UCLouvain

epl

École polytechnique de Louvain

Bionic prosthesis for the lower-limb - Design and development of a testbench for an ankle device

Author: **Thomas MORTIAUX**
Supervisors: **Renaud RONSSE, François HEREMANS**
Readers: **Jeanne EVRARD, Bruno DEHEZ**
Academic year 2022–2023
Master [120] in Electro-mechanical Engineering

Abstract

This study introduces the design and development of a testbench for a bionic ankle prosthesis, aimed at emulating the intricacies of a patient's gait cycle. The initial stage involves identifying the constraints of bipedal walking, along with its key phases. Subsequently, the design process addresses specified requirements, by the selection of design concepts, kinematic and dynamic models, and the integration of diverse actuators. The static and fatigue analysis extends to various components, encompassing the rotary shaft and platform, and its welds. The scope of sizing further encompasses the gear motor assembly, coupling, bearing units, mounting bracket, and finally linear modules.

Drawing from this comprehensive study, along with the extensive 3D CAO plan and product references derived, a fully-fledged prototype can be crafted for testing prosthesis systems. This prototype enables the realistic simulation of a walking phase, thereby enhancing the accuracy and precision of characterizations within intricate and complex tests.

Acknowledgment

I would like to express my heartfelt gratitude to Professor Renaud Ronsse for the opportunity to work on this subject. His guidance, advice, and exceptional supervision have been very valuable throughout this journey.

I extend my sincere appreciation to Jeanne Evrard, my assistant, and François Heremans, my co-supervisor, for their numerous meetings, invaluable insights, unwavering availability, patience, and the time they generously dedicated to assisting me.

I am also thankful to all the companies and suppliers who took the time to address my inquiries and provide me with the necessary resources.

To my family, friends, and all those who supported me directly or indirectly, I extend my heartfelt thanks for their encouragement, assistance, and patience.

This Thesis would not have been possible without the collective support, encouragement, and guidance from each of these of you. Merci à tous

Contents

Chapter 1

Introduction

1.1 Context

Limb amputation is a major surgical procedure that has significant physical and psychological consequences in a person's life. Various types of amputations exist depending on the body part affected. Specifically, lower limb amputation (LLA) considerably affects mobility and the overall quality of life of the amputee. Studies have shown various impacts that this type of operation can have on the mobility of the amputee. On average, an above-knee amputation reduces self-selected walking speed by 8.6% and increases metabolic cost by 46% in an active limb during walking compared to non-amputees [1]. Many people around the world face the daily repercussions of lower limb amputation. In fact, the reasons for such amputations can be diverse, including infection, tumor, diabetes, vascular compromise or trauma [2] [3].

In this context, the improvement of techniques and technologies in the field of ankle prosthetics is essential to hope that a person with lower limb amputation can regain as much mobility as possible. Specifically, there are ankle prostheses known as 'active' because they have the particularity of providing net positive energy during the walking cycle. This type of prosthesis helps partially to compensate for the negative consequences of an amputation on mobility. Designing and developing such prostheses involves numerous challenges. Indeed, lightweight, energy efficiency, biomimicry, and the ability to meet the specific needs of the patient are examples of important characteristics in the design of a prosthesis. In this regard, being able to test and evaluate the performance of a prosthesis or prototype is crucial in the design process.

In this perspective, the aim of this thesis is to design and develop a test bench to assess the performance of a bionic ankle prosthesis. The specific prosthesis under consideration is the Efficient Lockable Spring Ankle (ELSA) prosthesis, currently under development within the university. Specifically, the test bench will be designed to simulate the conditions of a patient's gait cycle, allowing for easier evaluation of the prosthesis's performance.

1.2 Structure of the thesis

This Master's thesis comprehensively outlines the entire process that led to the final design of the test bench. To achieve this, the thesis is divided into several chapters. Here is a description of the content of each of them :

Chapter 2 covers all the design steps, starting with the detailed specifications of the design project. Then, there is a phase of understanding the challenges of bipedal gait to correctly translate the design requirements and propose various conceptual designs. After selecting the most suitable design concepts, kinematic and dynamic models of the solution are created. Subsequently, based on these models, the characterization of the different actuators is performed.

After all these design steps, the next stage is the dimensioning phase. This step is detailed in Chapter 3. In this chapter, all components of the test bench are sized to perfectly meet their assigned specifications. During the dimensioning process of the various bench components, there will be calculations, characterizations, model research, verification, and, finally, the completion of the final modeling.

Chapter 4 will conclude this Master's thesis. In this chapter, we will provide an overall assessment of the proposed design solution for the test bench. An objective critique of the solution will be conducted, and finally, we will verify that all the specifications have been successfully met.

1.3 State of the art

A "test bench" is a general term encompassing all physical systems aimed at testing and measuring the behavior and performance of a product or device. Its purpose is to recreate, in a parameterized and controlled manner, the conditions of use of the product or device. In the industry, test benches are widely used in the design processes. They can be employed to verify compliance with standards, test performances, identify failures, or explore potential areas of improvement. Therefore, it can be understood that two test benches, designed to test the same type of product, can be entirely different depending on the pre-established specifications. In the field of prosthetics, test benches can also vary significantly from one another, despite all being designed to test the same type of product. This section aims to review the existing literature on ankle prosthesis test benches to provide an overview of the current state of advancements in this field.

A test bench must, therefore, meet the assigned specifications. If the testing requirements are straightforward, the test bench can also be simple as long as it meets expectations. For instance, in Figure 1.1, a relatively simple test bench can be observed. This test bench was designed to evaluate a parallel elastic actuator (PEA) power ankle prosthesis driven by an electro-hydrostatic actuator (EHA) [4]. The objective of this test bench was simply to perform a load test on the prosthesis for flat walking conditions. The prosthesis was thus securely fixed with a spring attached to its end to verify that it meets the bio-mechanical dynamics requirements.

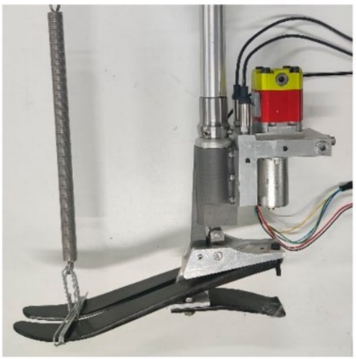

Figure 1.1: Loading test device for the experimental parallel elastic actuator parallel elastic actuator ankle prosthesis Driven by electro-hydrostatic actuator; Figure 7(a) of [4]

The following test bench has much more comprehensive specifications tailored to the specific type of prostheses being tested. Indeed, the test bench shown in Figure 1.2 was designed to test specific running prostheses for Paralympic athletes [5]. It is a multi-component test bench used for static and dynamic characterization of the prosthesis during jumping and sprinting events. The aim of the study is to test the stiffness properties of the prosthesis to achieve an optimal prosthesis for Paralympic runners. As seen in Figure 1.2a, the test bench is composed, among other elements, of two perpendicular hydraulic actuators and a substitute ground surface. This ground surface can be inclined up to +- 45°, allowing for the reproduction of the relative angle between the ground and the prosthesis. Combined together, the actuators and the ground surface enable the application of static and dynamic loads to the prosthesis during ground contact. The test bench is capable of replicating a loading cycle with amplitudes of up to 6000N and a period of 0.12 seconds, corresponding to typical characteristics of the stance phase of a sprint or long jump.

There are also highly comprehensive testing benches available for companies developing prosthetics. Two examples of such testing benches can be seen in Figure 1.3a and Figure 1.3b . Both testing benches comply with the ISO 22675 standard [6] for ankle-foot devices and foot units testing. The first bench (Figure 1.3a)[7] is from the company 'Thelkin' and faithfully replicates the load profile of a leg during a walking cycle [1]. The bench can apply dynamic loads up to $10kN$ and static loads up to $5kN$, with a step frequency of up to $5Hz$. This type of bench is quite large, measuring 2.25m in height, 1.2m in length, 0.65m in width, and has a mass of 650Kg. The second bench (1.3b) [8] is from the

[1] A video of the bench in motion can be viewed at the following link : `https://www.youtube.com/watch?v=B8r42-IObgY&ab_channel=THELKIN`

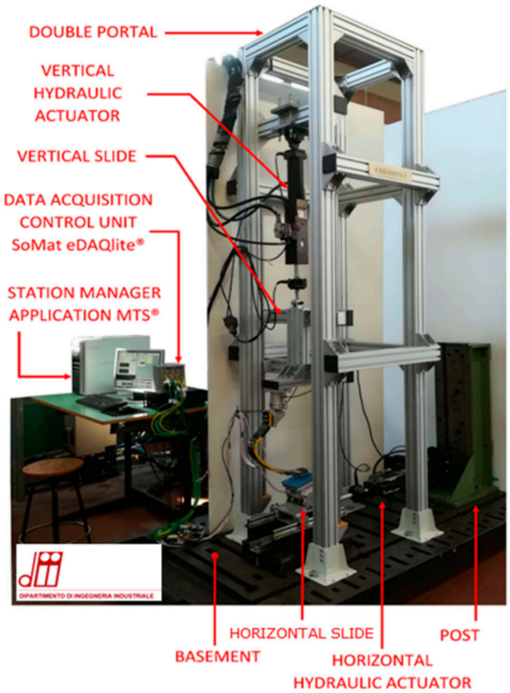

(a) Test bench with details of individual components ; Figure 3 of [5]

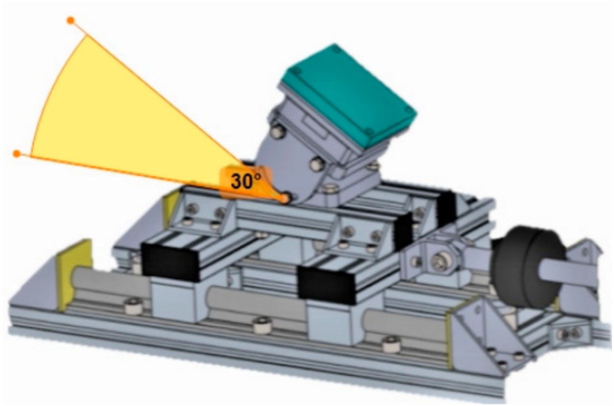

(b) Detailed view of the horizontal slide oriented at -30° ; Figure 4(a) of [5]

Figure 1.2: Test bench suitable for the static and dynamic characterization of a running prosthetic feet [5]

company 'Shore Western'. It is a servohydraulic system that also accurately reproduces the load profile of a leg during a walking cycle. The bench can provide axial load up to 6.8kN, its platform has a rotation amplitude of 70° (from -25° to 45°), and can have a cycle frequency of up to 1.5 Hz.

After reviewing several different examples of existing literature on ankle prosthesis test benches, we can now attempt to address the following question : What contributions can the design and realization of a test bench for the ELSA prosthesis bring ? Firstly, as we have seen, the existing ankle prosthesis test benches on the market are quite complex and offer a generalized solution for different types of prostheses. Therefore, they can represent a significant cost, require specific facilities, and are not specific to the development of the ELSA prosthesis. Designing and creating a test bench tailored to the needs of the ELSA prosthesis would offer a more cost-effective, accessible, and targeted solution to meet the goals and requirements of the prosthesis. Secondly, there are some gaps in the literature regarding testing benches for foot and ankle prostheses. The research conducted for the design of this bench could contribute to filling these gaps. Finally, realizing this testing bench would undoubtedly improve the development process of the ELSA prosthesis, which, in general, contributes to the advancement of research in the field of prosthetics aimed at enhancing the mobility and quality of life of amputees.

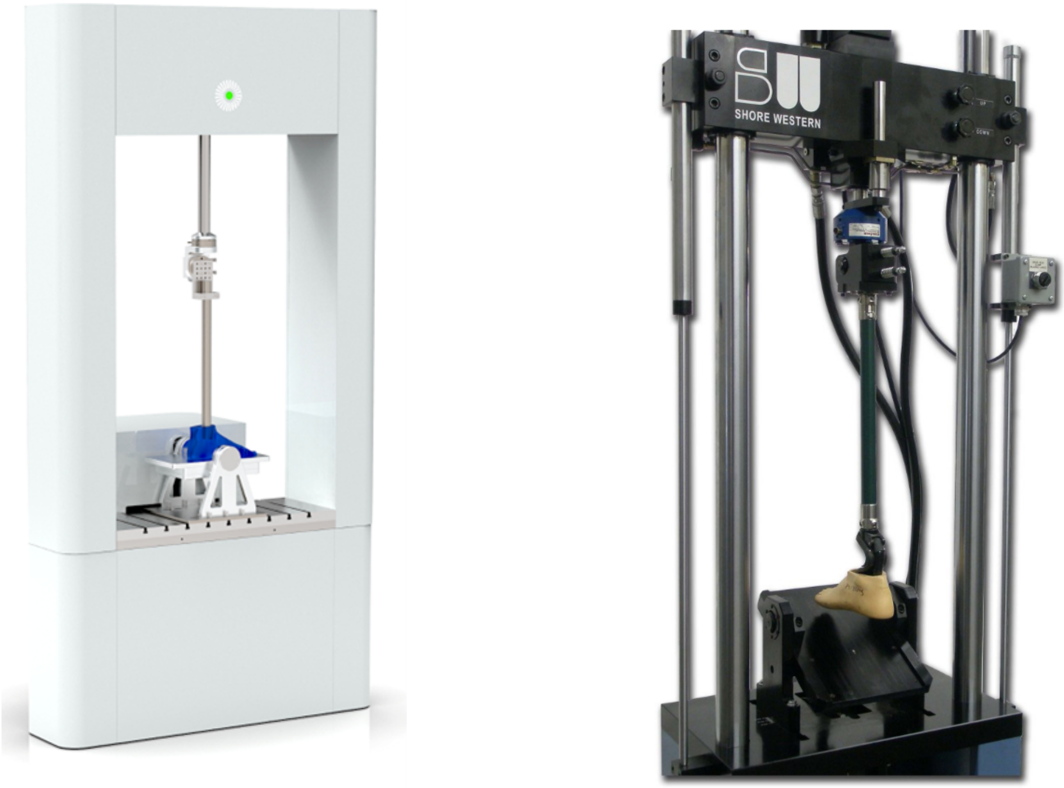

(a) Testing systems for foot and ankle prosthesis from 'Thelkin' [7]

(b) Ankle-Foot Prosthesis Simulator from 'Shore Western' [8]

Figure 1.3: ISO 22675 standard test benches

Chapter 2

Design

As part of a design project, the goal is to meet the specified requirements while adhering to various constraints and proposing the most optimal solution. To find this solution, a process consisting of several steps needs to be followed. The first step is to translate the project's requirements into functional specifications, which will be done by establishing the project's specifications. Then, a review of bipedal walking in the context of an ankle-foot prosthesis will be done in order to understand these challenges. This will enable us to propose concept designs that align with the specifications and requirements of the prosthesis. After making an initial selection based on various criteria, kinematic and dynamic models will be developed, allowing for the characterization of different actuation systems. All the reasoning and various steps that led to the design and selection of a final concept will be detailed in this chapter.

2.1 Specifications

The very first step in a design project is to establish the project specifications. A summary of these specifications can be seen in Table 2.1. In this table, we can first observe the main functions (MF) of the project, each expressing a specific goal of the test bench. These functions are then accompanied by their functional requirements (FR), which represent precise criteria that the test bench must meet for each main function. Additionally, we include the main constraints (MC) of the project, also accompanied by their requirements (CR). During the design and dimensioning stages, it will be crucial to ensure compliance with these constraints. All of this together forms the project's specifications, serving as the starting point for the design phase.

Specifications	
Context	The objective of the project is to design and develop a test bench capable of reproducing the operating conditions of a bionic prosthesis to test its performance.
Main Functions	MF 1 : to generate the contact profile between the ground and the prosthesis in the sagittal plane during a gait cycle MF 2 : to characterize the prototype during the cycle MF 3 : to be compliant to inclined slopes and/or stairs ascending/descending
Functional Requirements	FR 1.1 : to cover an operating frequency (gait cycle/second) of 0Hz to 1Hz FR 1.2 : to generate the ground reaction forces on the prosthesis for a body up to 150kg FR 1.3 : to be compliant to ISO10328 standard tests FR1.4 : to ensure compatibility with the interface of various ELSA prototypes FR 2.1 : to measure the torque in the prosthesis joint FR 2.2 : to measure the interaction forces between the ground and the prosthesis FR 3.1 : to be compliant to slopes from -15° to 15° FR 3.2 : to be compliant for standard-sized stairs specification with steps of 180 mm in height and 300 mm in depth
Main Constraints	MC 1 : safety of the user MC 2 : available energy sources
Constraints Requirements	CR 1.1 : Protection box CR 1.2 : Emergency stop button CR 1.3 : Noise limited to 80 dB CR 2.1 : Electrical power supply of 230 V CR 2.2 : Pneumatic power up to 7 bar

Table 2.1: Test bench specifications

2.2 Challenges of bipedal walking

Before diving directly into the concept design phase, it is essential to thoroughly understand all the implications of the various requirements in the specifications. To achieve this, we will review different aspects of bipedal walking to gain a comprehensive understanding of all the challenges of this test bench. To begin, we will outline the different stages that constitute a gait cycle. As depicted in Figure 2.1, a leg's gait cycle consists of a stance phase when the foot is in contact with the ground (60% of the cycle) and a swing phase when the foot is not in contact with the ground (40% of the cycle). For an ankle prosthesis, the most important characteristics of walking are the ground reaction forces (GRF) on the foot and the relative movements of the ankle and foot with respect to the ground. Within the scope of this test bench, we will focus solely on the components of walking in the sagittal plane. Indeed, the sagittal plane encompasses the dominant components of a gait cycle.

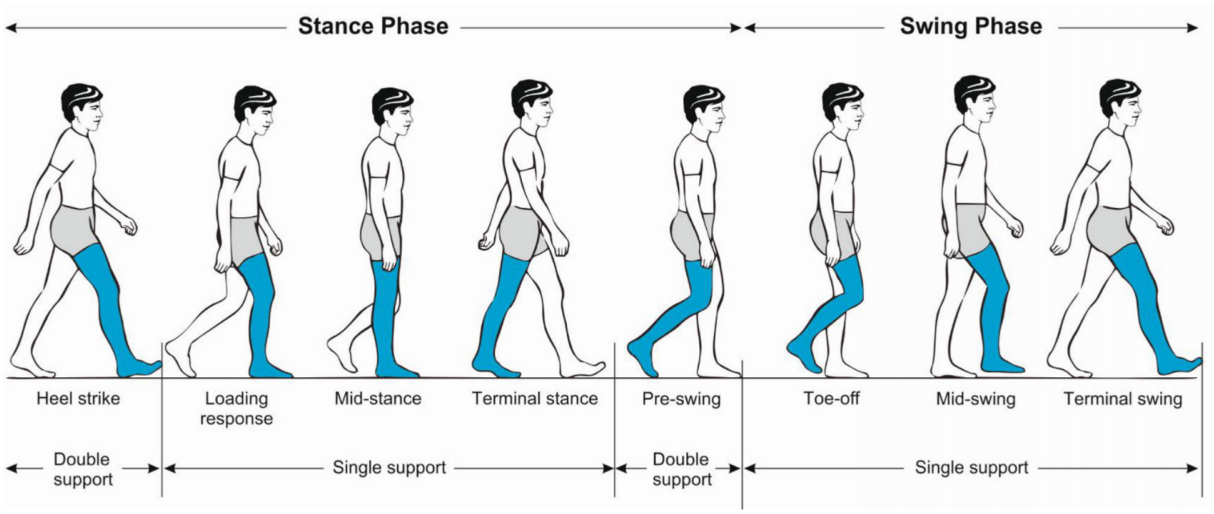

Figure 2.1: Gait cycle phases ; Figure 1 from [9]

As the stance phase involves contact between the foot and the ground, it is undoubtedly the most complex phase to reproduce. To faithfully replicate this phase, it is necessary to maintain the contact between the foot and the ground while preserving the relative angle between the sole of the foot and the ground. This situation is illustrated in Figure 2.2, where we can observe a first case with an ankle angle α of 0°, a contact point between the ground and the foot at coordinates X_1 and Y_1, and a relative angle between the ground and the foot β_1. Subsequently, we can observe a second case with an ankle angle α less than 0°, a contact point between the ground and the foot at coordinates X_2 and Y_2, and a relative angle between the ground and the foot β_2.

In these diagrams, we have taken the center of the ankle joint as a reference point. It can be observed that as the ankle angular position (α) and the relative angle between the foot and the ground (β) vary throughout the gait cycle, in order to maintain the

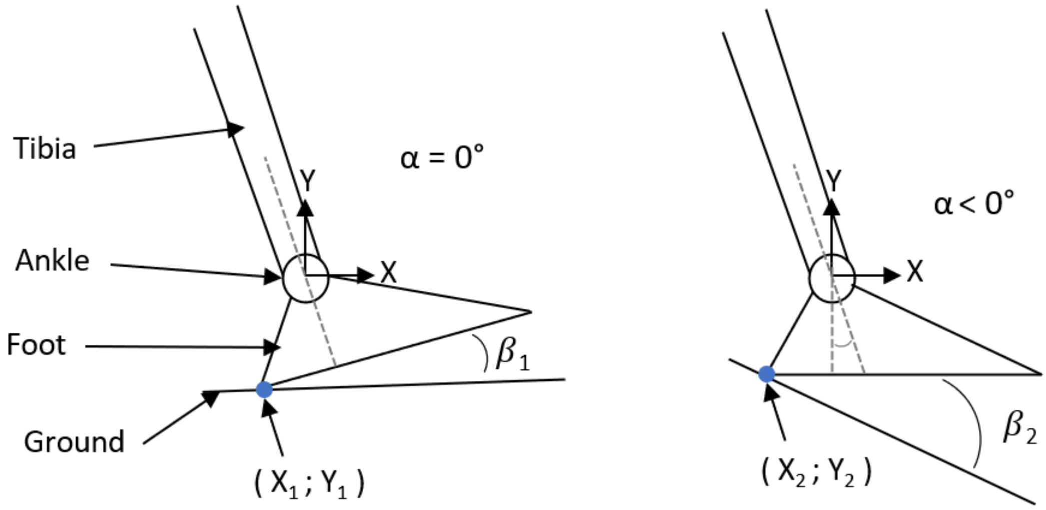

Figure 2.2: Representative diagrams of a tibia-ankle-foot assembly in contact with the ground, with β as the relative angle between the foot and the ground, α as the ankle angle, and (x;y) as the coordinates of the contact point.

changing position of the contact point (x;y) and the evolving relative angle between the foot and the ground during the gait cycle, the test bench will need to have 3 actuated degrees of freedom to control these positions x, y, and β (the angle α being actuated by the prosthesis). With regard to the ground reaction force (GRF), since we are working solely in the sagittal plane, it possesses only two components (vertical and horizontal), as shown in Figure 2.3. The test bench will, therefore, need to be capable of generating both the vertical and horizontal components of the ground reaction force.

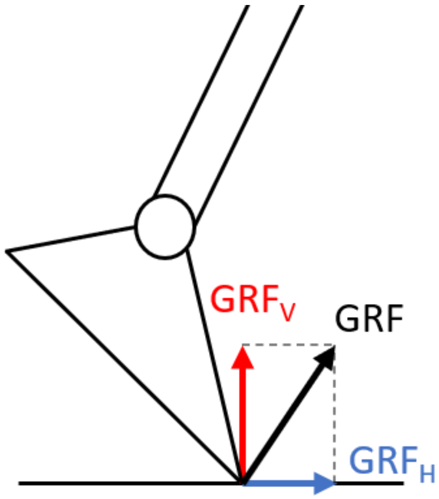

Figure 2.3: Schematic representation of the vertical (GRF_V) and horizontal (GRF_H) components of the ground reaction force on the foot in the sagittal plane.

2.3 Conceptual design

We are now able to propose different design concepts that align with the project specifications. These initial designs are at the conceptual stage, meaning they are solely described by translation and rotation movements. No specific actuation or guidance mechanism is mentioned yet. The various proposed designs can be seen from Figure 2.4 to Figure 2.7. All these models will follow the same code. Blue rectangles represent linear movements, while blue circles represent rotational movements. These shapes are accompanied by arrows indicating the direction of their movement. The color code of these arrows is as follows: a red arrow represents position-controlled actuation, an orange arrow represents force-controlled actuation, and a green arrow represents actuation controlled by the prosthesis. Each design will be represented during both the stance and swing phases.

In the first conceptual design (Figure 2.4), only the prosthesis is set in motion, while the substitute ground remains stationary. Here, we have two linear movements and one rotational movement. The arrangement of these movements among themselves is not yet significant. If this solution is chosen, a kinematic study will be necessary to determine how to arrange the three movements. This solution encompasses all configurations of 3 degrees of freedom (including at least one minimum rotation) that set the prosthesis in motion. For the swing phase (Figure 2.7a), as the prosthesis needs to follow a specific trajectory and there is no contact with the ground, it is apparent that all three degrees of freedom should be position-controlled. However, during the stance phase (Figure 2.7b), where contact between the prosthesis and the ground is established, all 3 movements will be kinematically constrained. Controlling only one of the three movements in position will allow the desired trajectory to be followed, while the other two will need to be force-controlled to maintain contact. In this case, we have chosen the rotational movement to be position-controlled, but any of the three could have been chosen. This reasoning applies to the upcoming designs as well.

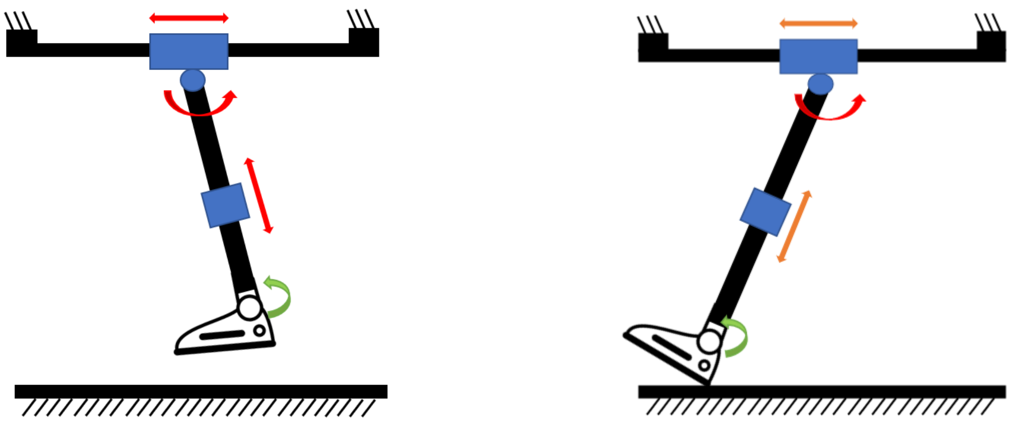

(a) Swing phase

(b) Stance phase

Figure 2.4: Conceptual Design 1

The second design (Figure 2.5) involves moving only the ground, while the prosthesis remains stationary. This solution consists of 3 degrees of freedom, including at least one rotation. In this case as well, the positions of the different movements can be interchanged. This design encompasses all solutions that solely involve moving the ground and not the prosthesis.

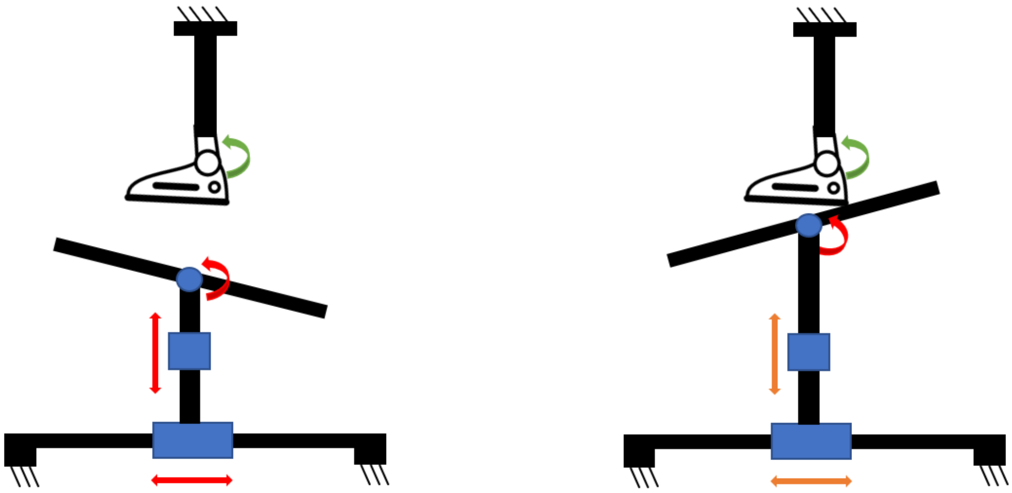

(a) Swing phase (b) Stance phase

Figure 2.5: Conceptual Design 2

Designs 3 and 4 set both the ground and the prosthesis in motion. Design 3 (Figure 2.6) initiates movement in the prosthesis using two degrees of freedom, while design 4 (Figure 2.7) employs a single degree of freedom for the prosthesis movement. If either of these solutions is chosen, it will also be necessary to investigate the various arrangements of degrees of freedom among them.

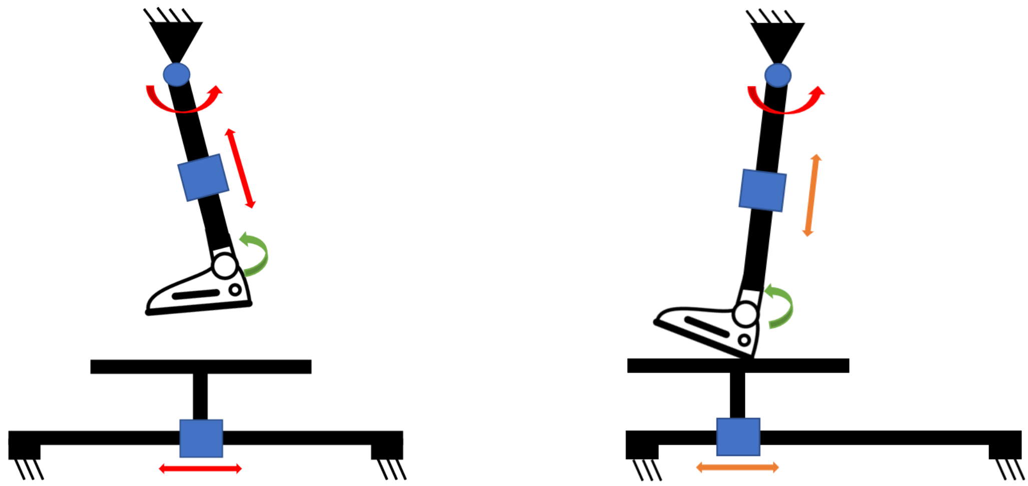

(a) Swing phase (b) Stance phase

Figure 2.6: Conceptual Design 3

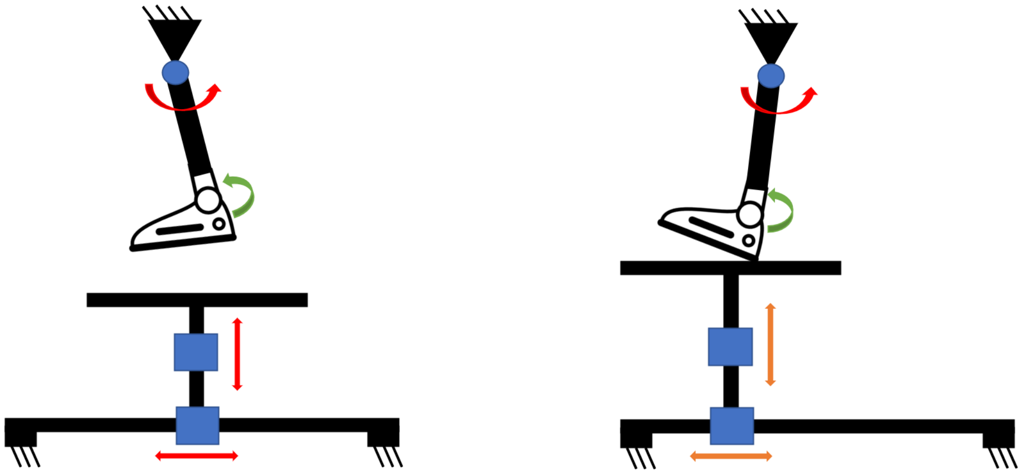

(a) Swing phase (b) Stance phase

Figure 2.7: Conceptual Design 4

Now, a selection must be made among these different designs. To achieve this, several selection criteria will be employed to objectively compare the solutions. At this stage of the design, we are not yet going into enough detail to compare these solutions in terms of the complexity of the actuation system, fabrication or cost. Three criteria have been identified for distinguishing these solutions. The first criterion is based on the number of bodies (prosthesis and/or ground) in motion, assuming that an increase in the number of moving bodies adds complexity to the bench. The second criterion is based on the number of moving actuators, which refers to the number of actuators in series with one another, also contributing to increased complexity of the bench. The final criterion concerns the complexity of measuring the ankle joint torque of the prosthesis, assuming that this measurement is complicated by the movement of the prosthesis. A summary table outlining the selection of one of the four designs based on these criteria can be found in Table 2.2. In this table, each criterion has been weighted by a weight factor based on its significance in relation to the other criteria. It can also be observed that for comparing the various designs, Design 1 was used as the baseline model, hence its column is filled with zeros. In the end, by summing up the three criteria, Design 1 has been selected.

Criteria	Weighting	Design 1	Design 2	Design 3	Design 4
Number of moving bodies	2	0	0	-	-
Number of moving actuators	2	0	0	+	+
Torque measurement complexity	1	0	-	-	-
Total		0	-	-	-

Table 2.2: Comparison table of the different design solutions

2.4 Kinematic study

The chosen solution therefore has 3 degrees of freedom, including at least one rotation. As these 3 degrees of freedom are in the same plane, there are 7 different possible configurations. These configurations are depicted in Figure 2.8, where q_1, q_2, and q_3 are either prismatic or revolute joints. To select among all these possibilities, we will conduct a kinematic study among these different configurations. To do this, we will establish the direct kinematic model for each of these configurations using the Denavit-Hartenberg convention [10]. This will then allow us to determine the Jacobian matrix (or Manipulator Jacobian), the determinant of which ($det\ J$) will enable us to make a selection.

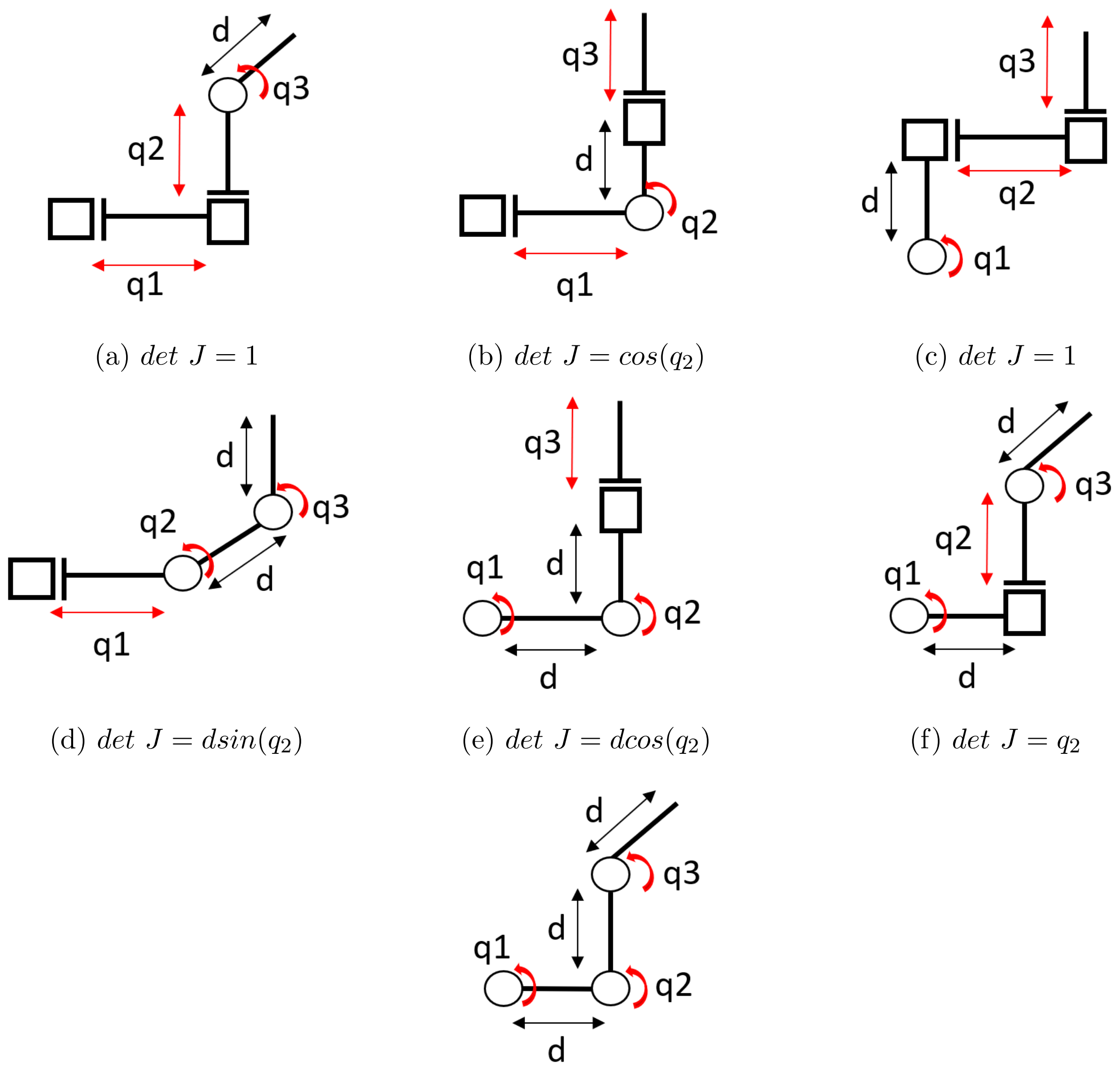

(a) $det\ J = 1$ (b) $det\ J = cos(q_2)$ (c) $det\ J = 1$

(d) $det\ J = dsin(q_2)$ (e) $det\ J = dcos(q_2)$ (f) $det\ J = q_2$

(g) $det\ J = d^2 sin(q_2)$

Figure 2.8: The 7 different possible configurations

The determinant of the Jacobian matrix for each configuration can be seen below its diagram in Figure 2.8 (the complete derivation leading to these results is provided in the appendices). The expressions of these determinants indicate the potential singularity configurations for the model. Identifying and avoiding these singularities is important for several reasons, such as the fact that in a singular configuration, certain directions of movement may become unreachable [10]. These are the configurations for which $Det\ J = 0$ that are referred to as singular configurations. Thus, it can be observed that several of the different solutions have singularities. These various solutions can also be compared based on their manipulating ability in positioning and orienting their end-effector [11]. The manipulability can be defined as : $\mu = |DetJ|$. Based on these criteria, configurations 'a' and 'c' from Figure 2.8 can be preferred. Furthermore, it can be assumed that the impact of the weight of actuators Q2 and Q3 on actuator Q1 will be less critical in solution 'a' than in solution 'c'. Ultimately, it is the solution 'a' from Figure 2.8 that is favored.

2.5 Dynamic model

We will now proceed to develop the dynamic model of our solution. This model is characterized by dynamic equations that establish the relationship between motion and force for each of the 3 actuators. To construct this model, we will employ the Euler-Lagrange equations as outlined in Section 6 of [10] and will utilize the notations from Figure 2.9 depicting the scenario.

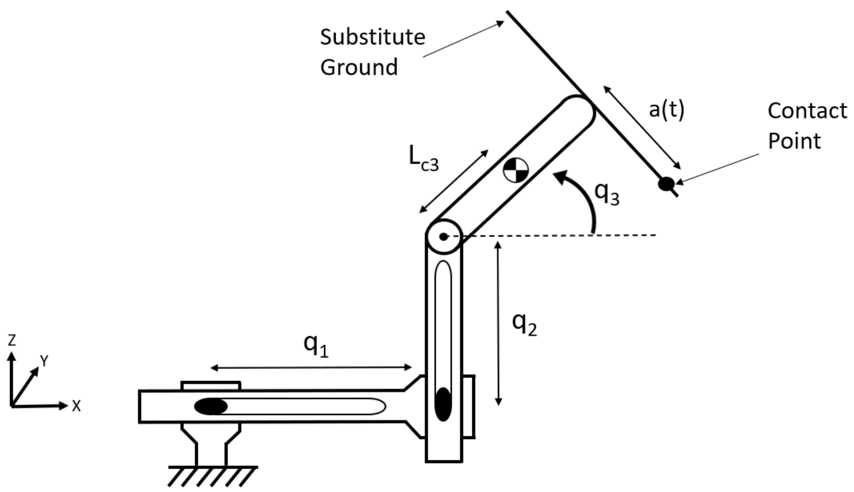

Figure 2.9: Representation of the scenario with q_1 denoting the position of the horizontal linear actuator (link 1), q_2 representing the position of the vertical linear actuator (link 2), q_3 indicating the angular position of the rotary actuator (link 3), L_{c3} signifying the distance between the center of rotation of actuator q_3 and its center of mass, and a(t) denoting the time-dependent position of the contact point between the prosthesis and the substitute ground.

Link 1 will represent the horizontal linear movement, link 2 the vertical linear movement, and link 3 the rotational movement. The position of the center of mass of these three links with respect to the inertial frame is given by :

$$Link\ \ 1\ \ :\begin{bmatrix}K_1+q_1\\0\\K_2\end{bmatrix};\ \ Link\ \ 2\ \ :\begin{bmatrix}K_1+q_1\\0\\K_2+q_2\end{bmatrix};\ \ Link\ \ 3\ \ :\begin{bmatrix}K_1+q_1+L_{c3}cos(q_3)\\0\\K_2+q_2+L_{c3}sin(q_3)\end{bmatrix}$$

where K_1 and K_2 are constants. Therefore, we can calculate the velocity of their center of mass as :

$$v_{c1}=J_{vc1}\dot{q}\ \ ;\ \ v_{c2}=J_{vc2}\dot{q}\ \ ;\ \ v_{c3}=J_{vc3}\dot{q}$$

where,

$$J_{vc1}=\begin{bmatrix}1&0&0\\0&0&0\\0&0&0\end{bmatrix};\ \ J_{vc2}=\begin{bmatrix}1&0&0\\0&0&0\\0&1&0\end{bmatrix};\ \ J_{vc3}=\begin{bmatrix}1&0&-L_{c3}sin(q_3)\\0&0&0\\0&1&L_{c3}cos(q_3)\end{bmatrix};\ \ \dot{q}=\begin{bmatrix}\dot{q}_1\\\dot{q}_2\\\dot{q}_3\end{bmatrix}$$

So, we can write the total translational kinetic energy as :

$$\frac{1}{2}\dot{q}^T\{m_1J_{vc1}^TJ_{vc1}+m_2J_{vc2}^TJ_{vc2}+m_3J_{vc3}^TJ_{vc3}\}\dot{q}$$

where m_1, m_2, and m_3 are the respective masses of link 1, 2, and 3. Next, we can also provide the expression for the total rotational kinetic energy as :

$$\frac{1}{2}\dot{q}^T\{I_3\begin{bmatrix}0&0&0\\0&0&0\\0&0&1\end{bmatrix}\}\dot{q}$$

Where I_3 is the mass moment of inertia of link 3. Therefore, we can express the total kinetic energy 'K' of the manipulator as :

$$K=\frac{1}{2}\dot{q}^T\{m_1J_{vc1}^TJ_{vc1}+m_2J_{vc2}^TJ_{vc2}+m_3J_{vc3}^TJ_{vc3}+I_3\begin{bmatrix}0&0&0\\0&0&0\\0&0&1\end{bmatrix}\}\dot{q}=\frac{1}{2}\dot{q}^TD(q)\dot{q}$$

Where D(q) is called the 'Inertia Matrix' and its expression is :

$$D(q)=\begin{bmatrix}m_1+m_2+m_3&0&-m_3L_{c3}sin(q_3)\\0&m_2+m_3&m_3L_{c3}cos(q_3)\\-m_3L_{c3}sin(q_3)&m_3L_{c3}cos(q_3)&m_3L_{c3}^2+I_3\end{bmatrix}$$

We can now calculate the Christoffel symbols, the general expression of which is :

$$c_{ijk} = \frac{1}{2}(\frac{\partial d_{kj}}{\partial q_i} + \frac{\partial d_{ki}}{\partial q_j} - \frac{\partial d_{ij}}{\partial q_k})$$

The non-zero Christoffel symbols are :

$$c_{331} = -m_3 L_{c3} cos(q_3)$$

$$c_{332} = -m_3 L_{c3} sin(q_3)$$

Now, we need to compute the potential energy 'P' of the 3 links :

$$P_1 = m_1 g h$$
$$P_2 = m_2 g(h + q_2)$$
$$P_3 = m_3 g(h + q_2 + L_{c3} sin(q_3)$$

Where 'h' is a constant and 'g' the gravitational acceleration. The total potential energy is thus given by : $P = P_1 + P_2 + P_3$. Finally, if we defined :

$$\phi_k = \frac{\partial P}{\partial q_k}$$

We can write the Euler-Lagrange equations as :

$$\sum_i d_{kj}(q)\ddot{q}_j + \sum_{i,j} c_{i,j,k}(q)\dot{q}_i\dot{q}_j + \phi_k(q) = \tau_k \quad , \quad k = 1, 2, 3$$

Where τ_k is composed of the forces and torque delivered by the 3 actuators, as well as the external forces and torques acting on the system. In our case, only two external forces in the x and z directions act on our system, which are the reaction forces between the ground and the prosthesis. So we have:

$$\begin{bmatrix} \tau_1 \\ \tau_2 \\ \tau_3 \end{bmatrix} = \begin{bmatrix} F_1 \\ F_2 \\ T_3 \end{bmatrix} + J^T(q)F_{ext} = \begin{bmatrix} F_1 + F_x \\ F_2 + F_z \\ T_3 + F_z[dcos(q_3) + a(t)sin(q_3)] + F_x[a(t)cos(q_3) - dsin(q_3)] \end{bmatrix}$$

Where F_1 and F_2 are the forces delivered by actuators q_1 and q_2, T_3 is the torque delivered by actuator q_3, F_x and F_z are respectively the forces in the x and z (positive) directions at the contact point with the prosthesis (see Figure 2.9), and $J^T(q)$ is the transpose of the Jacobian matrix of the system, the derivation of which can be found in Appendix A.1 [1]. So we can finally write the 3 dynamical equations of the system as :

$$(m_1 + m_2 + m_3)\ddot{q_1} - (m_3 L_{c3} sin(q_3))\ddot{q_3} - (m_3 L_{c3} cos(q_3))\dot{q_3}^2 = F_1 + F_x \tag{2.1}$$

$$(m_2 + m_3)\ddot{q_2} + (m_3 L_{c3} cos(q_3))\ddot{q_3} - (m_3 L_{c3} sin(q_3))\dot{q_3}^2 + (m_2 + m_3)g = F_2 + F_z \tag{2.2}$$

$$\begin{aligned} &- (m_3 L_{c3} sin(q_3))\ddot{q_1} + (m_3 L_{c3} cos(q_3))\ddot{q_2} + (m_3 L_{c3}^2 + I_3)\ddot{q_3} + m_3 L_{c3} g cos(q_3) = \\ &\qquad T_3 + F_z[dcos(q_3) + a(t)sin(q_3)] + F_x[a(t)cos(q_3) - dsin(q_3)] \end{aligned} \tag{2.3}$$

2.6 Characterisation

For now, only the type of motion for the 3 degrees of freedom and their arrangement has been chosen. The manner in which these motions will be guided and actuated still needs to be determined. To make this choice, it is first necessary to characterize the three different movements, meaning to determine their range of velocity, acceleration, force, torque, and position. Gathering all this information will then allow us to make decisions among the various solutions.

2.6.1 Expressions of joint positions during stance phase

The first step is to determine the position profile of q_1, q_2, and q_3 during the replication of a gait cycle. As shown in Figure 2.10, during the stance phase, the positions of q_1, q_2, and q_3 will depend on the following factors : the relative angle between the prosthetic sole and the ground (β), the distances d and a(t), and the position of the contact point between the prosthesis and the ground in space. Since the prosthesis is attached to a fixed base, this position is dependent on the dimensions of the prosthesis and the angular position of the prosthetic joint (α).

Among these factors, the angles α and β will be determined by the desired walking trajectory. Regarding the distance "d," it should be minimized to reduce rotational inertia, but considering the thickness of the substitution ground that needs to bear significant loads, we will use an overestimated value for "d" of 5cm. As for the position "a(t)," we assume that the foot length is centered around the axis of rotation, which implies that "a(t)" can have both positive and negative maximum values of half the foot length (including the shoe). For our calculations, we will use a maximum foot length of 32cm, corresponding to a shoe size of 48. These negative and positive maximum values of "a(t)" are sufficient for establishing the position profiles of q_1, q_2, and q_3. In fact, during the stance phase, the substitution ground is always in contact either with the heel (maximum negative value of "a(t)") or with the front of the shoe (maximum positive value of "a(t)"),

[1] it is worth noting that a change of axis representation needs to be performed between the two models to use the expression of the Jacobian matrix found in Appendix A.1

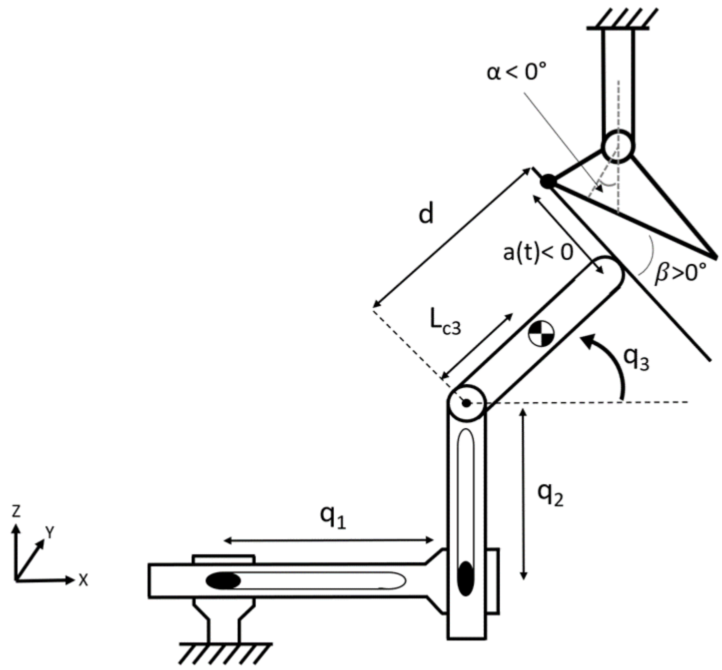

Figure 2.10: Representation of the contact between the prosthesis and the test bench during the stance phase.

which is sufficient from a kinematic standpoint to determine the position profiles of q_1, q_2, and q_3.

The kinematic relationship between the three joints and the contact point has already been established during the kinematic analysis (see Appendices A.1). If we define X_c and Z_c as the coordinates of the contact point in the sagittal plane, we can express the position of q_1 and q_2 during the stance phase as :

$$q_1 = X_c - dcos(q_3) - a(t)sin(q_3) \tag{2.4}$$

$$q_2 = Z_c - dsin(q_3) + a(t)cos(q_3) \tag{2.5}$$

However, it can be observed from Figure 2.10 that q_3 is constrained by the angles α and β :

$$q_3 = \alpha - \beta + \frac{\pi}{2} \tag{2.6}$$

So all that's left is to determine the position of the contact point based on the dimensions of the prosthesis and the angular position of its joint. The situation is depicted in Figure 2.11, where we can first observe the case of heel contact. Next, we can see the case of contact with the toe of the foot, and in the last image, we can observe the relevant dimensions and angles necessary for determining the position of the contact point based on the position of the center of the prosthesis joint $(X_j; Z_j)$.

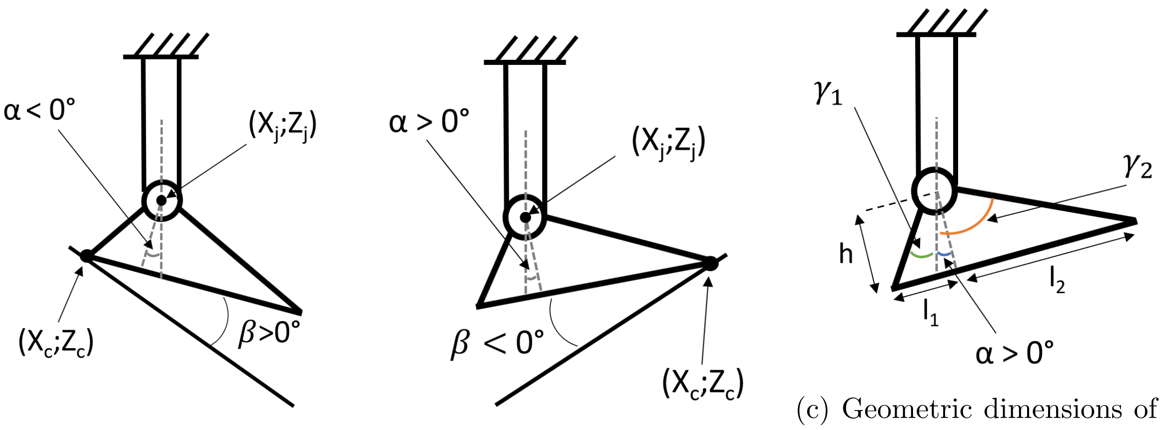

(a) Heel contact (b) Forefoot contact (c) Geometric dimensions of the prosthesis

Figure 2.11: Schematic representation of (a) the prosthesis in contact with the ground at the heel ; (b) the prosthesis in contact with the ground at the forefoot ; (c) the geometric dimensions of the prosthesis. Here, h represents the height between the center of the prosthetic joint and the sole, l_1 denotes the distance between the joint and the heel along the sole, l_2 is the distance between the joint and the toe along the sole, γ_1 represents the angle between the line connecting the joint and the heel and the line perpendicular to the sole passing through the center of the joint, and γ_2 represents the angle between the line connecting the joint and the toe and the line perpendicular to the sole passing through the center of the joint.

To derive the expression for the position, we will differentiate between the two scenarios depicted in Figures 2.11a and 2.11b. In the case of heel contact, we can write:

$$X_c = X_j - \sqrt{h^2 + l_1^2}\ sin(\gamma_1) \tag{2.7}$$

$$Z_c = Z_j - \sqrt{h^2 + l_1^2}\ cos(\gamma_1) \tag{2.8}$$

$$\gamma_1 = atan(\frac{h}{l_1}) - \alpha \tag{2.9}$$

For the case of contact with the toe of the foot, we can write :

$$X_c = X_j + \sqrt{h^2 + l_2^2}\ sin(\gamma_2) \tag{2.10}$$

$$Z_c = Z_j - \sqrt{h^2 + l_2^2}\ cos(\gamma_2) \tag{2.11}$$

$$\gamma_2 = atan(\frac{h}{l_2}) + \alpha \tag{2.12}$$

When the prosthesis is flat on the ground, both the heel and the forefoot are in contact with the surface. In this case, both expressions are applicable to determine the positions of the 3 joints. However, it is essential to use the appropriate value of a(t) (positive or negative) depending on whether one chooses the expression for the point of contact at the heel or at the forefoot. As for the values of h, l_1, and l_2, we relied on the dimensions of the ELSA prosthesis. For h, we added 3 cm to the measured value of 7 cm on the prosthesis to account for a larger shoe sole. For l_1 and l_2, we multiplied the measurements taken from the prosthesis by a proportionality factor to match the dimensions of a size 48 foot, resulting in l_1 = 7.4 cm and l_2= 24.6 cm..

2.6.2 Kinematic data for different gait cycles

Now, to plot the different profiles of joint positions, we need data for the relative angle between the ground and the prosthesis, as well as for the angle of the prosthesis joint during a walking cycle. As specified in the project requirements, we need to gather data for walking on flat ground, walking on inclined surfaces, as well as for stair ascent and descent.

The goal of a bionic prosthesis is to provide the amputee with sensations as close as possible to a healthy limb. Therefore, it is preferable to use trajectory data of movements from healthy limbs rather than the experimental data collected during tests of the ELSA prosthesis. For walking on flat ground, we will thus utilize reference trajectory data from Winter [12] for ankle angular position. However, for the relative angle between the foot and the ground, we will employ ELSA's data. For stair ascent and descent, we will also use reference trajectory data [13] for ankle angular position. As before, we will use ELSA's data for the relative angle between the foot and the ground. Graphical representations of the data used for the three different types of walking can be seen in Figure 2.12.

For walking on inclined slopes, the data used comes from a study on the kinetics and kinematics of locomotion in healthy individuals [14]. In this study, walking on inclined surfaces was performed for slopes of +- 5° and +- 10° at speeds of 0.8, 1, and 1.2 [m/s]. Here, we will use the data for slopes of +- 10° at 1.2 [m/s]. The graphical representation of this data can be seen in Figure 2.13.

2.6.3 Joint position profiles

Based on the collected data from the 5 different gait cycles, it is now possible to establish the joint position profiles during these cycles. During the stance phase, we will use equations 2.4 to 2.12 to determine the joint positions. However, during the swing phase, the joints are not kinematically constrained, so there are different possible trajectories to return to their initial positions (beginning of the stance phase). Here, to establish the joint position profile during the swing phase, we will use a Lagrange polynomial interpolation. Indeed, this allows us to closely follow the trajectory of the position profile curve at the beginning and end of the stance phase, avoiding abrupt changes in velocity and thus preventing significant acceleration spikes.

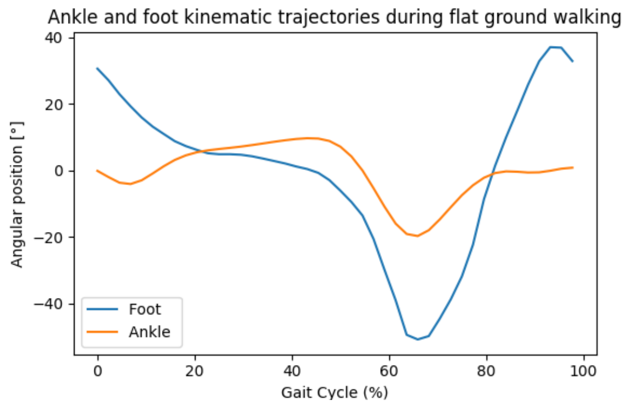

(a) Flat ground walking

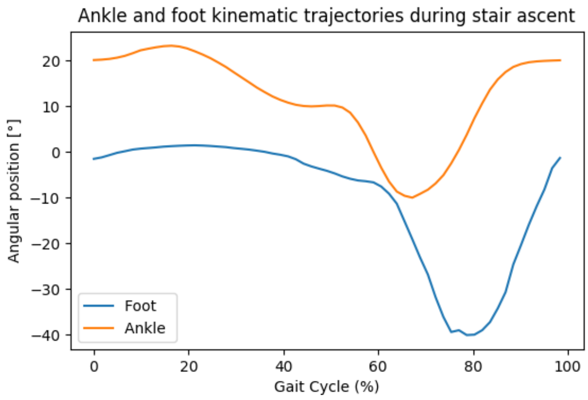

(b) Stair ascent

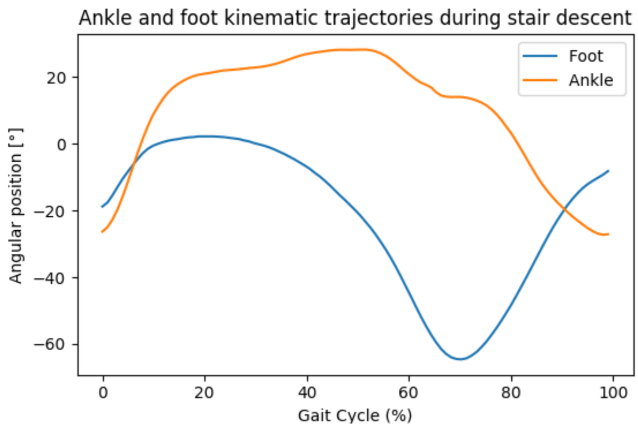

(c) Stair descent

Figure 2.12: Ankle and foot kinematic trajectories during (a) flat ground walking ; (b) stair ascent ; (c) stair descent. The angular positions of the foot and the ankle correspond respectively to angle β and α of Figure 2.11.

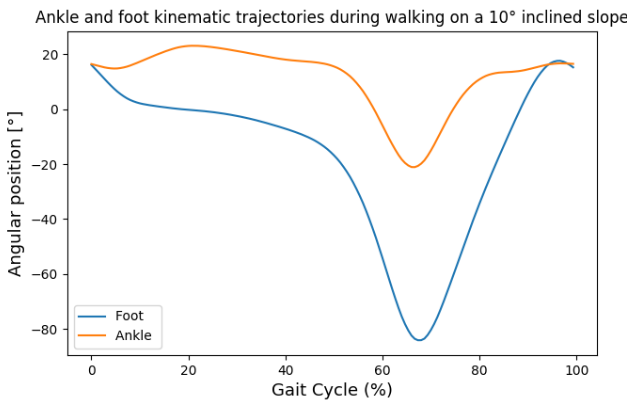

(a) Walking on a 10° inclined slope

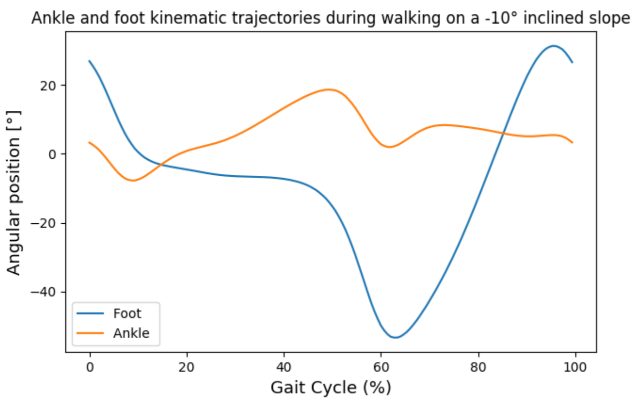

(b) Walking on a -10° inclined slope

Figure 2.13: Ankle and foot kinematic trajectories during walking on (a) a 10° inclined slope ; (b) a -10° inclined slope. The angular positions of the foot and the ankle correspond respectively to angle β and α of Figure 2.11. Kinematic data from [14].

The joint position profile during a walking cycle for stair ascent has been graphically represented in Figure 2.14, while the position profiles for the other 4 walking cycles can be found in Appendix B. The position profiles exhibit validation points. In fact, to verify the accuracy of these position profiles, a 3D model of our design was constructed, adhering to the specified dimensions. Two different views of the model are presented in Figure 2.15. By setting specific angular positions for the foot and ground of the 3D model, corresponding to trajectory data, and then measuring the joint positions on the model, validation points were established. These validation points serve to confirm the validity of our position profiles.

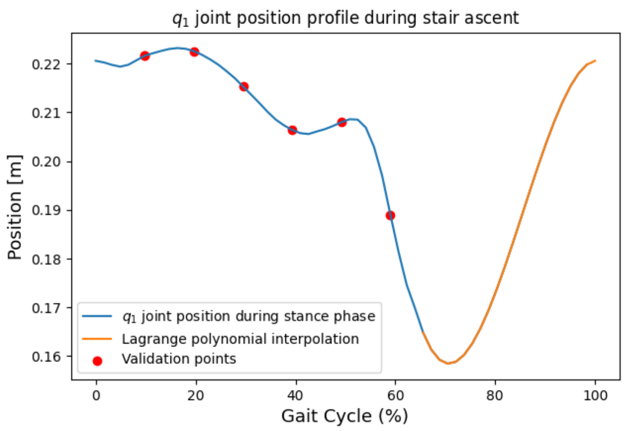

(a) q_1 joint position profile

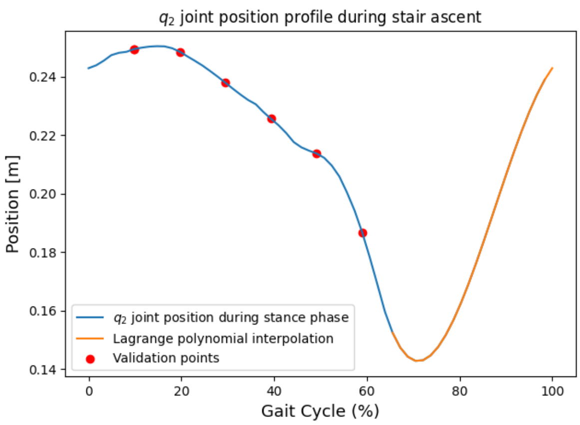

(b) q_2 joint position profile

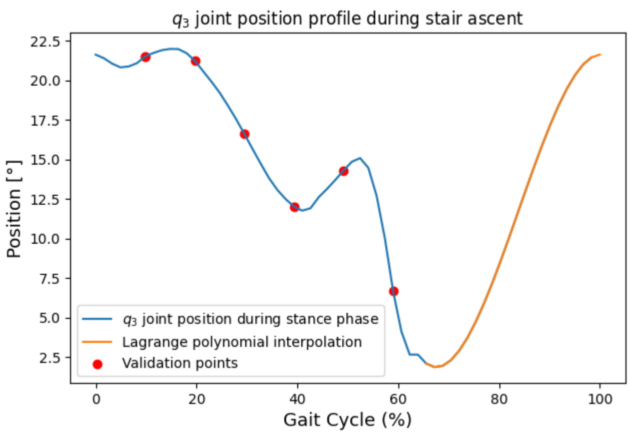

(c) q_3 joint position profile

Figure 2.14: Joint position profiles during stair ascent, with the stance phase position profile shown in blue, the position profile established using Lagrange polynomial interpolation in orange, and the validation points based on the 3D model marked in red.

2.6.4 Joint velocity and acceleration profiles

We can now establish the velocity and acceleration profiles based on the position profiles. As these profiles serve to characterize our actuators, we utilize the maximum step frequency (1 gait cycle per second) to calculate the velocity and acceleration profiles from the position. In Figure 2.16, we can observe the velocity and acceleration profile of joint q_1

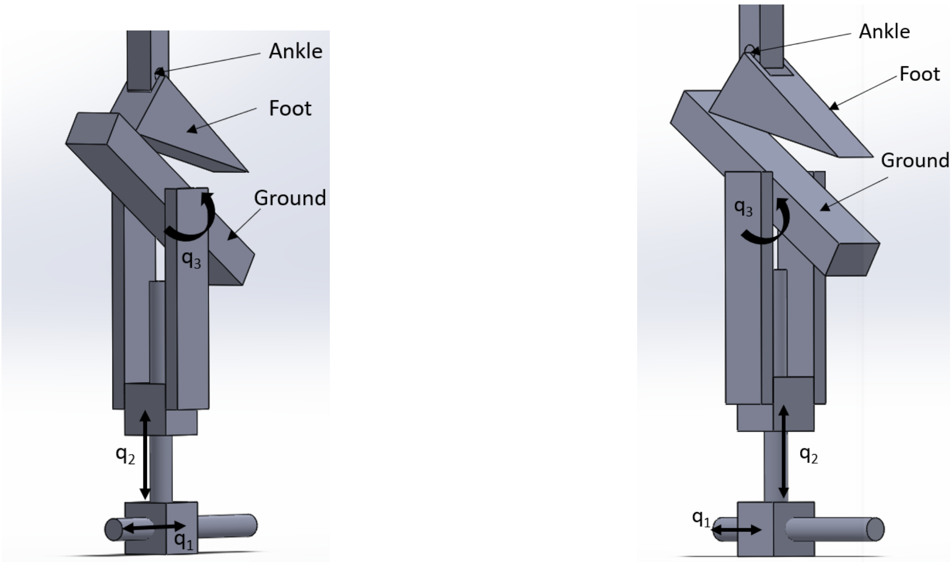

Figure 2.15: 3D draft of the current design

during stair ascent. We can notice abrupt changes in the velocity and acceleration profile. This is attributed to the low resolution of the data used to establish the position profile. To address this issue, we will resample the data using interpolation and then apply a 3rd-order Butterworth filter with a cutoff frequency of 10 Hz. The results of the profiles based on different data processing can be observed in Figure 2.17. For the position profile, no significant differences are noticed among the three curves during the stance phase. However, for the velocity and acceleration profiles, the benefits of resampling and filtering are clearly evident. All the position, velocity, and acceleration profiles for the three joints in the five different walking types can be found in Appendix B.

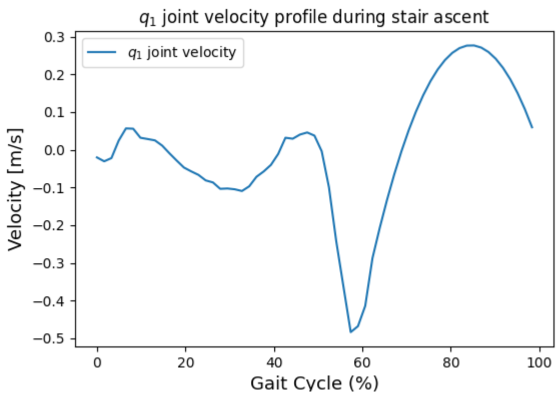

(a) q_1 joint velocity profile

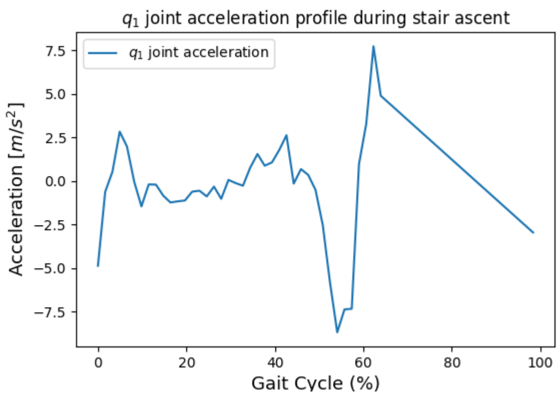

(b) q_1 joint acceleration profile

Figure 2.16: q_1 joint velocity and acceleration profile during stair ascent

2.6.5 Force and torque profiles

To complete the characterization, we now need to establish the joint forces profiles for q_1 and q_2, as well as the joint torque profile for q_3, for the five different walking scenarios.

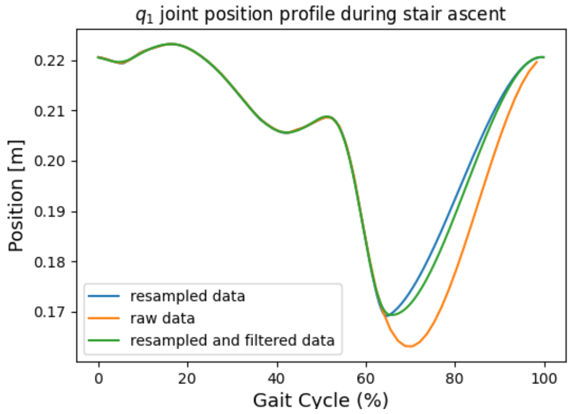

(a) q_1 joint position profile

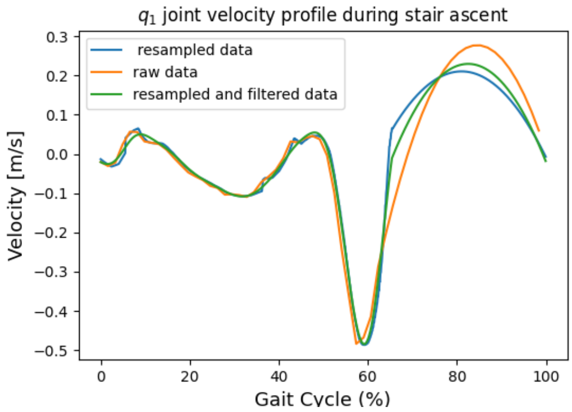

(b) q_1 joint velocity profile

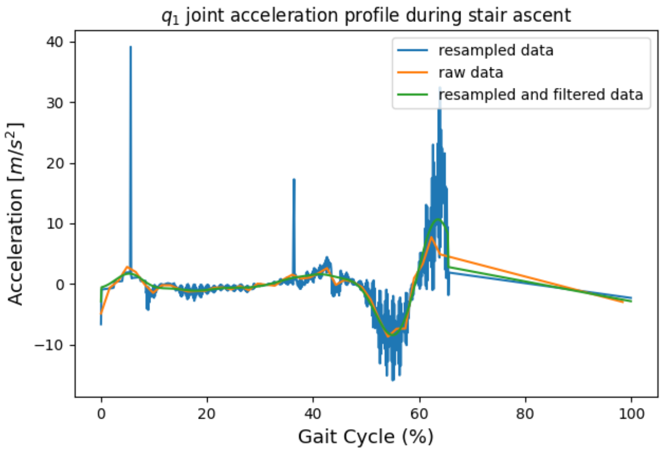

(c) q_1 joint acceleration profile

Figure 2.17: Position, velocity, and acceleration profile of joint q_1 during stair ascent. For each of the profiles, three versions are presented based on data processing : raw data, resampled data, and resampled and filtered data.

To accomplish this, we will employ the dynamic equations 2.1, 2.2 and 2.3 that we derived earlier. In these equations, we are seeking to determine F_1, F_2, and T_3, which represent the forces for joints q_1 and q_2, and the torque for joint q_3, respectively. Of course, in these equations, there are parameters that depend on the final solution, so it will not be possible to determine the required forces and torque accurately. However, assumptions can be made about these parameters to gain an understanding of the magnitudes of forces and torque. Firstly, we will assume that the masses m_1, m_2, and m_3 are 5 kg.For L_c3, by examining the dynamic equations, one can consider that it is preferable for the rotational element to have its center of mass on the axis of rotation (as in the 3D draft model on Figure 2.15) and hence, L_c3 is zero. For I_3, if we assume that the platform (or substitute ground as shown in Figure 2.9) should accommodate a size 48 shoe, then this platform needs to be 32cm long, 15cm wide, and let's overestimate its thickness as 5cm. Assuming this platform is symmetric with respect to the axis of rotation (as in the 3D draft model), and utilizing the density of aluminum (a lightweight and strong material that fits our application well), we obtain a mass moment of inertia of :

$$I_3 = \frac{2800(0.32\ 0.15\ 0.05)(0.32^2 + 0.05^2)}{12} = 0.0587 \quad [kgm^2]$$

Now, the only missing information is the ground reaction forces (GRF) between the prosthesis and the ground in the sagittal plane, denoted as F_x and F_z. The data from a gait analysis study [15] on healthy individuals was utilized for the GRF during walking on flat ground and for stair descent and ascent. For walking on flat ground, the data used are those of adults walking at a speed normalized to their height ($\frac{v}{h}$ [1/s]) between 0.8 and 1. For a person of 1.8 m, this corresponds to a walking speed between 5 and 6.5 km/h, and for a person of 1.6 m, it corresponds to a walking speed between 4.6 and 5.76 km/h. It is not straightforward to convert this into a step frequency as the length of a step depends on various factors such as a person's age, height, or gender [16]. However, it is possible to estimate the average step length of a male and female based on walking speed [17]. By doing so, we find in both cases a step frequency of about 2 steps per second, which corresponds to a walking cycle frequency of one cycle per second. For stair ascent and descent, the data used were from adults climbing standard-sized steps (180 mm in height and 300 mm in depth), but for these measurements, no walking speed is mentioned, so it is assumed that a standard walking speed is used for ascending and descending stairs. For walking on inclined slopes, the same study [14] that provided the source for kinematic trajectories will be utilized to obtain the GRF data.

The GRF data does not directly provide us with the forces F_x and F_z that we need. As seen in Figure 2.18, the GRF in the sagittal plane is provided with a 'Vertical' component perpendicular to the ground and a 'Forward' component parallel to the ground. Therefore, we can calculate our forces F_x and F_z using trigonometry as follows :

$$F_z = GRF_V sin(q_3) - GRF_F cos(q_3) \tag{2.13}$$

$$F_x = GRF_V cos(q_3) + GRF_F sin(q_3) \tag{2.14}$$

where GRF_V and GRF_F correspond respectively to the vertical and forward components of the GRF.

The GRF data also had to be resampled and filtered in the same manner as before. The processed data for stair ascent can be observed in Figure 2.19a. Using this data, we can reconstruct the forces F_x and F_z as shown in Figure 2.19b. It is now possible to calculate F_1, F_2 and T_3. For characterization purposes, we will considered the worst-case scenario and thus calculated the forces for a person weighing 150kg. Based on the various assumptions made. The results for stair ascent can be observed in Figure 2.20. It should be noted that to establish the profile of T_3, a linear law was used for the profile of a(t). Indeed, it is assumed that at the first and last contact between the prosthesis and the ground, the contact point is either at the heel or at the front of the foot, and between these two points, a linear approximation is used. The profiles of the GRF, forces F_x, F_z, F_1, F_2 and torque T_3 for the five different walking cycles are available in Appendix B.

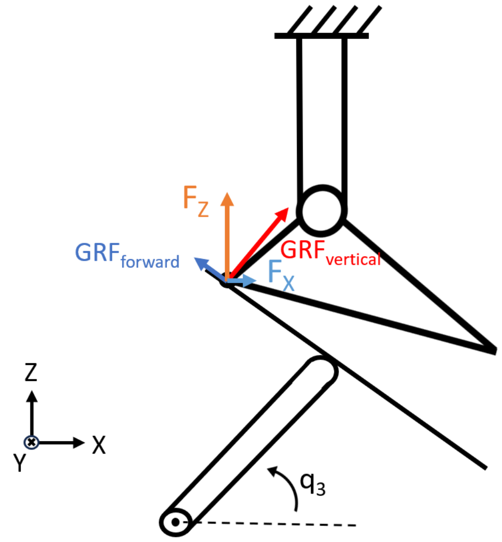

Figure 2.18: Representation of forces F_x and F_z as functions of the vertical and forward components of ground reaction forces on the prosthesis. Here, the forward ground reaction force is in the negative direction, in accordance with the situation.

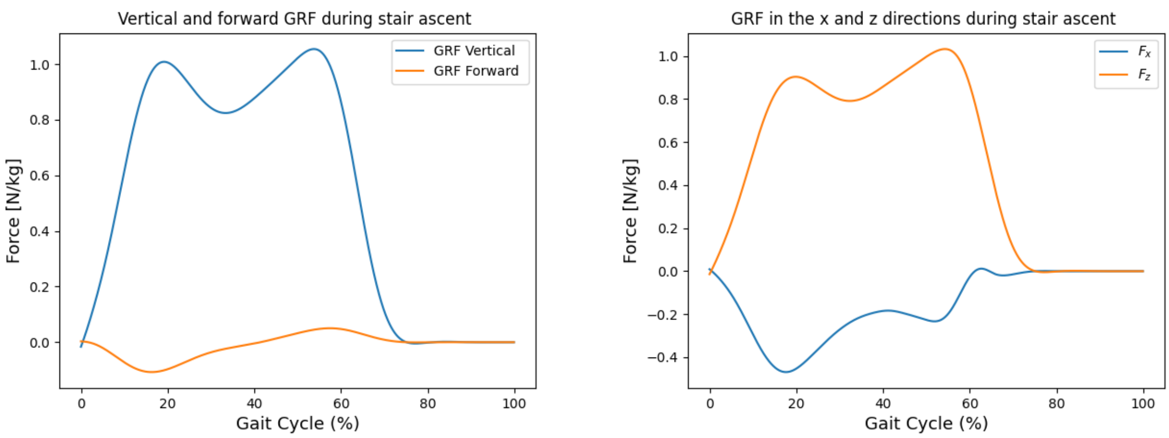

(a) Vertical and forward GRF

(b) GRF in the x and z directions

Figure 2.19: GRF relative to body weight in the sagittal plane during stair ascent

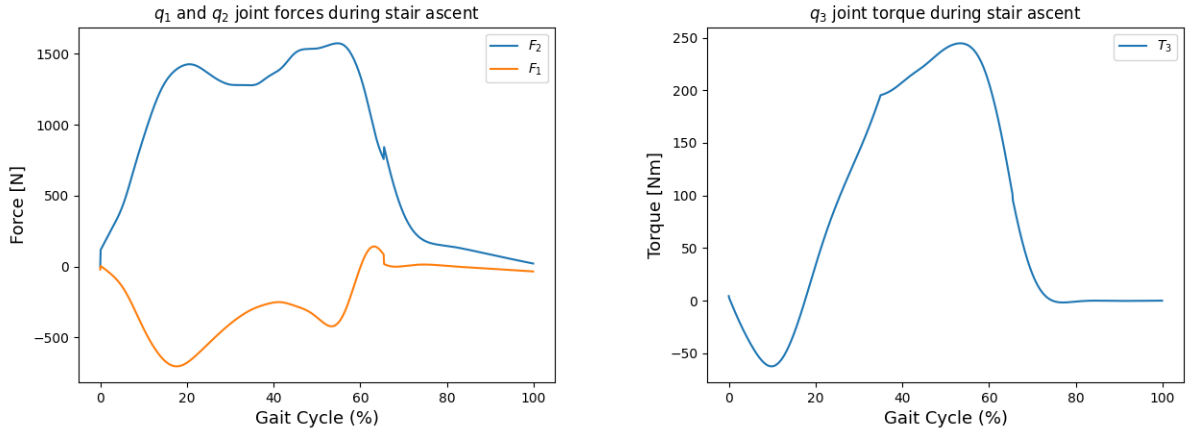

(a) q_1 and q_2 joint forces (b) q_3 joint torque

Figure 2.20: q_1, q_2 and q_3 force and torque profiles during stair ascent

2.6.6 Characterization summary

Now that we have established all the necessary profiles for characterizing the movements of our three joints, we can determine the maximum values of the various characteristics. In the tables 2.3 to 2.5, a summary of the values of the different characteristics of the movements of our three joints can be seen based on the various gait cycles. In these tables, the maximum values of the different characteristics are written in bold. For q_1, we can thus conclude that we need a minimum stroke length of 0.34m, the ability to achieve speeds of up to 1.15 m/s, accelerations of up to 19.5 m/s^2, and the capacity to provide forces of up to 969 N. For q_2, a minimum stroke length of 0.26m is required, along with the ability to reach speeds of up to 1.81 m/s, accelerations of up to 19.5 m/s^2, and the capability to deliver forces up to 1941 N. Finally, for q_3, we need a range of motion with a minimum of 105°, the ability to achieve speeds up to 6.65 rad/s, accelerations up to 138 rad/s^2, and we need a torque capacity of up to 292 Nm.

Characteristics	Flat ground	Slope ascent	Slope descent	Stair ascent	Stair descent
position [m]	0.14 – 0.21	0.21 – 0.25	0.16 – 0.28	0.16 – 0.23	**0.10 – 0.34**
velocity [m/s]	-0.35 – 0.4	-0.24 – 0.21	-0.47 – 0.37	-0.49 – 0.23	**-1.15** – 1.1
acceleration [m/s^2]	-7.41 – 7.35	-7.3 – 2.3	-6.25 – 5.22	-8.42 – 10.7	-16.6 – **19.5**
Force [N]	-141 – 436	-498 – 104	-585 – 195	-707 – 174	**-969** – 291

Table 2.3: summary table of q_1 characteristics for the different gait cycles

Characteristics	Flat ground	Slope ascent	Slope descent	Stair ascent	Stair descent
position [m]	0.02 – 0.23	**-0.03 – 0.253**	0.07 – 0.22	0.12 – 0.25	0.08 – 0.252
velocity [m/s]	-1.46 – 0.54	**-1.81** – 1.1	-1.43 – 0.63	-0.67 – 0.6	-0.77 – 1.25
acceleration [m/s^2]	-18.7 – 13.7	-17.6 – 22	-20.7 – **28.5**	-7.88 – 12	-21.2 – 20.9
Force [N]	0 – 1790	0 – 1648	0 – **1941**	0 – 1570	0 – 1784

Table 2.4: summary table of q_2 characteristics for the different gait cycles

Characteristics	Flat ground	Slope ascent	Slope descent	Stair ascent	Stair descent
q_3 position [°]	**-30** – 23	-1 – 57	-25 – 56	2 – 23	-7.94 – **74.7**
q_3 velocity [rad/s]	-4.05 – 3.69	-4.9 – 3.75	-6.08 – 3.54	-3.42 – 3.1	**-6.65** – 4.28
acceleration [rad/s^2]	-60.6 – 79.8	-83.1 – 73.8	-80.5 – 78.2	-74.3 – **138**	-91.2 – 129
Torque [Nm]	-270 – 273	-196 – 264	**-292** – 200	-62.5 – 245	-257 – 136

Table 2.5: summary table of q_3 characteristics for the different gait cycles

2.7 Selection of actuation and guidance systems

2.7.1 Actuator type

Now that the characterization phase is complete, we will proceed to the selection of actuation and guidance systems. To do this, the first thing we will determine is the type of actuator we will use, and by actuator type, we mean the power source of the actuator. Therefore, we have the option to choose between a hydraulic, pneumatic, or electric actuator.

In general, hydraulic actuators are particularly suitable for very large loads. In our case, where the loads do not exceed 2000 N, all three types of actuation can be suitable. On the other hand, pneumatic actuators have the advantage of being able to achieve very high speeds. Again, in this case, the speeds are relatively high, and all three types of actuators can be suitable. Now, looking at the disadvantages, both hydraulic and pneumatic actuators require specific components such as compressors and oil or air reservoirs, which can result in greater complexity in installation and more maintenance.

On the side of electric actuators, these are generally more compact installations, which can be very advantageous in this case since our three actuators are in series; hence, the weight and volume of these actuators need to be considered. Additionally, during the swing phase, all three actuators will need to be controlled in position. In the case of hydraulic and pneumatic actuation, this would require absolute position sensors for obtaining position feedback. In the case of an electric actuator, we can simply use an encoder on the motor along with a simple switch for calibration. Finally, it can also be stated that, in general, electric actuators offer more precise control in terms of position and speed compared to pneumatic and hydraulic actuators. For all the various reasons we have just mentioned, we will therefore opt for electric actuators.

2.7.2 Actuation and guidance of the rotational joint q_3

We will now proceed with the more detailed design of the actuation and guidance systems for our three joints. We will begin by designing the system for the rotational joint q_3. In fact, given that our three actuators are in series, the decisions made for the actuation and guidance of q_3 will directly impact the design of the actuation and guidance systems for q_1 and q_2.

First and foremost, as we have observed from equation 2.3, in order to limit the dynamic effects of the movement of the substitute ground as well as the effects of ground reaction forces on the torque of our actuator, it is crucial to minimize the values of 'd' and 'L_c3'. To achieve this, the platform used as substitute ground should be centered with respect to the axis of rotation, ensuring that its center of mass coincides with the rotation axis. A representation of the rotation shaft with the platform centered on the rotation axis can be observed in Figure 2.21.

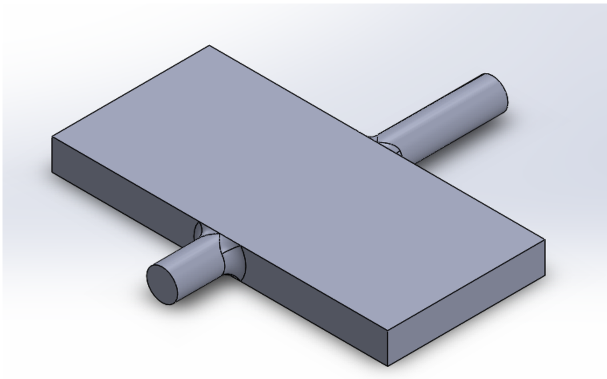

Figure 2.21: 3D representation of the combined rotation shaft and rotation platform serving as a substitute ground.

Next, to actuate this rotation shaft, we will choose to drive it using an electric motor directly coupled to the shaft in order to achieve a more compact system. To support and guide this rotation shaft, we will need to use bearings. The arrangement of these bearings to support the rotation shaft is of great importance for the actuation systems of q_1 and q_2. In fact, the placement of these bearings impacts the distribution of forces as well as the overall length of the rotation system that is supported by the installations of q_1 and q_2. To better understand the situation, we have depicted the kinematic diagram of the rotation shaft in two different scenarios in Figure 2.22. In these diagrams, the same axis system as in Figure 2.10 has been used, and it can be observed that the rotation shaft extends in the Y direction, whereas our two linear movements are in the XZ plane. Thus, it becomes apparent that forces in the x and z directions along the rotation shaft will induce significant bending moments on the guiding systems of q_1 and q_2.

If we assume that the motor and bearings are supported on a 'beam' attached to the linear actuator q_2 on side A in the kinematic diagram, we can observe that in the second configuration, the forces are closer to the attachment point, resulting in less bending. However, the motor will need to withstand higher radial forces, which is not ideal. To choose between these two configurations, we will conduct a static analysis of forces and moments for both scenarios. To do this, let's first establish the various forces and torque that can be observed on the free body diagrams :

- $F_{A,X}$ and $F_{A,Z}$: the radial forces exerted on the motor in the x and z directions.
- $C_{A,y}$ the torque generated by the motor.
- $F_{B,X}$ and $F_{B,Z}$: the forces exerted on the bearing between the motor and the platform in the x and z directions.
- $F_{C,X}$ and $F_{C,Z}$: the reaction forces of the prosthesis on the platform in the x and z directions.
- $F_{D,X}$ and $F_{D,Z}$: the forces exerted on the bearing at the end of the shaft in the x and z directions.

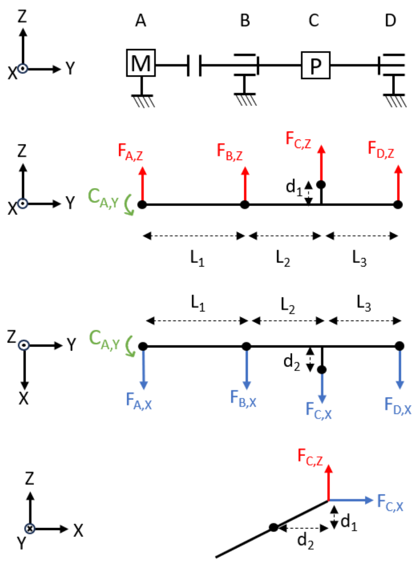

(a) First configuration

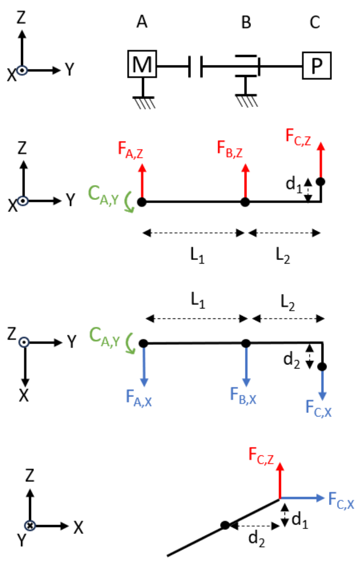

(b) Second configuration

Figure 2.22: Kinematic diagram and free body diagrams of the rotation shaft in two different configurations. For the first configuration (a), the motor is at A, bearings at B and D, and the platform at C. For the second configuration (b), the motor is at A, bearing at B, and the platform at C.

Now we can calculate the forces and moments for the first configuration :

- Along the Z axis :

$$\sum F = 0 : F_{A,Z} + F_{B,Z} + F_{C,Z} + F_{D,Z} = 0 \tag{2.15}$$

$$\sum M_B = 0 : L_1 F_{A,X} - L_2 F_{C,X} - (L_2 + L_3) F_{D,X} = 0 \tag{2.16}$$

- Along the X axis :

$$\sum F = 0 : F_{A,X} + F_{B,X} + F_{C,X} + F_{D,X} = 0 \tag{2.17}$$

$$\sum M_B = 0 : -L_1 F_{A,Z} + L_2 F_{C,Z} + (L_2 + L_3) F_{D,Z} = 0 \tag{2.18}$$

- Along the Y axis :

$$\sum M_B = 0 : C_{A,Y} - d_2 F_{C,Z} + d_1 F_{C,X} \tag{2.19}$$

Here, we will assume that we want an equal distribution of forces between the two bearings, meaning that $F_{B,Z} = F_{D,Z}$ and that $F_{B,X} = F_{D,X}$. With this assumption and by solving the system of equations, we find :

$$F_{D,X} = F_{B,X} = -\frac{L_1 + L_2}{2L_1 + L_2 + L_3} F_{C,X} \tag{2.20}$$

$$F_{A,X} = \frac{L_2 - L_3}{2L_1 + L_2 + L_3} F_{C,X} \tag{2.21}$$

$$F_{D,Z} = F_{B,Z} = -\frac{L_1 + L_2}{2L_1 + L_2 + L_3} F_{C,Z} \tag{2.22}$$

$$F_{A,Z} = \frac{L_2 - L_3}{2L_1 + L_2 + L_3} F_{C,Z} \tag{2.23}$$

We can see that if we set $L_2 = L_3$, our motor won't bear any radial load, and the forces applied to the platform will be evenly distributed between the two bearings. Now, let's examine the second configuration :

- Along the Z axis :

$$\sum F = 0 : F_{A,Z} + F_{B,Z} + F_{C,Z} = 0 \tag{2.24}$$

$$\sum M_B = 0 : L_1 F_{A,X} - L_2 F_{C,X} = 0 \tag{2.25}$$

- Along the X axis :

$$\sum F = 0 : F_{A,X} + F_{B,X} + F_{C,X} = 0 \tag{2.26}$$

$$\sum M_B = 0 : -L_1 F_{A,Z} + L_2 F_{C,Z} = 0 \tag{2.27}$$

- Along the Y axis :

$$\sum M_B = 0 : C_{A,Y} - d_2 F_{C,Z} + d_1 F_{C,X} \tag{2.28}$$

By solving the system of equations, we find :

$$F_{B,X} = -\frac{L_1 + L_2}{L_1} F_{C,X} \tag{2.29}$$

$$F_{A,X} = \frac{L_2}{L_1} F_{C,X} \tag{2.30}$$

$$F_{D,Z} = F_{B,Z} = -\frac{L_1 + L_2}{L_1} F_{C,Z} \tag{2.31}$$

$$F_{A,Z} = \frac{L_2}{L_1} F_{C,Z} \tag{2.32}$$

We can see here that our motor will inevitably bear radial loads. This might not be a problem as long as it stays within the motor's limits. We can try to limit these loads. For instance, if we set $L_1 = 4\ L_2$, our motor would only bear a quarter of the forces applied to the platform (which could be up to 500N of axial loads). However, if we assume that the forces at point C are applied at the center of the platform, and considering the platform's width of 15cm, L_2 would have to be at least 7.5cm. This would result in a minimum length of 30cm for L_1, thus negating the advantage of this configuration, which was to reduce the distances of force application (compared to a fixation on the motor side) to minimize bending moments on the guidings of q_1 and q_2. Consequently, we will opt for the first configuration.

2.7.3 Actuation and guidance of the prismatic joints q_1 and q_2

Let's now turn to the drive and guidance systems for our two linear movements. For electric linear actuators, there are various types of drives available, such as belt drives, screw drives, rack and pinion drives, or direct linear motor drives. Similarly, there are different types of guidance systems, including linear guides with ball chain technology or track roller guides. To make a choice among these options, we will refer to the NTN-SNR Linear Motion catalog [18]. NTN-SNR Linear Motion offers a comprehensive range of linear modules, encompassing all the aforementioned drive and guidance possibilities. This catalog provides a vast selection of modules that can meet our specific requirements. Furthermore, the catalog includes a detailed selection guide, aiding in the optimal solution selection process. Lastly, opting for both of our linear actuators from the same catalog will facilitate the coupling between the two actuators systems.

To make a selection among the various possibilities, several characteristics need to be taken into account, such as the stroke length, speed range, acceleration range, and the different forces the system will be subjected to. Through the characterization stage, we have already established some of these characteristics. However, linear actuation systems are particularly sensitive to potential buckling issues that may arise. Therefore, the complete dimensioning of the rotation system will be necessary to obtain accurate dimensions of the system and determine the moments and forces that the guidances of the two linear actuators will have to withstand.

2.8 Adjustment of the design model

After conducting research for the dimensioning of the rotation module, it quickly became apparent that the setup would have considerable size and mass. Thus, we realized that placing all 3 actuators in series was not a viable option due to their size and weight. Indeed, the comparison table of different design solutions (Table 2.2) may have underestimated the complexity of integrating 3 actuators in series. Taking this aspect into account, we understand that solutions 3 and 4 (Figure 2.6 and 2.7), which proposed splitting the 3 movements into 2, are more appealing. So, we will modify our design by opting to separate our 3 actuators. Keeping in mind the kinematic study of the actuator arrangement, we decide to separate the linear modules that will set the prosthesis in motion from the rotational movement that will drive the substitute ground. The representation of the new design can be observed in Figure 2.23.

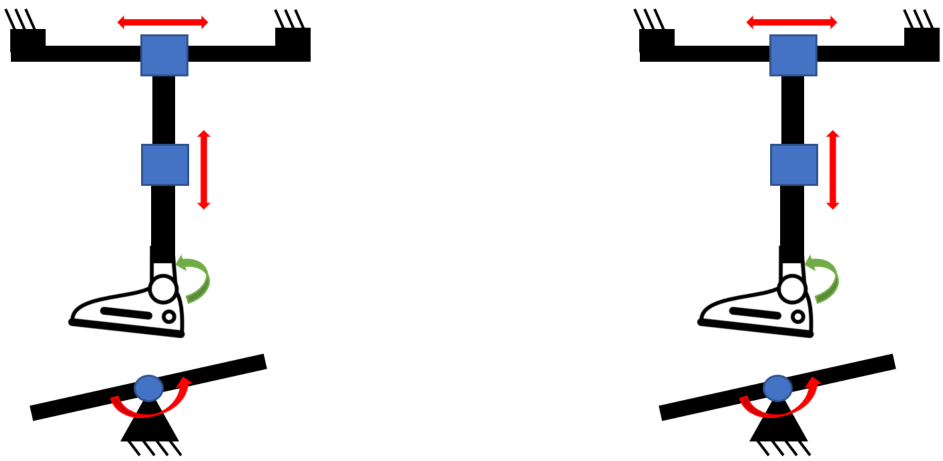

(a) Swing phase (b) Stance phase

Figure 2.23: New conceptual design after adjustment

This adjustment in the design does not bring any modifications to the characterization of velocities and accelerations since the kinematic constraints among the 3 joints remain valid. For joint q_3, the position profile remains exactly the same as before. However, for joints q_1 and q_2, their position profiles will simply be reversed. For instance, for q_2, instead of having to raise the substitution ground, it will now have to lower the prosthesis. The same reasoning can be applied to q_1. The kinematic model of the new solution can be found in the appendix C.1.

Regarding dynamics, as L_{c3} in equation 2.3 is assumed to be 0, there will be no changes for joint q_3 either. However, for joints q_1 and q_2, there will be some modifications. Their dynamic equations will no longer be affected by the movement of the rotation module but by that of the prosthesis which is preferable given that the prosthesis has less significant motion dynamics. The updated expressions for the dynamic equations of joints q_1 and q_2

can be seen in equations 2.33 and 2.34 . The complete derivation leading to these results can be found in Appendix C.2.

$$(m_1 + m_2 + m_p)\ddot{q_1} - (m_p L_{cp} sin(q_p))\ddot{q_p} - (m_p L_{cp} cos(q_p))\dot{q_p}^2 = F_1 - F_x \quad (2.33)$$

$$(m_2 + m_p)\ddot{q_2} + (m_p L_{cp} cos(q_p))\ddot{q_p} - (m_p L_{cp} sin(q_p))\dot{q_p}^2 + (m_2 + m_p)g = F_2 - F_z \quad (2.34)$$

with m_p as the mass of the prosthesis, L_{cp} as the distance between the center of the prosthesis joint and its center of mass, and q_p representing the angular position of the prosthesis center of mass.

Ultimately, in the characterization of our three actuators, only the forces that the linear actuators will need to provide will vary. To estimate these forces, we will use the new dynamic equations and and make new assumptions. Firstly, based on the previously mentioned linear module catalog [18], we now estimate masses of 15 kg for each linear module. Then, for the center of mass of the prosthesis, we will use its geometric center, resulting in $L_{cp} = 82$ mm. Lastly, utilizing the new profiles of positions, velocities, and accelerations (simply inverted) for q_1 and q_2, along with the new dynamic equations and considering the prosthesis mass and geometry, we determine the following forces for the two linear actuators :

Characteristics	Flat ground	Slope ascent	Slope descent	Stair ascent	Stair descent
Force q_1 [N]	-469 – 170	-106 – 514	-223 – 594	-224 – 715	-375 – **970**
Force q_2 [N]	-1638 – 84	-1581 – 80	**-1778** – 108	-1456 – 76	-1671 – 98

Table 2.6: summary table of actuation force ranges for q_1 and q_2 for the different gait cycles

So we finally observe that this design change has relatively little impact on the characterization of our actuators. The choices made in section 2.7 regarding the actuation and guidance systems of our 3 modules remain valid. However, this design change serves its purpose well. Indeed, the significant volume and weight of the substitution ground rotation system would have posed major constraints in terms of the problem of buckling that linear actuation systems can encounter.

Chapter 3

Test bench sizing

This chapter will provide detailed sizing of all the parts and components of this test bench. This is a crucial step in ensuring that each component of the test bench will meet its assigned characteristics and withstand the conditions of use. To achieve this, for each component, its characterization will be performed first, meaning the specific requirements imposed by the test bench for that component will be determined. Then, a selection will be made from all available possibilities to optimally meet the requirements while maintaining a certain safety margin. Finally, depending on the new features the component provides, we need to check that all the requirements have been met.

3.1 Rotary module

3.1.1 Rotary shaft and platform

First, we will address the sizing of the rotating shaft, a critical step to guarantee its ability to withstand applied forces. The initial focus will be on the static sizing of the shaft, followed by dimensioning the weld, and concluding with fatigue sizing of the shaft.

Static sizing

As the static study of forces and moments on the rotation axis has already been realised in section 2.7.2, we can directly generate the internal force diagrams using the same notations as before. Creating the internal force diagrams will allow us to assess the most critical section of the shaft. These diagrams can be observed in the figure 3.1.

We can observe that it is at point C where the shaft will experience the highest bending and torsional moments. If the shaft were to fail, it is highly likely to occur at this location. Therefore, we will focus on point C for sizing the shaft. Now, we can determine an initial estimation of the required shaft diameter (with a constant cross-section) using the Von

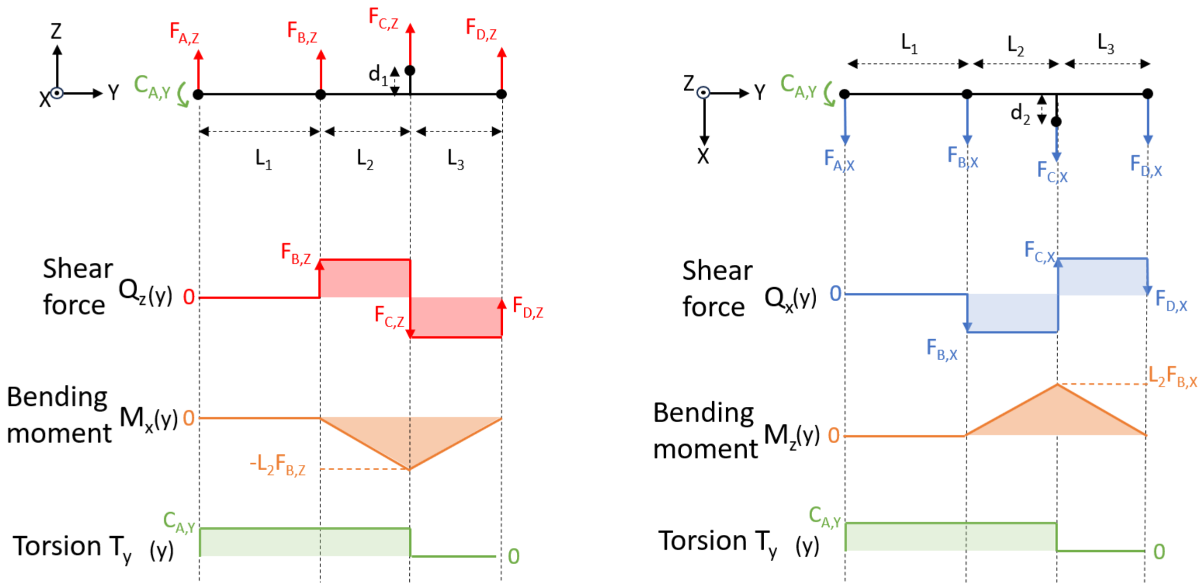

(a) Diagrams of the shear force in Z along Y axis, of the bending moment in X along Y axis and of the torsion in Y along Y axis

(b) Diagrams of the shear force in X along Y axis, of the bending moment in Z along Y axis and of the torsion in Y along Y axis

Figure 3.1: Internal force diagrams of the rotating shaft

Mises criterion. To do this, we first need to calculate the Von Mises equivalent stress (σ_e) at point C of the shaft :

$$\sigma_e = \sqrt{\sigma_{max}^2 + 3\tau_{max}^2} \tag{3.1}$$

In the equation 3.1, σ_{max} is the maximum normal stress of the circular section of the shaft, and τ_{max} is the maximum tangential stress of the same section. In this case, there are no tensile/compressive forces on the section, so the maximum normal stress is simply composed of the bending moments in the x and z directions. The maximum bending moment is calculated using the equation 3.2. Over all five different gait cycles, we found a maximum equivalent bending moment of 104.84 Nm. For pure bending, the normal stress is given by $\frac{Mx}{I}$ where M is the bending moment, I the moment of inertia of the cross section with respect to the neutral axis and x is the distance from the neutral axis. For a circular section shaft, the maximum normal stress is thus given by the equation 3.3 where d is the diameter of the shaft. Next, to determine the maximum tangential stress, we need to compare whether the torsion or the shear component will yield the highest stress. For a circular section shaft, the tangential stress due to torsion is given by the equation 3.4, while the shear stress is given by the equation 3.5 where $Q_{C,max}$ is the maximum equivalent radial load and d the diameter of the shaft. Over all five different gait cycles, the maximum equivalent radial load is $1907N$, so the diameter of the shaft should be at least 46cm for the tangential stress due to shear to be greater than the tangential stress due to torsion. Therefore, we will use the equation 3.4 for the expression of the maximum tangential stress. Finally, we can express the Von Mises equivalent stress as given in the equation 3.6.

$$M_{c,max} = \sqrt{M_{C,x}^2 + M_{C,Z}^2} = 104.84Nm \tag{3.2}$$

$$\sigma_{max} = \frac{32M_{C,max}}{\pi d^3} \tag{3.3}$$

$$\tau_{max} = \frac{16T_{C,Y}}{\pi d^3} \tag{3.4}$$

$$\tau_{max} = \frac{16Q_{C,max}}{3\pi d^2} = 16\frac{\sqrt{Q_{C,x}^2 + Q_{C,Z}^2}}{3\pi d^2} \tag{3.5}$$

$$\sigma_e = \sqrt{\sigma_{max}^2 + 3\tau_{max}^2} = \sqrt{(\frac{M_{c,max}}{\frac{\pi d^3}{32}})^2 + 3(\frac{T_{c,y}}{\frac{\pi d^3}{16}})^2} \tag{3.6}$$

Now, to make an initial estimation of the diameter of the constant-section shaft, we need to compare the Von Mises equivalent stress with the material's yield strength (S_y) divided by a safety factor. For the material, for a first estimation, we choose an aluminum alloy 6061-T6 with a yield strength of 275 MPa as provided by the 'Fundamentals of Machine Component Design' [19]. We use a safety factor 'SF' of 2 for 'well-known materials, under reasonably constant environmental conditions, subjected to loads and stresses that can be determined readily' as recommended by [19].

$$\frac{S_y}{SF} \geq \sigma_e \Leftrightarrow d^3 \geq \frac{16SF}{\pi S_y}\sqrt{(2M_{c,max})^2 + 3(T_{c,y})^2} \Leftrightarrow d \geq 0.02727m \tag{3.7}$$

For the platform, we know that it has a length of 32cm and a width of 15cm, but now we need to calculate the minimum thickness 'h' required to prevent the platform from failing under the applied forces. To size this platform, we will consider the worst-case scenario, which is when the prosthesis applies forces on only one side of the platform and at its end. The section that is most likely to fail is therefore the 15cm wide and 'h' high section at the center of the platform. The dominant stress in this section is the normal stress due to pure bending caused by the force applied at the end of the platform perpendicular to it. This bending moment has a maximum value of $M_{max} = 292Nm$, and we can calculate the maximum normal stress for a rectangular cross section as given by the equation 3.8. Next, since the normal stress is dominant in the expression of the Von Mises equivalent stress, we can directly use the Von Mises criterion to determine the minimum required thickness 'h'. Using the same material and safety factor as before, we find a minimum thickness of 9.21 mm as shown in the equation 3.9.

$$\sigma_{max} = \frac{6M_{max}}{0.15h^2} \tag{3.8}$$

$$\frac{S_y}{SF} \geq \sigma_e \Leftrightarrow \frac{S_y}{SF} \geq \frac{6M_{max}}{0.15h^2} \Leftrightarrow h \geq 9.21mm \tag{3.9}$$

To create the shaft-platform assembly, the initial idea was to manufacture both parts as a single piece with an equivalent thickness of the shaft and platform, as shown in Figure 3.2a . However, as observed from the previous calculations, the platform's thickness is much smaller than that of the shaft. Adopting this design would result in significant material wastage and a substantial increase in rotational inertia. Therefore, considering manufacturing the shaft and the platform separately and then joining them together using an assembly technique appears to be a much better approach. There are various assembly techniques possible. However, riveting would require drilling a hole through our shaft, leading to a very high stress concentration at that location, which would significantly increase the shaft diameter. On the other hand, adhesive bonding would not provide sufficient resistance against torsion. Finally, welding would require slight modifications to the shaft's shape to facilitate the process. This last option seems to offer a good compromise between the two, providing better strength than bonding and involving a lower stress concentration factor than drilling a hole in the shaft. This configuration can be seen on figure 3.2b.

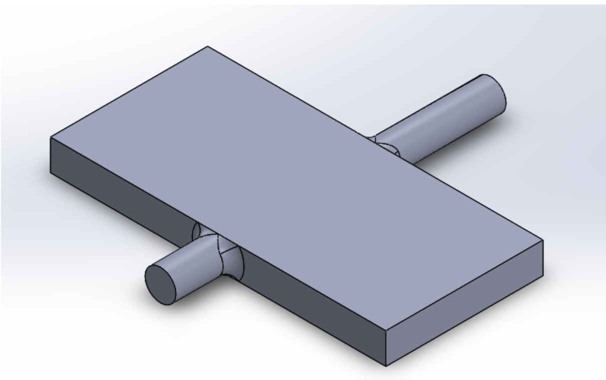

(a) 3D representation of the shaft-platform assembly in a single piece

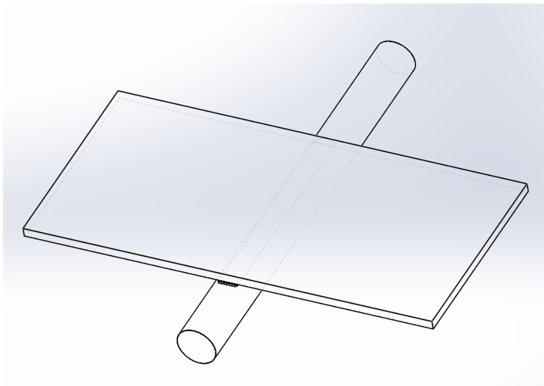

(b) 3D representation of the shaft and platform assembled by welding

Figure 3.2: 3D representation of the shaft-platform assembly in a single piece in (a) and by assembly in (b)

Weld sizing

In order to weld the platform and the shaft together, it will be necessary to calculate the minimum thickness of the welding joint to ensure it does not fail. For these calculations, the same procedure as in section 14.5 of the 'Fundamentals of Machine Component Design' [19] will be followed. First, let's define 'h' as the leg length of the weld. In this section, they explain that the significant stress on the weld is the shear stress in the throat section. The throat area is equal to tL where 'L' is the length of the weld and 't' is the throat length, defined as 'the shortest distance from the intersection of the plates to the straight line connecting the ends of the two legs' as shown on Figure 3.3.

For the calculation of the weld size, our situation is represented in Figure 3.4a . Here, we have two forces acting transversely on the two weld joints AD and BC, and one of these

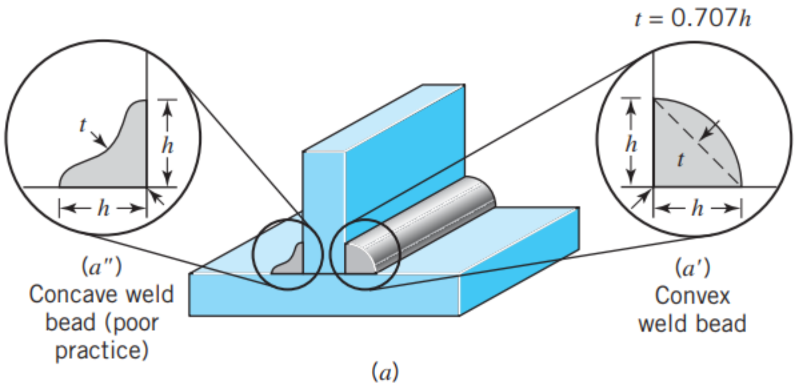

Figure 3.3: Throat length 't' of a fillet weld ; Figure 11.7 of the 'Fundamentals of Machine Component Design' [19]

forces induces bending on the joints. For the rest of the analysis, various assumptions drawn from [19] are made:

1. For calculating moments of inertia of the weld linear segments, the effective weld width in the weld plane is the same as the throat length t.
2. The throat length dimension t is assumed to be very small in comparison with other dimensions.
3. The transverse shear stress is given by V/A where V is the shear force and A is the weld throat area.
4. The resultant shear stress acting in the plane of the weld throat is the resultant of the bending and transverse shear stresses.
5. The distortion energy theory is applicable for estimating the shear yield strength of the weld material.

The bending moment is equal to (1840)(0.16) $= 294.4Nm$. The moment of inertia about the neutral bending axis (dotted line on Figure 3.4a) consists of the contributions of the two weld : $I = I_{AD} + I_{BC}$ where $I_{AD} = I_{BC} = 0.15td$ with d the distance between the weld and the neutral bending axis ($= \frac{0.015}{2}$). So the bending stress on the weld AD is equal to :

$$\sigma = \frac{Md}{I} = \frac{(294.4)(\frac{0.015}{2})}{(0.15)t(\frac{0.015}{2}^2)} = \frac{130.84}{t}[kPa] \tag{3.10}$$

And the transverse shear stresses on all welds are :

$$\tau_1 = \frac{V}{A} = \frac{590}{(0.15+0.15)t} = \frac{1.966}{t}[kPa] \tag{3.11}$$

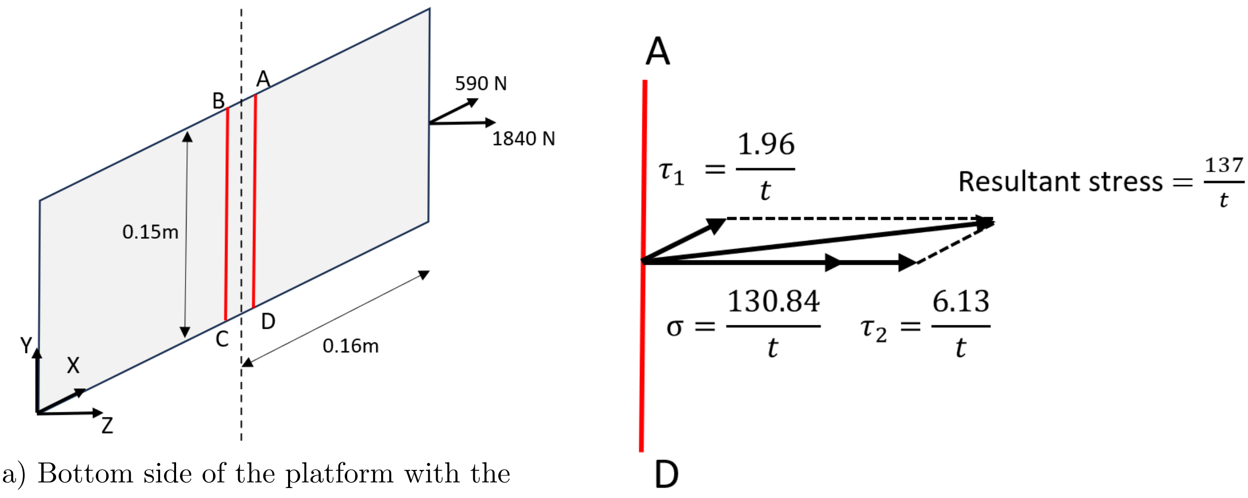

(a) Bottom side of the platform with the two forces applied to the platform shown and in red the AD and BC welds

(b) Stresses on weld AD in [kPa]

Figure 3.4: Representation of the situation for calculating the thickness of the weld joint

$$\tau_2 = \frac{V}{A} = \frac{1840}{(0.15 + 0.15)t} = \frac{6.133}{t}[kPa] \tag{3.12}$$

As can be seen from Figure 3.4b, the resultant stress of the bending and transverse shear stresses on the weld joint AD is equal to $\frac{137}{t}[kPa]$. Let's now suppose that this resultant stress acts in the plane of the weld throat. Using the distortion energy theory to obtain an estimated shear yield strength and using the same material and safety factor as before we have :

$$\frac{0.58S_y}{SF} \geq \frac{137}{t} \Leftrightarrow t \geq 1.72mm \tag{3.13}$$

In this case, the angle between the welded surfaces is 30 degrees instead of 90. The leg length of the weld 'h' is thus equal to $\frac{t}{cos15}$ which gives $h \geq 1.78mm$. However, for practical reasons it is not usual to have a leg length less than 3mm.

In order to make the welding of the two pieces possible, it was necessary to slightly modify the geometry of the shaft, as shown in Figure 3.5 . This flat section will introduce stress concentrations at that place of the shaft. Therefore, a stress concentration factor 'K_t' needs to be considered for the shaft diameter calculation. To choose this factor, we will consider the flat section as a shaft fillet (see Figure 3.6), with the small radius 'r' equal to the smallest distance between the flat and the center of the shaft, which will result in an overestimated factor. Referring to Figure 3.6, stress concentration factors of 1.3 for bending and 1.15 for torsion are obtained by using assumption that the flat is small compared to the shaft so the ratio $\frac{d}{D} = 1.1$ and to decrease as much the stress concentration factor $r = 5mm$. By taking into account the stress concentration factors, we obtain:

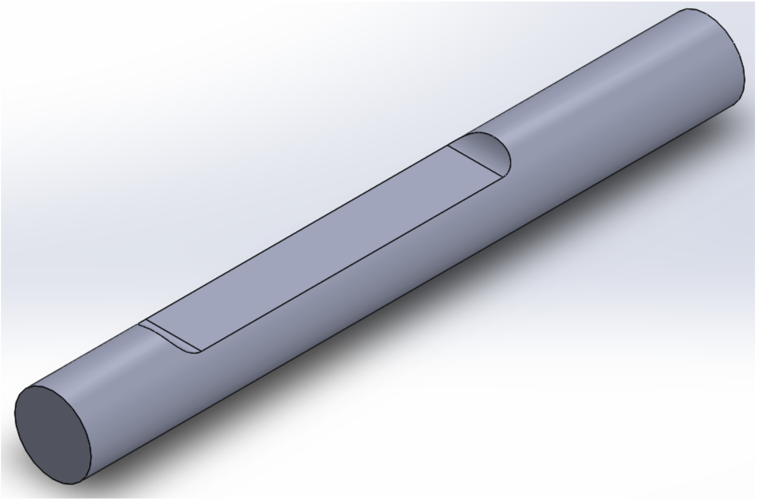

Figure 3.5: 3D representation of the shaft

$$\frac{S_y}{SF} \geq \sigma_e \Leftrightarrow d^3 \geq \frac{16SF}{\pi S_y}\sqrt{(2(1.3)M_{c,max})^2 + 3(1.15T_{c,y})^2} \Leftrightarrow d \geq 0.02876m \qquad (3.14)$$

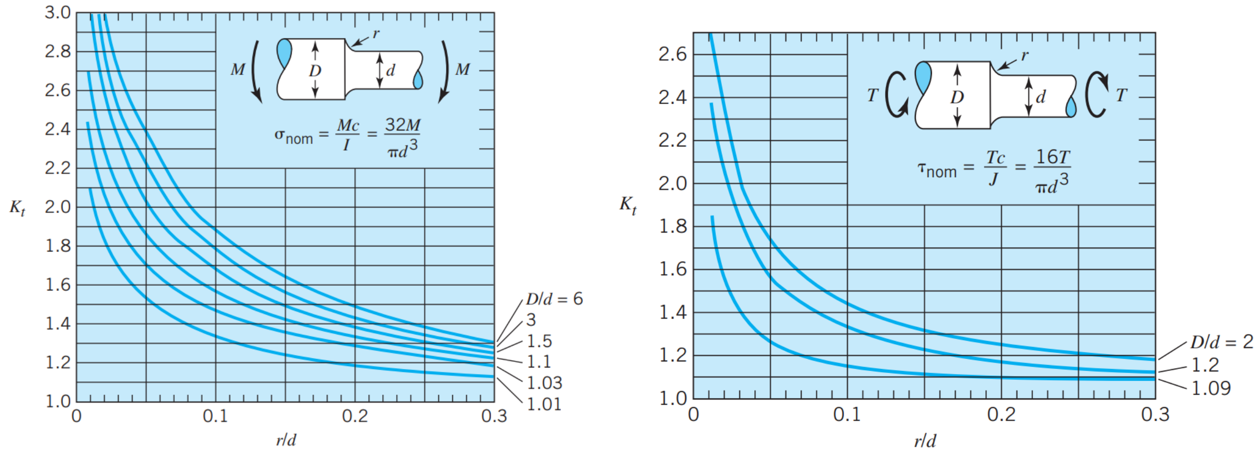

(a) (b)

Figure 3.6: Stress concentration factor for a shaft fillet for (a) bending ; (b) torsion ; Figure 4.35 of the 'Fundamentals of Machine Component Design' [19]

Fatigue sizing

Finally, to complete the sizing of our two components, we need to consider that they will be cyclically loaded for numerous cycles. The shaft and the platform will be subject to fatigue, which, over time, can cause the failure of the component. To ensure this doesn't happen, we will construct the 'fatigue strength diagram' for both components and graphically verify that the previously determined shaft diameter/platform thickness will withstand fatigue.

Let's begin by dimensioning the shaft for fatigue. For the shaft, we first need to find the fatigue stress concentration factor K_f in the expressions for stress due to bending and torsion. This parameter is calculated using the following formula:

$$K_f = 1 + (K_t - 1)q \tag{3.15}$$

with K_t the stress concentration factor and q the notch sensitivity factor. Using the previously found values for K_t and finding a value of 0.8 for q using Figure 8.24 of [19], we obtain:

$$\begin{aligned} K_{f,b} &= 1,24 \quad \text{for bending} \\ K_{f,t} &= 1,12 \quad \text{for torsion} \end{aligned}$$

Then, after examining the torque graphs for the shaft, we observe that it will experience alternating torsion. For bending, we will assume it remains constant and take its maximum value. We can now calculate the following values for the critical section of the shaft :

- The maximum equivalent alternating stress : $\sigma_{ea,max} = SF\frac{16T_{max}}{\pi d^3}K_{f,t} = 123[MPa]$
- The maximum equivalent mean stress : $\sigma_{em,max} = SF\frac{32M_{max}}{\pi d^3}K_{f,t} = 98[MPa]$
- The ultimate shear strength : $S_{us} = 0.8S_u = 248[MPa]$
- The shear yield strength : $S_{sy} = 0.58S_y = 159.5[MPa]$
- The endurance limit : $S_n = 0.5S_uC_LC_GC_SC_TC_R = 56.18[MPa]$

with S_u the ultimate tensile strength (310 [MPa] for 6061 - T6 aluminium alloy), S_y the tensile yield strength (275 [MPa] for 6061 - T6 aluminium alloy), C_L the load factor, C_G the gradient factor, C_S the surface factor, C_T the temperature factor and C_R the reliability factor (values are found in the Table 8.1 of [19]).

With the various calculated values, we can now plot the fatigue strength diagram for critical section of the shaft. This diagram is shown in Figure 3.7a where we can see that the operating stress, composed of the equivalent alternating and mean stresses in the critical section of the shaft, is above the strength limits of the shaft. To address this issue, we can start by using a better material. In our case, the 2014-T6 aluminum alloy seems like a good choice. Indeed, the material has an ultimate tensile strength of 485 MPa, a tensile yield strength of 415 MPa, is easily machinable and exhibits good weldability by arc welding. Then we can also increase the shaft diameter. Finally, with the 2014-T6 aluminum alloy as material and a 36mm shaft diameter we can see on Figure 3.7b that the operating stress is below the strength limits of the shaft. Please note that the calculated diameter of 36mm is the diameter at the center of the flat and since the flat has a thickness of 2mm, the final diameter of the shaft is 40mm.

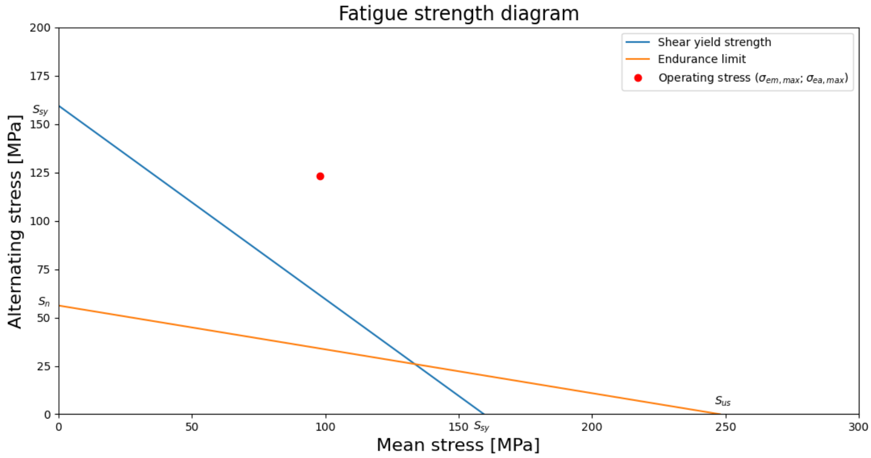

(a) with a 30mm shaft diameter and 6061-T6 aluminium alloy

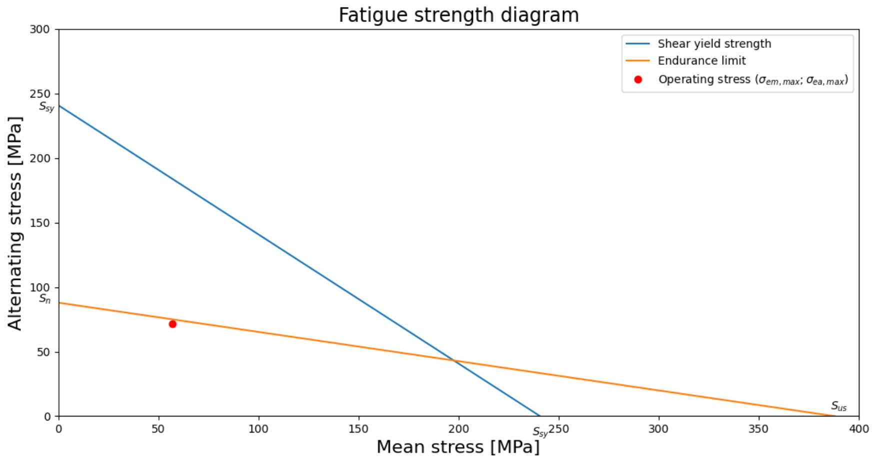

(b) with a 36mm shaft diameter and 2014-T6 aluminium alloy

Figure 3.7: Fatigue strength diagram of the critical section of the shaft with the shear yield strength in blue, the endurance limit in orange and the operating stress composed of the equivalent alternating and mean stresses in red.

Let's now move on to the fatigue dimensioning of the platform. The forces applied by the prosthesis on the platform always produce a bending moment of the same sign throughout the entire cycle. Therefore, we can consider that the platform is subjected to alternating bending and mean bending. The bending moment ranges from 0 to a value M_{max} over the course of one cycle, so we can consider that the alternating and mean bending moments are both equal to $\frac{M_{max}}{2}$. Hence, we can calculate the alternating and mean stresses on the critical section of the platform as follows (with a width of 15cm and a thickness h) :

$$\sigma_{ea,max} = SF\frac{3M_{max}}{0.15h^2} \tag{3.16}$$

$$\sigma_{em,max} = SF\frac{3M_{max}}{0.15h^2} \tag{3.17}$$

For the fatigue strength diagram, as we are dealing with alternating bending rather than alternating torsion, we need to adjust the various factors according to Table 8.1 of [19] for calculating the endurance limit. For alternating bending, we also need to use the tensile yield and ultimate strengths (S_y and S_u) instead of the yield and ultimate shear strengths (S_{sy} and S_{us}). Then, using the values of $\sigma_{ea,max}$ and $\sigma_{em,max}$ with a safety factor of 2, the tensile and yield strengths of the aluminum alloy 2014-T6, and the minimum thickness of 9.21mm calculated previously, we can plot the fatigue strength diagram as shown in Figure 3.8a. On this diagram, we can see that the operating stress is above the endurance limit of the shaft. However, on Figure 3.8b, we can see that a thickness of 11mm is sufficient to withstand fatigue.

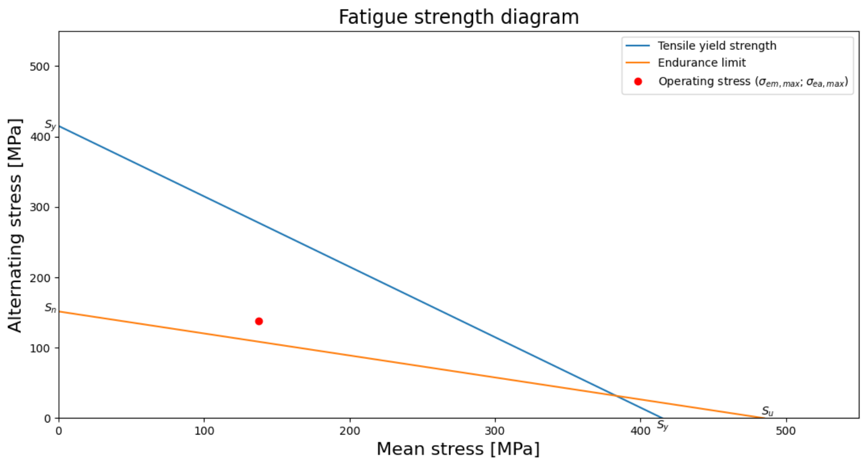

(a) with a 9.21mm platform thickness and 2014-T6 aluminium alloy

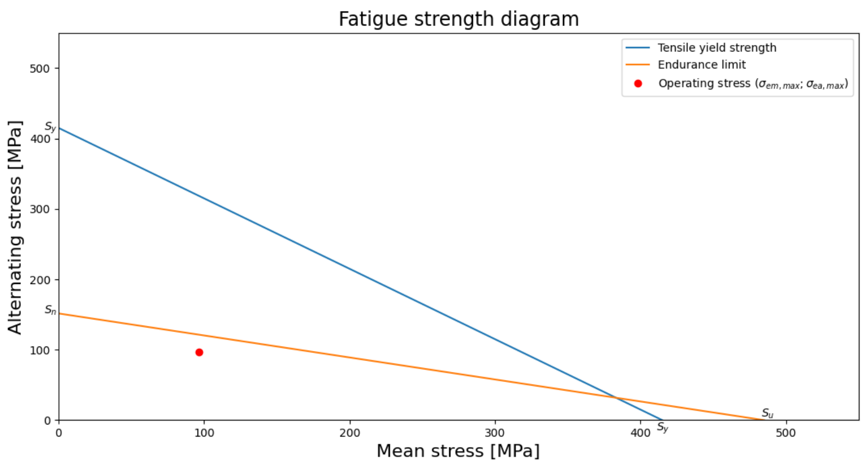

(b) with a 11mm platform thickness and 2014-T6 aluminium alloy

Figure 3.8: Fatigue strength diagram of the critical section of the platform with the yield strength in blue, the endurance limit in orange and the operating stress composed of the equivalent alternating and mean stresses in red.

3.1.2 Gear motor assembly

To set the rotation platform of the test bench in motion, we will need to use a motor. Typically, these motors have a high rotational speed and a low torque. However, in our case, we require a relatively low speed range and a very high torque. Therefore, we will need a gearhead that, based on its reduction ratio, will increase the torque and proportionally reduce the speed. Thus, we are currently searching for a gear motor assembly. To select this assembly, one approach is to start by choosing a suitable gearhead, determine the optimal reduction ratio, and then select a compatible motor that best meets the requirements. In this case, the challenge of finding motors that meet our specific requirements led us to first identify motors that could potentially meet the demands based on a certain reduction ratio. Subsequently, we sought a compatible gearbox while ensuring that, considering the gearbox efficiency, all requirements are still met.

First, we need to select to motor type that we need. As revealed by establishing the position, velocity, and acceleration profiles of the rotary actuator through kinematics, the motor must possess a high dynamic performance. Additionally, it should be precisely controlled in position while providing extremely high torque. Consequently, the choice of motor type has led us to opt for a direct current (DC) servo motor. Based on the previously established profiles, the characteristics of the motor are the following :

1. Peak torque : 292 Nm
2. RMS torque : 145 Nm
3. Maximum power : 1055 W
4. RMS power : 385 W
5. Maximum speed : 64 rpm

Generally, the limitations of a motor are of thermal origin. During motor operation, losses generate heat within the motor, and the motor has a certain capacity to dissipate this heat. If the dissipation of this heat is not efficient enough, the temperature within the motor may increase, leading to a decrease in motor efficiency. Excessive temperature within the motor can even significantly reduce its lifetime. The principal losses in an electrical motor are due to Joules losses in the electrical wires. They can be expressed as $P = RI^2$ where R is the electrical resistance of the wires in ohm and I the current in ampere. A simple thermal model of the motor can be established :

$$RI^2 = h\Delta T = \frac{T_{mot} - T_{amb}}{R_{th}} \tag{3.18}$$

with h the heat dissipation coefficient in [W/K], T_{mot} the temperature of the motor in Kelvin, T_{amb} the ambient temperature in Kelvin and R_{th} the thermal resistance of the motor in [K/W].

	AKM2G-44NL	AKM2G-42PL	AKM2G-43NL
Peak Torque [Nm]	27.1	14.5	21.2
Rated Torque [Nm]	8.2	4.73	6.65
Rated Speed [rpm]	1400	2800	1900
Rated Power [kW]	1.2	1.39	1.32

Table 3.1: AKM2G-44NL, AKM2G-42PL and AKM2G-43NL servo motors key characteristics.

As the current I in the motor's wires can be expressed as the product between the torque constant K_t in [A/Nm] and the torque supplied by the motor C in [Nm], the equation becomes :

$$RK_t^2C^2 = \frac{T_{mot} - T_{amb}}{R_{th}} \tag{3.19}$$

We can see that the motor operation is thus limited by a maximum continuous torque. In fact, in the technical sheet of a motor is given the motor's operating range, which is limited by the maximum continuous torque and maximum permissible speed. However, temporarily higher torques are permitted up to a certain limit which is the peak torque.

For the motor selection, we use the catalog from Kollmorgen of the 'AKM2G Low voltage Servo Motor' series [20], where some motors could meet our requirements. In this catalog, we are considering three different models. These models are listed in the table 3.1 below along with their key characteristics :

For each of these motors, we can calculate the maximum possible reduction ratio for their gearhead by dividing the maximum motor rotational speed by the maximum rotational speed required at the output of the gearhead :

$$i_{max_{44NL}} = \frac{1400}{64} = 21.875 \ \ ; \ \ i_{max_{42PL}} = \frac{2800}{64} = 43.75 \ \ ; \ \ i_{max_{43NL}} = \frac{1900}{64} = 29.875 \tag{3.20}$$

Using a selection tool from Micron [21], compatible gearheads for the different motor models were found by specifying certain parameters such as reduction ratio, torque, speed and loads requirements, and the motor model. All three gearheads are from the 'ValueTrue Planetary Gearhead ' range of the catalog from 'Thomson Linear Motion Optimized' [22] in collaboration with Micron. The three different gearheads models are as follows : VT010-020-0 RM100-40, VT010-040-0 RM100-40 and VT010-025-0 RM100-40 for the AKM2G-44NL, AKM2G-42PL and AKM2G-43NL respectively. Their reduction ratio are 20, 40 and 25 respectively. They all have two stages of reduction and an efficiency coefficient of 0.9. By considering the reduction ratio and efficiency, we can recalculate the various key values at the output of the different gear motor assemblies in the following table 3.2:

	Gear motor assembly 1	Gear motor assembly 2	Gear motor assembly 3
Reduction ratio	20	40	25
Efficiency	0.9	0.9	0.9
Peak Torque [Nm]	487.8	522	477
Rated Torque [Nm]	147.6	170.28	149.625
Rated Speed [rpm]	70	70	76
Rated Power [kW]	1.08	1.251	1.188

Table 3.2: Key characteristics of the three different gear motor assemblies where AKM2G-44NL VT010-020-0, AKM2G-42PL VT010-040-0 and AKM2G-43NL VT010-025-0 correspond respectively to the gear motor assembly 1, 2 and 3.

Analyzing table 3.2, we can observe that all three motors meet our requirements in terms of peak torque, maximum speed, and power. For the nominal torque (or rated torque), to ensure thermal compatibility with our demands, the nominal torque of the motor must be higher than the RMS torque required by our application. Therefore, we select the AKM2G-42PL motor, which provides a larger margin concerning the nominal torque. Now, we can perform a thermal verification of the motor graphically, as shown in Figure 3.9 where we can see that the highest RMS torque among the 5 different operating cycles at maximum speed falls within the continuous operating range of the motor. We can also graphically verify that the most constraining operating points of the five different gait cycles are all below the peak torque curve of the motor.

After selecting the motor model, the next step is to choose from the various available options. The first option is a holding brake. This brake is designed to maintain a specific position when the motor is at rest, providing a blocking torque that eliminates the need for continuous motor power. It is not intended for dynamic braking. To put the motor back into motion, the holding brake must first be released. This feature can be highly beneficial for this test bench, especially when performing static loading tests on the prosthesis. However, there are some drawbacks to consider when adding this option to the motor. It will increase the motor's length by 5 cm, add a mass of 1.36 kg, and introduce an inertia of 0.36 $kgcm^2$ [20]. However, since the three actuators are no longer in series, adding length and mass to the motor is no longer a concern. Regarding inertia, it is essential to verify whether the chosen motor is still capable of providing sufficient torque when considering the additional inertial moment of the rotor of the motor, the holding brake, and the reducer in the actuator's dynamic equation. With the 3D model, we found that the final value of the moment of inertia of the rotating shaft and platform was 0.04293 kgm^2. The inertial moment of the motor and the holding brake is 1.72 10^{-4} kgm^2, and to transfer this value to the output of the reducer, it needs to be multiplied by the reduction ratio since the motor's rotor will rotate 40 times faster than the output rotor of the reducer.

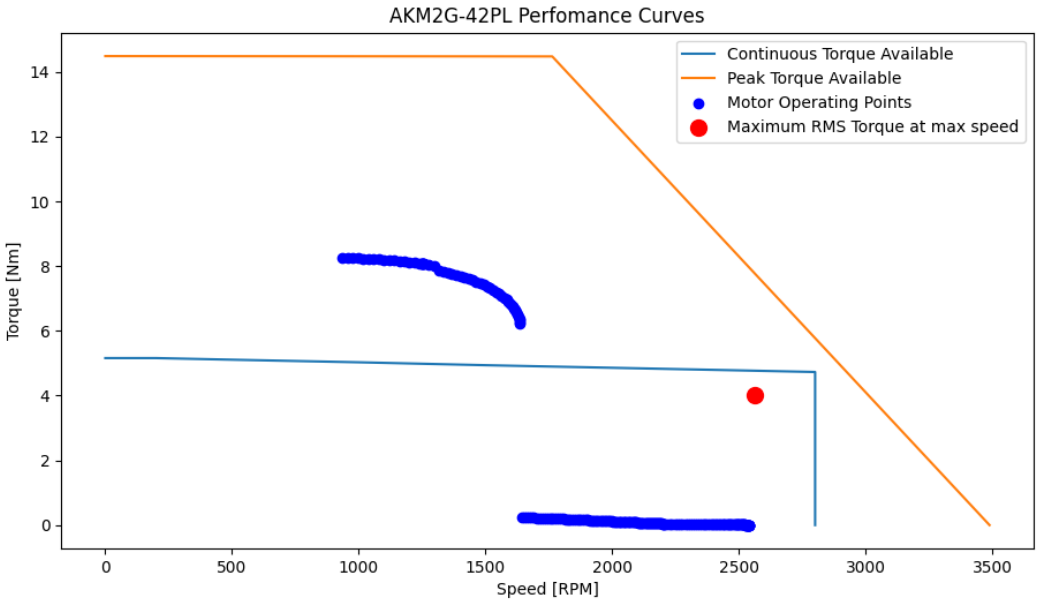

Figure 3.9: Thermal verification of the AKM2G-42PL servo motor with its performance curves [20], the most constraining operating points of the motor in blue and the maximum RMS torque at maximum speed in red.

Then, as the inertia of the gear head is $0.79\ 10^{-4}\ kgm^2$, the new total inertia is :

$$I_3 = 0.04293 + 40 * 1.72\ 10^{-4} + 0.79\ 10^{-4} = 0.0498 kgm^2 \tag{3.21}$$

This new value does not imply any significant change, and our motor is still well-suited. The second option concerns the motor feedback, for which four different possibilities are presented in figure 3.10.

AKM2G LV Servo Motor Feedback Summary

Available Models⁵	Code	Description	Connector	Type	Size	Motor ID Support³	Accuracy¹,² (arc-sec)	RMS Noise¹ (arc-sec)	Resolution	Absolute revs.
3, 4	2-	Commutating Encoder	C/G	Optical	15	No	±218.2"	N/A	12 bits	None
2, 3, 4	GU	HIPERFACE DSL®	D	Capacitive	EEM37	Yes	±240"	±20"	17 bits	4096
2, 3, 4	LD	EnDat® 2.2	D	Inductive	EQI 1131	Yes	±120"	See Note 4	19 bits	4096
3, 4	R-	Resolver	C/G	Inductive	15	No	±540"	N/A	24 bits for AKD	1

Figure 3.10: AKM2G Low Voltage Servo Motor Feedback Summary from [20]

As the gear head VT010-040-0 has a precision of 4 arc-min (= 0.0666 degree), the optical encoder with a resolution of 0.088 degree and a precision of 218.2 arc-sec (= 0.06 degree) is largely sufficient. The final complete reference for this motor with these options is AKM2G-42PLANC22-10.

One can observe the 3D rendering of the final gear motor assembly in the image 3.11. The total mass of the assembly is 13.22 kg, its overall length is 42.84 cm, and the largest square section measures 10.1 cm per side [20][22].

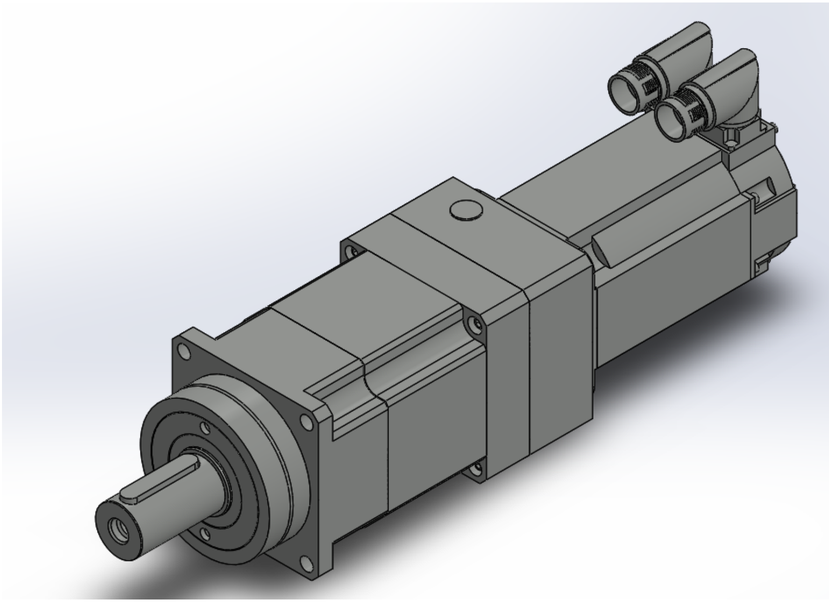

Figure 3.11: 3D rendering of the gear motor assembly (motor : AKM2G-42NLANC22-10 [20] ; gearhead : VT010-025-0 RM100-40 [22])

3.1.3 Coupling

In order to couple the output shaft of the gearbox with the rotation shaft, we will need to use a coupling. This coupling must be compatible with the output shaft of the gearbox, which has a diameter of 32mm with a keyway, and the rotation shaft, which has a diameter of 40mm. Furthermore, this coupling must also support a torsional torque of up to 292Nm. For this purpose, we will be using the BKL 300 32 PFN 40 1 metal bellows coupling from 'R+W' [23]. This coupling is easily mountable, has relatively low inertia, is compatible with both shafts, and has a nominal torque rating of 500Nm. Technical drawings of the coupling can be found in Appendix D.1. The coupling's placement in conjunction with the other modules can also be visualized in Figure 3.13.

3.1.4 Bearing units

To support and guide our shaft, we will also need bearing housings. As determined earlier, we will use two housings placed on either side of the platform. These housings should be compatible with the 40mm diameter of the shaft and be able to withstand equivalent radial loads up to 1907N. In this case, we will use the cast iron UCPH208 bearing housings, which can be found on the MISUMI website [24]. These housings have an inner diameter of 40mm and can comfortably support the required radial forces. These housings include setscrews. Since there are no axial forces acting on the shaft in our case (except for parasitic forces), we can constrain the axial displacement of the shaft using the setscrews on the housings. This eliminates the need to machine a shoulder on the shaft and weaken it. Technical drawings of the bearing housings are available in Appendix D.2. The housings can also be viewed along with the other modules in Figure 3.13.

3.1.5 Mounting bracket

The last mechanical component we need for the rotation module is a mounting bracket for the motor-reducer assembly. This bracket should match the precise dimensions of the reducer's mounting system. To achieve this, we have utilized a set of welded mounting plates that can be fully customized to our requirements on the MISUMI website [25]. An illustration of the bracket can be seen in Figure 3.12. For simplicity, the floor attachment holes have been aligned with those of the bearing housings. Technical drawings and complete reference of the mounting bracket are available in Appendix D.3. The bracket can also be viewed alongside the other modules in Figure 3.13.

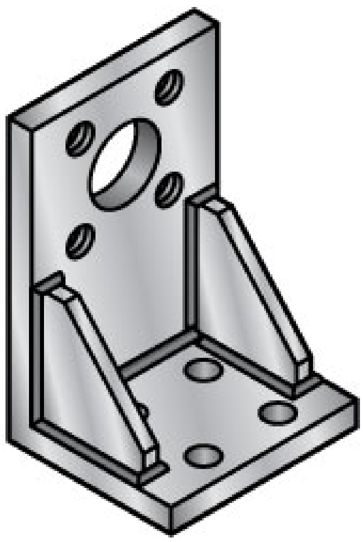

Figure 3.12: Fully customizable mounting bracket model from MISUMI [25]

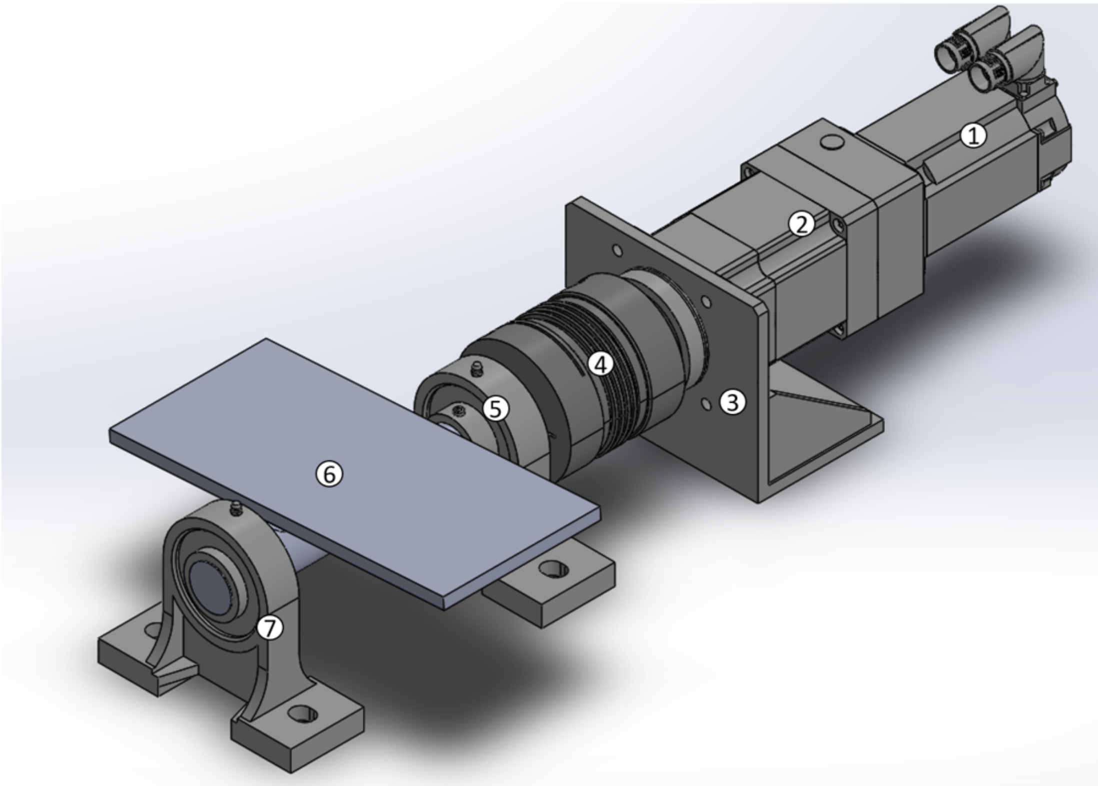

(a) Isometric view

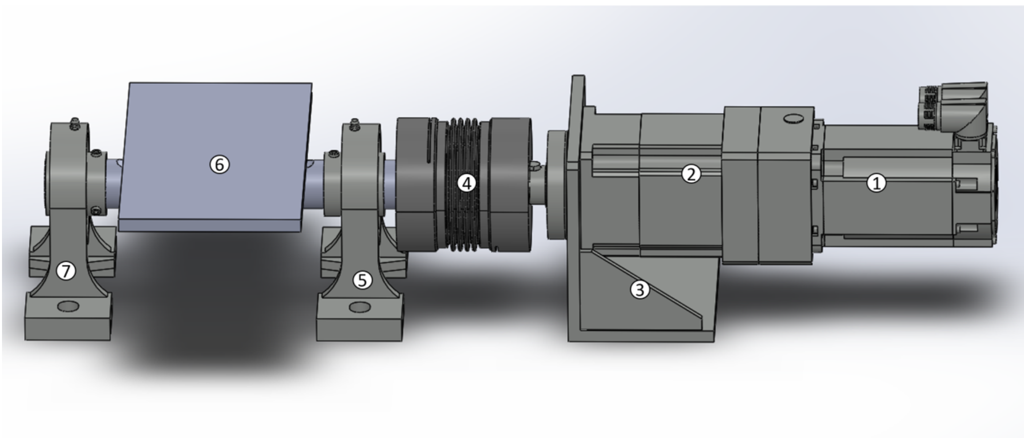

(b) Lateral view

Figure 3.13: 3D model of the complete rotation module: (1) motor, (2) gearhead, (3) mounting bracket, (4) coupling, (5) bearing, (6) shaft-platform assembly, (7) bearing.

3.2 Linear modules

To size our linear actuators, as explained in section 2.7.3, we will rely on the catalog from NTN-SNR Linear Motion [18]. During this sizing process, to describe the various characteristics of an actuator, we will employ the same coordinate system as provided in the catalog, as depicted in Figure 3.14. Indeed, among the key characteristics of a linear actuator, we find the maximum dynamic load moments for M_x, M_y, and M_z. We will rely on these characteristics multiple times, as they represent limits not to be exceeded to prevent a situation of buckling.

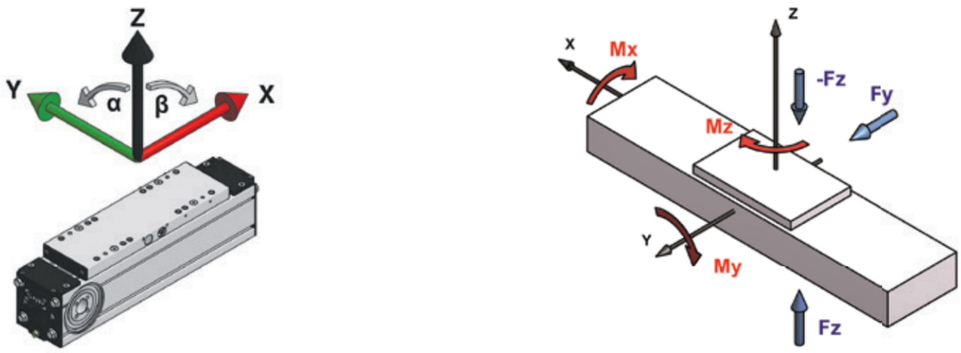

Figure 3.14: Coordinate system illustrating the forces and torques acting on a linear actuator in the principal directions. F_x represents the axial force, F_y the tangential load, and F_z the radial load. M_x denotes the torque in the roll direction, M_y the torque in the pitch direction, and M_z the torque in the yaw direction. Figure 2.1 from [18].

3.2.1 Selection of connection type

In the catalog, if we require 2 or 3-axis systems, there are various types of connections available depending on the configuration and arrangement of the different linear actuators. In our case, we need a 2-axis system with one horizontal linear actuator and another vertical one. For this configuration, there are three different types of connections between the two actuators : A-Standard connection, cross connection, angle connection. These three possibilities are illustrated in Figure 3.15. Thus, we first need to make a choice among these three connection types.

Depending on the connection type, various actuator models are feasible. For the A-Standard connection type, the vertical actuator is a toothed belt-Ω- drive from the AXC series. As illustrated in Figure E.1 in the Appendix E.1, this type of actuator exhibits lower dynamic torque resistance M_x in comparison to other available actuator types for the remaining two connection types. Consequently, we will exclude the A-Standard connection type due to this constraint.

Then, as the remaining two connection types employ the same actuator models, we need to rely on another criterion to differentiate between them. As depicted in Figure 3.15, various linear actuators feature a slider unit that moves along the actuator's structure when the latter remains fixed. However, in instances where the slider unit remains stationary (as in the case of a cross connection), the entire module's structure undergoes movement. Considering that slider units are significantly lighter than the overall module

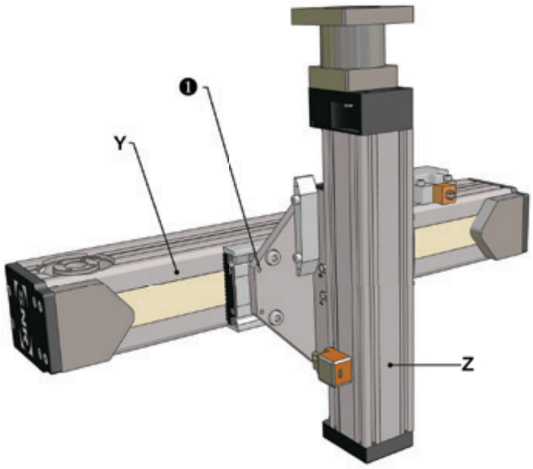

(a) Cross connection

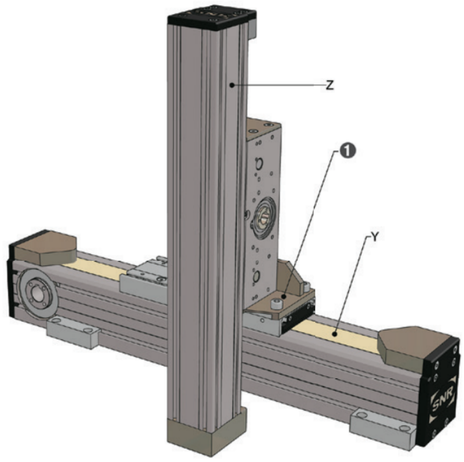

(b) A-Standard connection

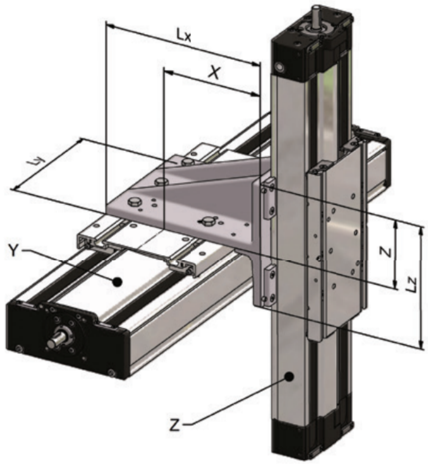

(c) Angle connection

Figure 3.15: Various types of connections possible for a 2-axis system with a horizontal linear actuator and a vertical one. Figures (a), (b), and (c) correspond to Figures 6.11, 6.17, and 6.21 from [18].

structures, it is more advisable to set the slider unit in motion rather than the entire structure. Based on this reasoning, we will hence choose the angle connection.

3.2.2 Model selection and sizing

For this connection type, the various possible configurations based on the utilized models can be observed in Figure E.7 in Appendix E.7. In all cases, the AXDL model is employed. For each model type, there are then various sizes available. For example, for the AXDL model, there are different sizes and performance levels such as AXDL110, AXDL160, and AXDL240. Furthermore, an AXDL model can be driven either by a lead screw (AXDL110S) or by a toothed belt (AXDL110Z). However, when comparing the two types of drives for the same model size, it is evident that in the case of belt drive, there are more limitations on the maximum dynamic load moments. This comparison can be observed by referring to tables in Figures E.2 and E.3 in Appendix E.2 and E.3. Therefore, we will opt for a lead screw drive. Regarding the guidance system, the AXDL models with screw drive utilize 2 parallel linear guides with ball chain technology [26]. This type of guidance can reach speeds of up to 5 m/s and accelerations of up to 50 m/s^2 [18]. By comparing these values to the velocity and acceleration characteristics established earlier for the two linear movements (see tables 2.3 and 2.4), we conclude that this suits our requirements perfectly. An illustration of the AXDL model with screw drive can be observed in Figure 3.16.

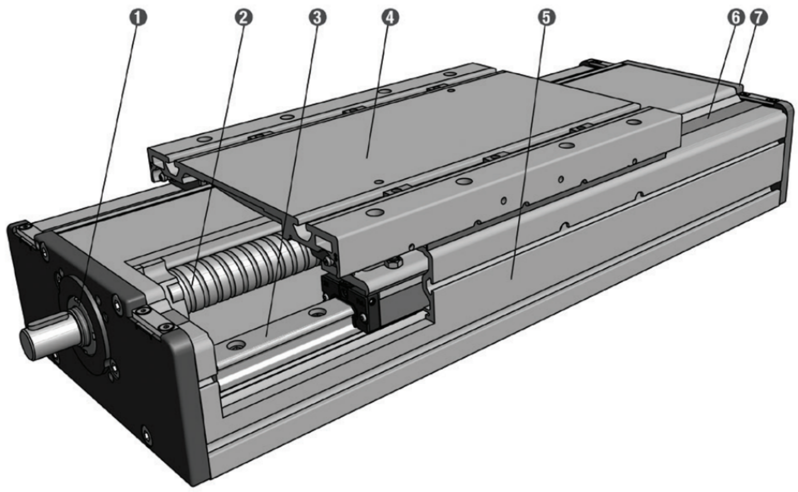

Figure 3.16: Structure of the AXDL linear axis with screw drive with : (1) fixed bearing unit, (2) screw drive, (3) guiding system, (4) slider unit, (5) profile, (6) Cover strip, (7) floating bearing unit. Figure 5.27 from [18].

Now, we must choose between the three different sizes: AXDL110S, AXDL160S, and AXDL240S. First, looking at the technical data of the AXDL110S model in Figure E.4, it can be seen that this type of model allows reaching speeds of up to 1.6 m/s. However, our vertical actuator needs to achieve speeds of up to 1.81 m/s, so we cannot use this size of model for this actuator. Additionally, examining the various possible configurations shown in Figure E.7, it becomes apparent that this size of model cannot be used for the horizontal actuator either. The AXDL160S model, on the other hand, allows for speeds of up to 2.5 m/s (see Figure E.5), making it potentially suitable for both of our actuators. However, we will need to ensure that we do not exceed the maximum dynamic load moments of the model. To do so, we must determine the forces and moments that our linear actuators will experience.

In order to determine these forces and moments, we need to consider the geometry of the setup. A 3D representation of the situation can be seen in Figure 3.17[1]. To determine the forces that the two sliders will experience, we first need to calculate the forces and moments at the prosthesis' rotation joint (point A). In Figure 3.181, it can be observed

[1]For this Figure, a coordinate system consistent with Figure 3.15c has been used.

that the prosthesis' joint will experience forces in the y and z directions, and a torque in the x direction. These forces and torque originate from the GRF transmitted to the joint through the prosthesis. For the forces, we will use equations 2.13 and 2.14 which allow us to decompose the GRF into principal directions (in the equation, F_x corresponds here to F_y). Across the 5 different walking cycles, we have a maximum force of 1800N in the F_z direction and +-1000N in the F_y direction. For the torque, considering dynamics, we can utilize the equation C.3 where T_3 represents the torque at the prosthesis' joint. Ultimately, across the 5 walking cycles, this results in a maximum torque M_x of -403 Nm.

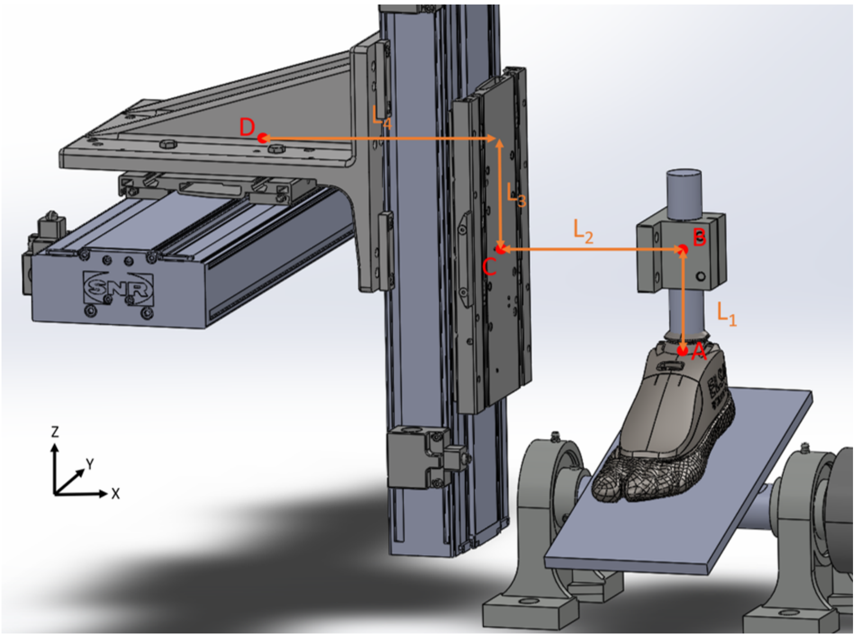

Figure 3.17: 3D representation of the geometric distances between the linear actuators and the prosthesis, with point A being the center of the prosthesis' rotation joint, point B the center of fixation, point C the center of the vertical linear actuator's slider, and point D the center of the horizontal linear actuator's slider.

Now, in order to establish the forces and moments at the center of the fixation (point B), we need to determine the length L_1. As depicted in Figure 3.18, the type of fixation used minimizes the distance L_1 in relation to the total length of the cylindrical pylon to which the prosthesis is attached. Therefore, we can here set the value of L_1 to 10cm. With this information, we can proceed to determine the forces and moments at point B [2] :

$$M_{B,X} = -M_{A,X} - L_1 F_{A,Y} = 403 - 0.1\ (-1000) = 503 \quad [Nm] \quad ^3 \tag{3.22}$$

$$F_{B,Y} = -F_{A,Y} = -1000 \quad [N] \tag{3.23}$$

$$F_{B,Z} = -F_{A,Z} = -1800 \quad [N] \tag{3.24}$$

[2]Here, we are considering the transmission of forces and moments between the different points using the third law of Newton.

[3]Here, to consider the worst-case scenario, we have considered a maximum negative force $F_{A,Y}$.

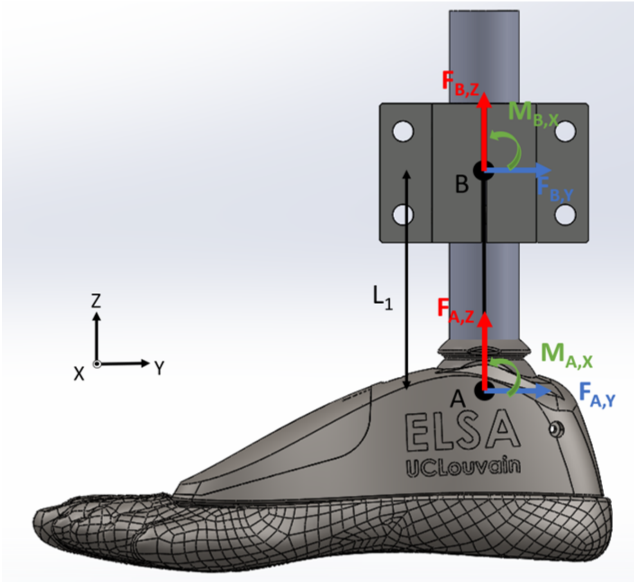

Figure 3.18: Representation of forces and moments acting in the principal directions on the center of the prosthesis' rotation joint at point A and on the center of fixation at point B.

Next, to determine the forces and moments at the center of the slider of the vertical linear actuator (point C), we need to determine the length L_2. Using the current 3D model of the test bench, we can determine an L_2 length of 17cm to ensure clearance from the rotation module and considering an additional margin. Following the same coordinate system as shown in Figure 3.18, we can thus determine the forces and moments acting on the slider at point C as follows 2:

$$M_{C,X} = -M_{B,X} = -503 \quad [Nm] \tag{3.25}$$

$$M_{C,Y} = L_2 F_{B,Z} = 0.17\,(-1800) = -306 \quad [Nm] \tag{3.26}$$

$$M_{C,Z} = -L_2 F_{B,Y} = -0.17\,(-1000) = 170 \quad [Nm] \tag{3.27}$$

$$F_{C,Y} = -F_{B,Y} = 1000 \quad [N] \tag{3.28}$$

$$F_{C,Z} = -F_{B,Z} = 1800 \quad [N] \tag{3.29}$$

Now, we need to compare the calculated moments of forces with the maximum dynamic load moments that the vertical linear actuator can withstand. For this actuator, based on the reference system of Figure 3.14, we have calculated maximum values for M_x, M_y, and M_z of 170 Nm, -306 Nm, and -503 Nm respectively. By comparing these values with the permissible maximum values from Figure E.3, we conclude that the AXDL160S model is sufficient for our vertical actuator.

To verify that this model also corresponds to the horizontal actuator, we will now need to calculate the moments of forces at point D. To do this, we need to determine the values of distances L_3 and L_4. For L_3, its value will vary during the usage cycle, so we will consider the worst-case scenario, which is when the vertical actuator's slider is in its highest or lowest position. As the variation in the position of this slider during a cycle is a maximum of 25 cm (see Table 2.4), we will consider a maximum length of 12.5 cm for L_3. For L_4, we need to take into account the distance X from Figure 3.15c as well as the thickness of the vertical actuator. For the distance X, a value of 144 mm can be found in the table of Figure E.7, and as the AXDL160S model has a thickness of 83 mm [18], we finally find a distance L_4 of 227 mm. We can now calculate the moments of forces at point D as follows :

$$M_{D,X} = -M_{C,X} - L_3 F_{C,Y} = 503 - 0.125\ (-1000) = 628\ \ [Nm] \tag{3.30}$$

$$M_{D,Y} = -M_{C,Y} + L_4 F_{C,Z} = 306 + 0.227\ (1800) = 714\ \ [Nm] \tag{3.31}$$

$$M_{D,Z} = -M_{C,Z} - L_4 F_{C,Y} = -170 - 0.227\ (-1000) = -397\ \ [Nm] \tag{3.32}$$

Now, we need to compare the calculated moments of forces with the maximum dynamic load moments that the horizontal linear actuator can withstand. For this actuator, based on the reference system of Figure 3.14, we have calculated maximum values for M_x, M_y, and M_z of 714 Nm, 628 Nm, and -397 Nm respectively. By comparing these values with the permissible maximum values from Figure E.3, we can see that our value of M_x is too high and we conclude that the AXDL160S model is not sufficient for our horizontal actuator. For this actuator, we will need to move to the AXDL240S model and verify that this model can be suitable for us. Since the size of the actuator has changed, we need to adjust the value of L_4 and recalculate our moments of forces. To determine the value of L_4, we will follow the same reasoning as before, adapting the value of X according to the table in Figure E.7. L_4 now has a value of 260 mm. By adapting this value into the equations for the moments of force at point D, we find :

$$M_{D,X} = -M_{C,X} - L_3 F_{C,Y} = 503 - 0.125\ (-1000) = 628\ \ [Nm] \tag{3.33}$$

$$M_{D,Y} = -M_{C,Y} + L_4 F_{C,Z} = 306 + 0.26\ (1800) = 774\ \ [Nm] \tag{3.34}$$

$$M_{D,Z} = -M_{C,Z} - L_4 F_{C,Y} = -170 - 0.26\ (-1000) = -430\ \ [Nm] \tag{3.35}$$

We can now compare these new values with those in the table of Figure E.3. Looking at this table, we can see that there are two different options for the AXDL240 model depending on the guidance system D or E. In both cases, it is the same guidance system as described earlier, the only difference lies in the length of the slider, where in case 'E' a longer slider length is used, allowing for greater forces to be accommodated. Here, with the newly calculated values, we can see that the AXDL240S model with guidance system D is a perfect fit for our requirements.

Ultimately, for the two linear actuators, horizontal and vertical, we will use the AXDL240S and AXDL160S models respectively. However, there are still different possible configurations for these two models as shown in Figures E.5 and E.6. In fact, to achieve the required speeds, two different configurations are possible for each model. In both cases, to make our choice, we will base it on the lead value of the screw. The lead value corresponds to the linear displacement of the slider for one revolution of the screw. Having a larger lead value allows for lower speed and acceleration values for our motors. However, a larger lead value also proportionally increases the required torque. Here, we will choose a larger lead value to prioritize lower accelerations since the actuators will need to move larger masses. Finally, the complete references of the two linear actuators are :

- AXDL160SNG 2550-D-300-600-0 0-01-00-X-0
- AXDL240SVG 3232-D-400-754-0 0-01-00-X-0

It should be noted that the last 5 digits correspond to the different possible additional options. Here, we have simply added the option with a mechanical switch (' 01 ' in the sequence) which will allow calibrating the position of the actuator at the start of operation. Additionally, the value X here corresponds to coupling options that depend on the type of motor used.

3.2.3 Motor selection

The next step is to select motors for our two linear actuators. We will start by selecting the motor for the vertical linear actuator as it will influence the selection of the other motor. To do this, we need to establish the required characteristics for the motor. We will begin by determining the maximum peak torque and the maximum RMS torque over the 5 different cycles that the motor will need to support. For a ball screw-driven system, the torque can be calculated as follows :

$$T = \frac{FP}{2\pi\eta} + aI_s \tag{3.36}$$

where F is the axial load in [N], P is the screw pitch in [m], η is the efficiency of the ball screw, a is the angular acceleration of the screw in [rad/s^2] and I_s is the inertia of the screw in [kgm^2]. Here, the axial load corresponds to the force F_2 in the dynamic equation C.2 in which we will use a mass m_2 of 4.2 kg [18] corresponding to the mass of the vertical linear actuator's slider. For P and η, you can find their values in the table of Figure E.5. For a, we already have the acceleration profiles of the linear movement in [m/s^2], and by multiplying this acceleration by $\frac{2\pi}{P}$, we get the acceleration profile of the screw in [rad/s^2]. For I_s, based on the table in Figure E.5 and considering a screw length equal to the stroke length (0.3m), we find a value of : $2,2510^{-4}0,3 = 0,67510^{-4}$ [kgm^2]. Regarding the velocity profiles, we already have the velocity profiles of the linear movement in [m/s], and by multiplying this velocity by $\frac{60}{P}$, we obtain the velocity profile of the screw in [revolutions per minute (RPM)]. With all these values, we can establish the motor characteristics for the 5 different walking cycles. These characteristics are summarized in Table 3.3.

Characteristics	Flat ground	Slope ascent	Slope descent	Stair ascent	Stair descent
Peak torque [Nm]	13.72	12.94	**14.92**	12	13.6
RMS torque [Nm]	**8.05**	7.47	7.37	7.6	7.27
Max speed [rpm]	1752	**2184**	1716	804	1500
Peak power [W]	1000	**1746**	1051	660	1513
RMS power [W]	390	**509**	273	224	407

Table 3.3: summary table of the characteristics of the vertical linear actuator motor over the 5 different gait cycles.

For their linear modules, NTN-SNR Linear Motion also provides the compatible gear head for the module based on the motor dimensions and the required reduction ratio. Here, we will simply need to choose a motor considering the desired reduction ratio that suits us best. Of course, we should select a slightly oversized motor to account for the gear head efficiency coefficient and the rotor's inertia.

First, we need to determine the type of motor we require. Based on the velocity and acceleration profiles established during the design phase, it's evident that the motor should exhibit high dynamic performance. An appropriate choice would have been to use a DC motor. However, the conducted research did not yield a sufficiently powerful DC motor for our application. Consequently, our choice shifted towards an AC synchronous motor as it is better suited for dynamic applications compared to asynchronous motors. Furthermore, we will refine our selection by focusing on permanent magnet motors, as they generally offer a high torque-inertia ratio, resulting in superior dynamic performance.

Subsequently, to identify motors that align with our specifications, we utilized the product configurator provided by Siemens [27], which facilitates the discovery of motors compatible with specified characteristics across a broad range of options. During this search, we factored in potential reduction ratios. Here, given motors capable of reaching up to 8000 rpm, we can consider potential reduction ratios of 3, 2, or 1 (no reduction) considering that the ball screw needs to operate up to 2184 rpm.

Considering an initial reduction ratio of 2, two motors potentially met our specifications. The reference for the first motor is: 1FT2206-2AH00-1MA0 [27]. The torque curve for this motor can be observed in Figure 3.19. In this plot, the two RMS torques at maximum speeds reached during their respective cycles for the two most demanding walking conditions (flat ground walking and slope ascent) are displayed. It can be seen that after accounting for the rotor inertia of the motor, the RMS torque at maximum speed during the slope ascent exceeds the continuous torque curve of the motor. Thus, this motor is not suitable for our application. The reference of the second motor is as follows: 1FT2206-4AH00-1MA0 [27]. The characteristic curve of this motor can be seen in Figure 3.20. For this motor, after taking into account the inertia of the motor rotor, we can see that the RMS torques are still within the continuous operating zone. However, this motor does not provide enough margin to consider the inertia of the reducer and its efficiency coefficient.

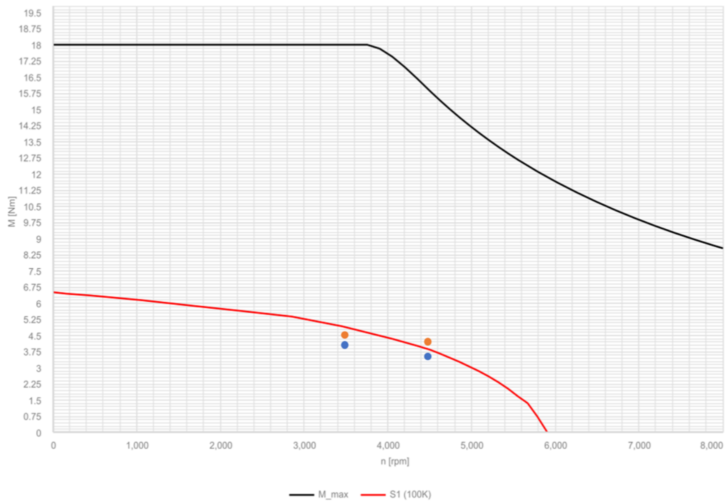

Figure 3.19: Characteristic curves of the motor 1FT2206-2AH00-1MA0 . The red curve represents the continuous operating region, while the black curve represents the intermittent operating region of the motor. The blue and orange points correspond to the RMS torques at maximum speeds reached during flat ground walking and slope ascent, before and after accounting for the rotor inertia of the motor, respectively. Figure generated using Siemens Product Configurator [27].

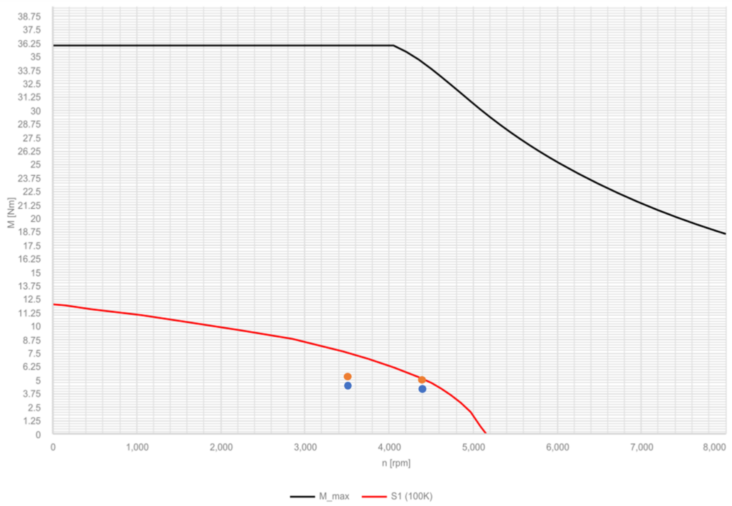

Figure 3.20: Characteristic curves of the motor 1FT2206-4AH00-1MA0 . The red curve represents the continuous operating region, while the black curve represents the intermittent operating region of the motor. The blue and orange points correspond to the RMS torques at maximum speeds reached during flat ground walking and slope ascent, before and after accounting for the rotor inertia of the motor, respectively. Figure generated using Siemens Product Configurator [27].

Next, considering not using a reducer this time, we find the following motor reference: 1FK2106-4AF00-1MA0. Not using a reducer would eliminate the need to account for the

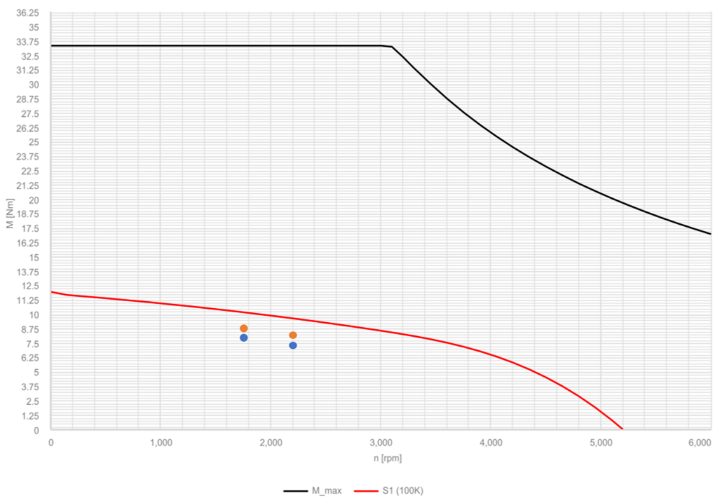

Figure 3.21: Characteristic curves of the motor 1FK2106-4AF00-1MA0 . The red curve represents the continuous operating region, while the black curve represents the intermittent operating region of the motor. The blue and orange points correspond to the RMS torques at maximum speeds reached during flat ground walking and slope ascent, before and after accounting for the rotor inertia of the motor, respectively. Figure generated using Siemens Product Configurator [27].

efficiency coefficient and inertia of the reducer. The characteristic curves of this motor can be seen in Figure 3.21. Here, we can observe that after taking into account the inertia of the motor rotor, the RMS torques still fall well within the continuous operating zone of the motor. We can also see that this motor can handle peak torques up to 33Nm, which is more than sufficient for our requirements. The motor datasheet can be found in Appendix D.4. Here, a version of the motor with an encoder system has been selected.

Now, we can move on to sizing the motor for the horizontal linear actuator. Firstly, for characterization, as it is also a ball screw drive, the equation 3.36 can be used to calculate the required torque. Here, the axial load corresponds to the force F_1 in the dynamic equation C.1 where we will use a mass m_2 of 22.9 kg corresponding to the total mass of the vertical actuator [18] including the motor (see Figure D.4, and a mass m_1 of 6.4 kg corresponding to the mass of the horizontal actuator's slider[18]. For P and η, their values can be found in the table of Figure E.6. For I_s, based on the data from the same table and considering a screw length equal to the travel length (0.4m), we find a value of : $6,1710^{-4}0,4 = 2,46810^{-4}$ [kgm$^{\mathbf{2}}$]. For the velocity and acceleration profiles, as before, we can use the screw pitch to determine their values in [rpm] and [rad/s$^{\mathbf{2}}$]. With all these values, we can establish the motor characteristics for the 5 different walking cycles. These characteristics are presented in Table 3.4.

Now that the characteristics have been established, we can proceed with motor selection. Once again, the motor we need should have high dynamic performance, so we will look into DC-type motors. For searching a motor compatible with our specifications, we will use the Kollmorgen catalog [20]. In this catalog, some motors offer speeds up to 8000

Characteristics	Flat ground	Slope ascent	Slope descent	Stair ascent	Stair descent
Peak torque [Nm]	3.09	3.32	3.37	3.84	**5.4**
RMS torque [Nm]	0.93	1.54	1.74	1.89	**3.31**
Max speed [rpm]	750	450	881.25	918.75	**2156.25**
Peak power [W]	170	106.2	155.5	202	**689**
RMS power [W]	36	31.77	72.14	47.8	**277.7**

Table 3.4: summary table of the characteristics of the horizontal linear actuator motor over the 5 different gait cycles.

rpm, and since the ball screw of the actuator should reach a maximum speed of 2157 rpm, we can consider a maximum reduction ratio of 3. Considering this ratio, the motor should have a nominal torque of 1.1 Nm and a peak torque of 1.8 Nm. The AKM2G-24PL 96 VDC motor could potentially be suitable. We can see the motor's characteristic curves in Figure 3.22.

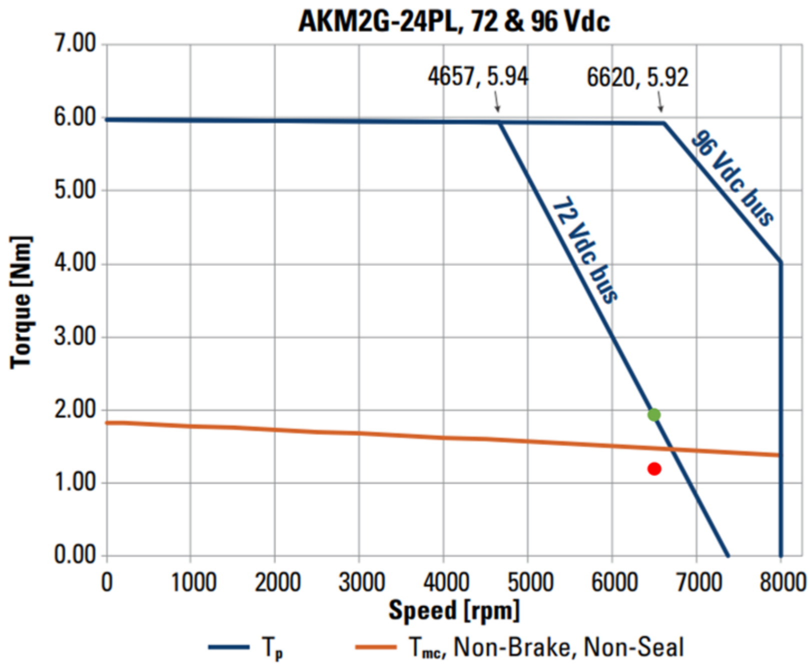

Figure 3.22: Characteristic curves of the AKM2G-24PL motor. The orange line represents the continuous available torque, while the blue line represents the peak torque. The red and blue points correspond respectively to the RMS and peak torque at maximum speed reached during stair descent considering the motor rotor inertia and a gear head efficiency of 0.95. Figure from [20] page 13.

Here, we have considered a reduction ratio of 3. For this type of ratio, reducers typically have a single stage of reduction, so we can assume that the reducer used will have an efficiency coefficient of 0.95. Taking into account this coefficient as well as the inertia of the motor's rotor, we can recalculate the required torque as follows :

$$T = \frac{1}{0.95}(\frac{FP}{2\pi\eta} + a(I_S + 3I_R)) \tag{3.37}$$

where F is the axial load in [N], P is the screw pitch in [m], η is the efficiency of the ball screw, a is the angular acceleration of the screw in [rad/s^2], I_s is the inertia of the screw in [kgm^2] and I_R is the motor rotor inertia in [kgm^2]. Using a value of $0,279\ 10^{-4}$ [kgm^2] for I_R [20], we find a maximum RMS torque of 3.58 Nm and a maximum peak torque of 5.97 Nm over the 5 different walking cycles. Taking into account the reduction ratio, the motor must therefore be able to provide a nominal torque of 1.19 Nm and a peak torque of 1.99 Nm. From Figure 3.22, we can therefore conclude that the motor is still sufficient and has some margin to account for the inertia of the reducer. Considering a version of the motor with an encoder system, the final reference for the motor is AKM2G-24PLANDN2-10.

3.3 Sensors

In order to fulfill its functions, the test bench will need to be equipped with several sensors. Firstly, as specified in chapter 2, the three different actuators need to be controlled in position during the swing phase. During the stance phase, the linear actuators will be controlled in force, while the rotational actuator will be controlled in position. To enable these control modes, various sensors will be required.

For position control, the three different motors are already equipped with encoder systems. It's sufficient to calibrate the initial position of the actuator at the beginning of usage to estimate the current position of the module using the encoders. For the linear actuators, both modules are already equipped with contact switch sensors to calibrate the initial position. For the rotational module, the simplest solution is to add a contact sensor so that the platform comes into contact with the sensor at certain angles. Any type of contact sensor can be suitable.

Next, for force control of the linear actuators, we need to be able to measure the forces applied by these actuators. Additionally, as indicated in the specifications, we also need to measure the torque at the prosthetic joint. The configuration of the forces and torque to be measured requires a 6-axis sensor. Assuming this sensor is placed between point B and point C in the Figure 3.17, the sensor should be capable of measuring forces up to 1800N and torque up to 500Nm. The K6D110 multi-component sensor from PM Instrumentation [28] could be suitable for our use. This sensor can measure forces up to 8kN and torques up to 750Nm. The mounting system for this sensor has not yet been determined. However, its placement within the test bench can be visualized in Figure 3.23.

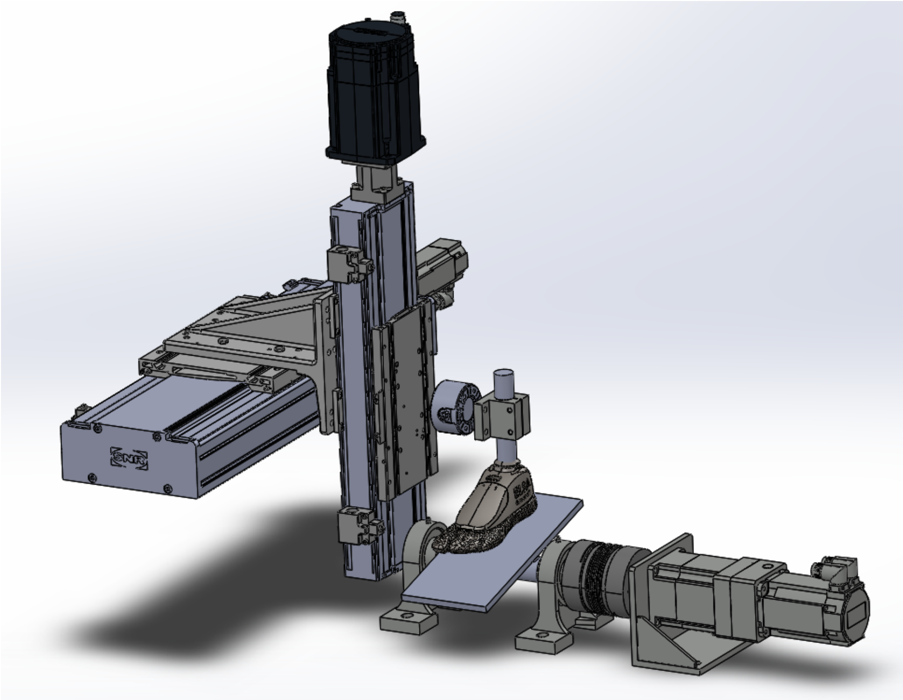

(a) First view

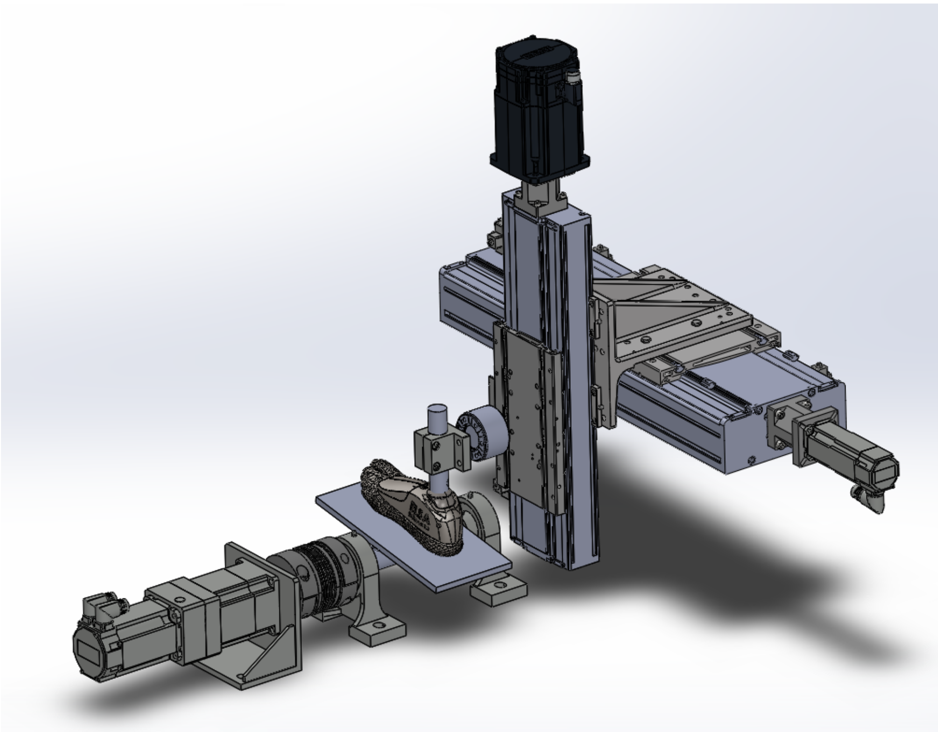

(b) Second view

Figure 3.23: 3D representation of the test bench

Chapter 4

Discussion and conclusion

This section aims to summarize results obtained from each step of the design process. By recapitulating the hypothesis used and mentioning further steps, we will be able to fully understand this thesis. Our approach involves a systematic review of each preceding segment, wherein we elucidate the core concepts and highlight key notions, thus enabling a holistic understanding.

4.1 Design

The purpose of this section was to devise an optimal design that addresses the constraints in the most efficient manner.

Firstly, we listed the main functions (MF), main constraints (MC), along with their corresponding requirements (FR and CR). This process aimed to establish clear specifications and provide a robust foundation for our work. Secondly, we undertook an analysis of the challenges posed by bipedal walking. Our focus was directed towards the dominant sagittal plane, where we identified key parameters (α, β, (x,y), GRF) to guide our investigation.

Subsequently, we explored several conceptual designs, weighing their advantages and disadvantages before ultimately selecting the most suitable option. In this chosen configuration, the prosthesis remains stationary while the substitute ground is set in motion. Within this context, we addressed two linear movements and one rotational movement, the order of which needed determination. Through a kinematic study, we arrived at the decision to employ q_1 and q_2 as prismatic joints, and q_3 as a revolute joint.

The establishment of three equations formed the dynamic model of our chosen solution. To characterize the distinct movements of each actuator, we assessed their range of velocity, acceleration, force, torque, and position. This analysis enabled the selection of the appropriate actuation and guidance systems.

As we progressed, we refined the design to accommodate newly encountered constraints. This iterative process culminated in a final conceptual design that comprehensively met all requirements.

4.2 Test bench sizing

After the design process, we needed to fully dimension the defined solutions. We first characterize each component to select the best fitting solution. Afterward, we ensured that each component was suitable by verifying that it met all the requirements. Here is a summary of the key dimensions of the components or their market references :

- Rotating shaft : aluminum alloy 2014-T6 with a minimum diameter of 36mm and a total length of 330mm.
- Platform : aluminum alloy 2014-T6, length of 320mm, width of 150mm, and thickness of 11mm.
- Gear motor assembly : motor AKM2G-42PLANC22-10 [20] and gear head VT010-040-0 RM100-40 [22].
- Coupling : BKL 300 32 PFN 40 1 [23].
- Bearing units : cast iron UCPH208 bearing housings [24].
- Mounting bracket : set of welded mounting plates completely customized according to the dimensions of the gear head [25].
- Vertical linear module and motor : AXDL160SNG 2550-D-300-600-0 0-01-00-X-0 [18] and 1FK2106-4AF00-1MA0 [27].
- Horizontal linear module : AXDL240SVG 3232-D-400-754-0 0-01-00-X-0 [18] and AKM2G-24PLANDN2-10 [20].

Consequently, the system is now fully designed and dimensioned, paving the way for the manufacturing of a prototype.

4.3 Improvements

Due to time constraints, our work had to conclude at its current stage. However, there are several future steps that can be undertaken to ultimately achieve a functional testbench. First of all, regarding mechanical assembly, we need to find a way to connect the cylindrical pylon to the vertical actuator slider while accommodating the 6-axis sensor. We also need to devise a mechanical structure for attaching the horizontal actuator.

Furthermore, the entire electronic framework of the test bench needs to be designed. This encompasses the cables, drivers, and power sources for all three motors. Lastly, it will also be essential to implement safety systems such as an emergency stop button and a protective enclosure.

4.4 Conclusion

In conclusion, the primary objective of designing and dimensioning a testbench for an ankle device has been successfully achieved. A comprehensive 3D CAD model has been developed, complete with product references. The design selection process carefully considered various parameters to address constraints effectively. Furthermore, the sizing process was meticulously conducted, employing a comprehensive methodology to encompass a wide range of potential scenarios.

Bibliography

[1] Wilken J. Russell Esposito E, Rábago CA. *The influence of traumatic transfemoral amputation on metabolic cost across walking speeds.* Prosthet Orthot Int. 42(2):214-222., 2018 Apr.

[2] Lakra A. Adams CT. Below-knee amputation. `https://www.ncbi.nlm.nih.gov/books/NBK534773/`. [Updated 2023 May 7]. In: StatPearls [Internet]. Treasure Island (FL): StatPearls Publishing; 2023 Jan-.

[3] Chauvin BJ. Myers M. Above-knee amputation. `https://www.ncbi.nlm.nih.gov/books/NBK544350/`. [Updated 2022 Jun 21]. In: StatPearls [Internet]. Treasure Island (FL): StatPearls Publishing; 2023 Jan-.

[4] Xu H. Huang Q, Li B. *The Design and Testing of a PEA Powered Ankle Prosthesis Driven by EHA.* Biomimetics (Basel). 12;7(4):234., 2022 Dec.

[5] Nicola Petrone, Gianfabio Costa, Gianmario Foscan, Francesco Bettella, Gianluca Migliore, and Andrea Giovanni Cutti. Conceptual design of a new multi-component test bench for the dynamic characterization of running specific prostheses. *Proceedings*, 49(1), 2020.

[6] ISO 22675 : 2016. Prosthetics — testing of ankle-foot devices and foot units — requirements and test methods. `https://www.iso.org/obp/ui/en/#iso:std:iso:22675:ed-2:v1:en`. June-2021.

[7] Thelkin. Testing systems for foot and ankle prosthesis. `https://thelkin.com/en/products-en-2/special-systems-en/foot-ankle-tester-en.html`. June-2021.

[8] Shore Western. Ankle-foot prosthesis simulator.. `http://shorewestern.com/Documents/PDFs/Ankle.pdf`.

[9] Katzenshlager R. Pirker W. Gait disorders in adults and the elderly. *Wien Klin Wochenschr; 129 : 81-95*, 2017.

[10] Seth Hutchinson Mark W. Spong and M. Vidyasagar. *Robot Modeling and Control.* JOHN WILEY SONS, INC., First Edition.

[11] T. Yoshikawa. Manipulability of robotic mechanisms. *International Journal of Robotics Research, 4(2):3–9*, 1985.

[12] D. A. Winter. *Biomechanics and Motor Control of Human Movement.* John Wiley Sons, Oct. 2009.

[13] B J McFadyen and D A Winter. An integrated biomechanical analysis of normal stair ascent and descent. *Journal of biomechanics vol. 21,9 : 733-44*, 1988.

[14] Neuman R Bolívar-Nieto E Fey NP Gregg RD. Reznick E, Embry KR. Lower-limb kinematics and kinetics during continuously varying human locomotion. *Scientific data;8(1):282.*, 2021 Oct 28.

[15] Mazzoleni P Ferrarin M. Bovi G, Rabuffetti M. A multiple-task gait analysis approach: kinematic, kinetic and emg reference data for healthy young and adult subjects. *Gait Posture. 33(1):6-13.*, 2011.

[16] Daron A et al. Poleur M, Ulinici A. Normative data on spontaneous stride velocity, stride length, and walking activity in a non-controlled environment. *Orphanet J Rare Dis. 2021;16(1):318.*, Published 2021 Jul 19.

[17] Noboru Sekiya, Hiroshi Nagasaki, Hajime Ito, and Taketo Furuna. Optimal walking in terms of variability in step length. *Journal of Orthopaedic & Sports Physical Therapy*, 26(5):266–272, 1997.

[18] NTN-SNR. Ntn-snr linear motion : Linear axis. `https://www.ntn-snr.com/sites/default/files/2021-02/DOC.I_AX_CAT2_GBa_web2.pdf`.

[19] K.M. Marshek R.C. Juvinall. *The Fundamentals of Machine Component Design*. éd. J. Wiley and Sons, 2020.

[20] Kollmorgen. Akm2g low voltage servo motor selection guide. `https://www.kollmorgen.com/sites/default/files/AKM2G3-LV-KM_SG_000360_RevB-EN.pdf`, 2020.

[21] Micron. Gearhead selection tool. `https://www.micronmotioneering.com/GearheadSelection/ConfigurationPage`.

[22] Thomson Linear Motion Optimized. True planetary gearheads catalog. `https://www.thomsonlinear.com/downloads/gearheads/TRUE_Planetary_Gearheads_cten.pdf#page=82e`.

[23] R+W. Precision couplings. `https://www.rw-france.fr/produits/accouplements-de-precision/accouplements-a-soufflet-metallique/bkl/`.

[24] MISUMI. Cast iron pillow unit ucph. `https://uk.misumi-ec.com/vona2/detail/221000346064/?CategorySpec=00000005554%3a%3aa%0900000005555%3a%3aa%0900000005563%3a%3amig00000001998150%0900000005559%3a%3ab%0900000005556%3a%3ac&CAD=01&rid=cat_`.

[25] MISUMI. L-shaped brackets. `https://uk.misumi-ec.com/vona2/mech/M1500000000/M1505000000/M1505020000/#`.

[26] NTN-SNR. Ntn-snr linear motion : Linear guides. https://www.ntn-snr.com/sites/default/files/2018-09/doc.i_lg_cat2_gba_web.pdf.

[27] Siemens. Product configurator. https://mall.industry.siemens.com/spice/cloudcm/configurator.

[28] PM Instrumentation. K6d110 multi-component sensor. https://www.pm-instrumentation.com/k6d110-capteur-de-force-6-composantes-1kn100nm-a-10-kn750-nm.

Appendices

Appendix A

Direct kinematic models and Jacobian matrices

To perform the direct (or Forward) kinematic model of the various configurations, the approach outlined in Section 3.2 of [10] will be followed, utilizing the Denavit-Hartenberg convention. For obtaining the distinct Jacobian matrices, the methodology described in Section 4.6 of [10] was adopted. In the geometric models of the seven distinct configurations (Figure A.1 to A.7) , the variable a(t) can also be noted. This variable denotes the variable position of the contact point between the prosthesis and the bench (it can thus assume negative values).

It is also worth noting that, to simplify the mathematical notation, specific notations have been employed:

- $S_i = sin(q_i^*)$
- $C_i = sin(q_i^*)$
- $S_{ij} = sin(q_i^* + q_j^*)$
- $C_{ij} = cos(q_i^* + q_j^*)$
- $S_{ijk} = sin(q_i^* + q_j^* + q_k^*)$
- $C_{ijk} = cos(q_i^* + q_j^* + q_k^*)$

$\forall i, j, k \in \{1, 2, 3\}$.

A.1 Prismatic-Prismatic-Revolute Joints Manipulator

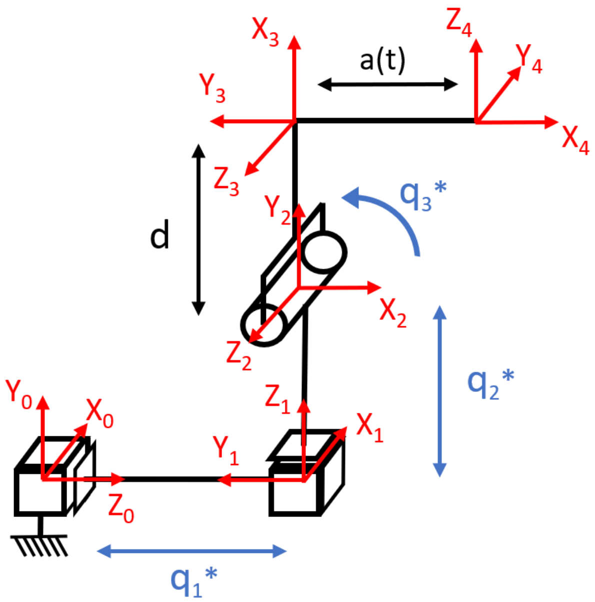

Figure A.1: Geometric model

Link	d_i	a_i	α_i	θ_i
1	q_1^*	0	-90	0
2	q_2^*	0	90	-90
3	0	d	0	q_3^*
4	0	a(t)	-90	-90

Table A.1: Link parameters

$$^0H_1 = \begin{bmatrix} 1 & 0 & 0 & 0 \\ 0 & 0 & 1 & 0 \\ 0 & -1 & 0 & q_1^* \\ 0 & 0 & 0 & 1 \end{bmatrix} \qquad ^1H_2 = \begin{bmatrix} 0 & 0 & -1 & 0 \\ -1 & 0 & 0 & 0 \\ 0 & 1 & 0 & q_2^* \\ 0 & 0 & 0 & 1 \end{bmatrix} \qquad ^2H_3 = \begin{bmatrix} C_3 & -S_3 & 0 & dC_3 \\ S_3 & C_3 & 0 & dS_3 \\ 0 & 0 & 1 & 0 \\ 0 & 0 & 0 & 1 \end{bmatrix}$$

$$^3H_4 = \begin{bmatrix} 0 & 0 & 1 & 0 \\ -1 & 0 & 0 & -a(t) \\ 0 & -1 & 0 & 0 \\ 0 & 0 & 0 & 1 \end{bmatrix} \qquad ^0H_2 = \begin{bmatrix} 0 & 0 & -1 & 0 \\ 0 & 1 & 0 & q_2^* \\ 1 & 0 & 0 & q_1^* \\ 0 & 0 & 0 & 1 \end{bmatrix} \qquad ^0H_3 = \begin{bmatrix} 0 & 0 & -1 & 0 \\ S_3 & C_3 & 0 & dS_3 + q_2^* \\ C_3 & -S_3 & 0 & dC_3 + q_1^* \\ 0 & 0 & 0 & 1 \end{bmatrix}$$

$$^0H_4 = \begin{bmatrix} 0 & 1 & 0 & 0 \\ -C_3 & 0 & S_3 & q_2^* + dS_3 - a(t)C_3 \\ S_3 & 0 & C_3 & q_1^* + dC_3 + a(t)S_3 \\ 0 & 0 & 0 & 1 \end{bmatrix} \qquad J(q) = \begin{bmatrix} 0 & 0 & 0 \\ 0 & 1 & dC_3 + a(t)S_3 \\ 1 & 0 & a(t)C_3 - dS_3 \\ 0 & 0 & -1 \\ 0 & 0 & 0 \\ 0 & 0 & 0 \end{bmatrix}$$

$$det\ J = \begin{vmatrix} 0 & 1 & dC_3 + a(t)S_3 \\ 1 & 0 & a(t)C_3 - dS_3 \\ 0 & 0 & -1 \end{vmatrix} = 1$$

A.2 Prismatic-Revolute-Prismatic Joints Manipulator

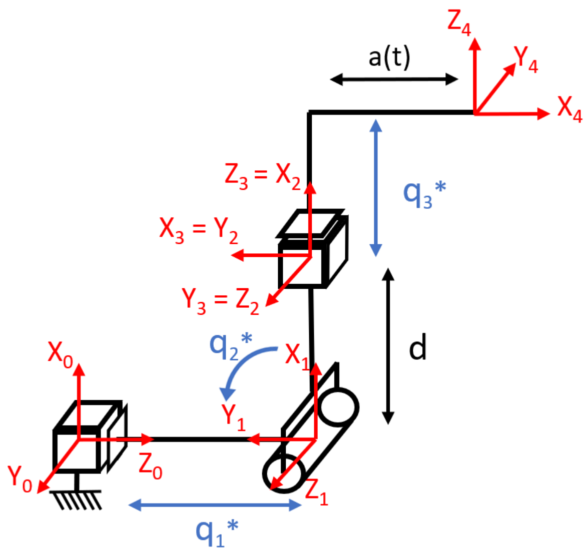

Figure A.2: Geometric model

Link	d_i	a_i	α_i	θ_i
1	q_1^*	0	-90	0
2	0	d	0	q_2^*
3	0	0	90	90
4	q_3^*	a(t)	0	180

Table A.2: Link parameters

$$^0H_1 = \begin{bmatrix} 1 & 0 & 0 & 0 \\ 0 & 0 & 1 & 0 \\ 0 & -1 & 0 & q_1^* \\ 0 & 0 & 0 & 1 \end{bmatrix} \quad ^1H_2 = \begin{bmatrix} C_2 & -S_2 & 0 & dC_2 \\ S_2 & C_2 & 0 & dS_2 \\ 0 & 0 & 1 & 0 \\ 0 & 0 & 0 & 1 \end{bmatrix} \quad ^2H_3 = \begin{bmatrix} 0 & 0 & 1 & 0 \\ 1 & 0 & 0 & 0 \\ 0 & 1 & 0 & 0 \\ 0 & 0 & 0 & 1 \end{bmatrix}$$

$$^3H_4 = \begin{bmatrix} -1 & 0 & 0 & -a(t) \\ 0 & -1 & 0 & 0 \\ 0 & 0 & 1 & q_3^* \\ 0 & 0 & 0 & 1 \end{bmatrix} \quad ^0H_2 = \begin{bmatrix} C_2 & -S_2 & 0 & dC_2 \\ 0 & 0 & 1 & 0 \\ -S_2 & -C_2 & 0 & q_1^* - dS_2 \\ 0 & 0 & 0 & 1 \end{bmatrix}$$

$$^0H_3 = \begin{bmatrix} -S_2 & 0 & C_2 & dC_2 \\ 0 & 1 & 0 & 0 \\ -C_2 & 0 & -S_2 & q_1^* - dS_2 \\ 0 & 0 & 0 & 1 \end{bmatrix} \quad ^0H_4 = \begin{bmatrix} S_2 & 0 & C_2 & a(t)S_2 + q_3^*C_2 + dC_2 \\ 0 & -1 & 0 & 0 \\ C_2 & 0 & -S_2 & a(t)C_2 - q_3^*S_2 + q_1^* - dS_2 \\ 0 & 0 & 0 & 1 \end{bmatrix}$$

$$J(q) = \begin{bmatrix} 0 & a(t)C_2 - S_2(q_3^* + d) & C_2 \\ 0 & 0 & 0 \\ 1 & -a(t)S_2 - C_2(q_3^* + d) & -S_2 \\ 0 & 0 & 0 \\ 0 & 1 & 0 \\ 0 & 0 & 0 \end{bmatrix} \; det\ J = \begin{vmatrix} 0 & a(t)C_2 - S_2(q_3^* + d) & C_2 \\ 1 & -a(t)S_2 - C_2(q_3^* + d) & -S_2 \\ 0 & 1 & 0 \end{vmatrix} = -cos(q_2^*)$$

A.3 Revolute-Prismatic-Prismatic Joints Manipulator

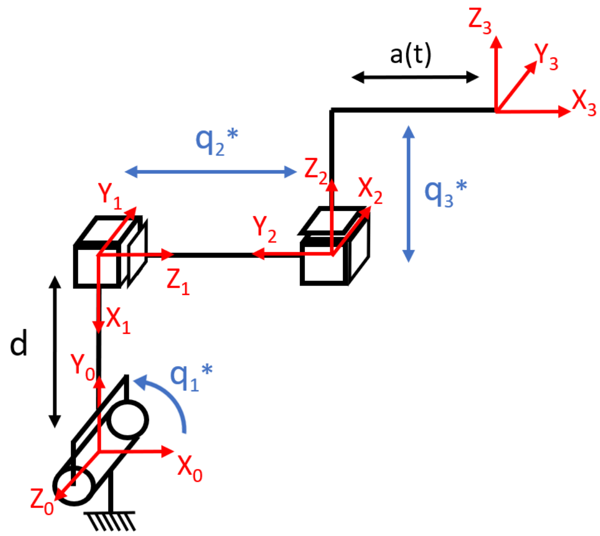

Figure A.3: Geometric model

Link	d_i	a_i	α_i	θ_i
1	0	d	-90	180 + q_1^*
2	q_2^*	0	-90	90
3	q_3^*	a(t)	0	-90

Table A.3: Link parameters

$$^{0}H_1 = \begin{bmatrix} -C_1 & 0 & S_1 & -dC_1 \\ -S_1 & 0 & -C_1 & -dS_1 \\ 0 & -1 & 0 & 0 \\ 0 & 0 & 0 & 1 \end{bmatrix} \quad ^{1}H_2 = \begin{bmatrix} 0 & 0 & -1 & 0 \\ 1 & 0 & 0 & 0 \\ 0 & -1 & 0 & q_2^* \\ 0 & 0 & 0 & 1 \end{bmatrix} \quad ^{2}H_3 = \begin{bmatrix} 0 & 1 & 0 & 0 \\ -1 & 0 & 0 & -a(t) \\ 0 & 0 & 1 & q_3^* \\ 0 & 0 & 0 & 1 \end{bmatrix}$$

$$^{0}H_2 = \begin{bmatrix} 0 & -S_1 & C_1 & S_1q_2^* - dC_1 \\ 0 & C_1 & S_1 & -C_1q_2^* - dS_1 \\ -1 & 0 & 0 & 0 \\ 0 & 0 & 0 & 1 \end{bmatrix} \quad ^{0}H_3 = \begin{bmatrix} S_1 & 0 & C_1 & a(t)S_1 + C_1q_3^* + S_1q_2^* - dC_1 \\ -C_1 & 0 & S_1 & -a(t)C_1 - S_1q_3^* - C_1q_2^* - dS_1 \\ 0 & -1 & 0 & 0 \\ 0 & 0 & 0 & 1 \end{bmatrix}$$

$$J(q) = \begin{bmatrix} C_1(a(t) + q_2^*) + S_1(d - q_3^*) & S_1 & C_1 \\ S_1(a(t) + q_2^*) + C_1(q_3^* - d) & -C_1 & S_1 \\ 0 & 0 & 0 \\ 0 & 0 & 0 \\ 0 & 0 & 0 \\ 1 & 0 & 0 \end{bmatrix}$$

$$det\ J = \begin{vmatrix} C_1(a(t) + q_2^*) + S_1(d - q_3^*) & S_1 & C_1 \\ S_1(a(t) + q_2^*) + C_1(q_3^* - d) & -C_1 & S_1 \\ 1 & 0 & 0 \end{vmatrix} = sin^2(q_1^*) + cos^2(q_1^*) = 1$$

A.4 Prismatic-Revolute-Revolute Joints Manipulator

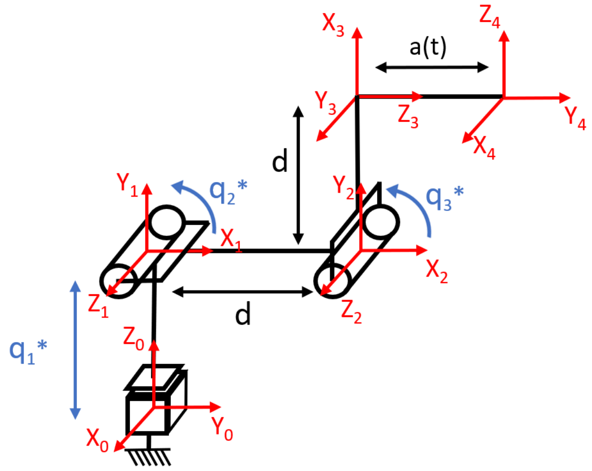

Figure A.4: Geometric model

Link	d_i	a_i	α_i	θ_i
1	q_1^*	0	90	90
2	0	d	0	q_2^*
3	0	d	90	q_3^*
4	a(t)	0	90	90

Table A.4: Link parameters

$$
{}^0H_1 = \begin{bmatrix} 0 & 0 & 1 & 0 \\ 1 & 0 & 0 & 0 \\ 0 & 1 & 0 & q_1^* \\ 0 & 0 & 0 & 1 \end{bmatrix} \qquad
{}^1H_2 = \begin{bmatrix} C_2 & -S_2 & 0 & dC_2 \\ S_2 & C_2 & 0 & dS_2 \\ 0 & 0 & 1 & 0 \\ 0 & 0 & 0 & 1 \end{bmatrix} \qquad
{}^2H_3 = \begin{bmatrix} C_3 & 0 & S_3 & dC_3 \\ S_3 & 0 & -C_3 & dS_3 \\ 0 & 1 & 0 & 0 \\ 0 & 0 & 0 & 1 \end{bmatrix}
$$

$$
{}^3H_4 = \begin{bmatrix} 0 & 0 & 1 & 0 \\ 1 & 0 & 0 & 0 \\ 0 & 1 & 0 & a(t) \\ 0 & 0 & 0 & 1 \end{bmatrix} \quad
{}^0H_2 = \begin{bmatrix} 0 & 0 & 1 & 0 \\ C_2 & -S_2 & 0 & dC_2 \\ S_2 & C_2 & 0 & dS_2 + q_1^* \\ 0 & 0 & 0 & 1 \end{bmatrix} \quad
{}^0H_3 = \begin{bmatrix} 0 & 1 & 0 & 0 \\ C_{23} & 0 & S_{23} & dC_{23} + dC_2 \\ S_{23} & 0 & -C_{23} & dS_{23} + dS_2 + q_1^* \\ 0 & 0 & 0 & 1 \end{bmatrix}
$$

$$
{}^0H_4 = \begin{bmatrix} 1 & 0 & 0 & 0 \\ 0 & S_{23} & C_{23} & a(t)S_{23} + dC_{23} + dC_2 \\ 0 & -C_{23} & S_{23} & q_1^* + dS_{23} + dS_2 - a(t)C_{23} \\ 0 & 0 & 0 & 1 \end{bmatrix}
$$

$$
J(q) = \begin{bmatrix} 0 & a(t)C_{23} + d(S_{23} + S_2) & a(t)C_{23} + dS_{23} \\ 0 & 0 & 0 \\ 1 & a(t)S_{23} + d(C_{23} + C_2) & a(t)S_{23} + dC_{23} \\ 0 & 1 & 1 \\ 0 & 0 & 0 \\ 0 & 0 & 0 \end{bmatrix}
$$

$$
det\ J = \begin{vmatrix} 0 & a(t)C_{23} + d(S_{23} + S_2) & a(t)C_{23} + dS_{23} \\ 1 & a(t)S_{23} + d(C_{23} + C_2) & a(t)S_{23} + dC_{23} \\ 0 & 1 & 1 \end{vmatrix}
$$

$$
= (a(t)C_{23} + dS_{23}) + (-a(t)C_{23} - d(S_{23} + S_2) = -dsin(q_2^*)
$$

A.5 Revolute-Revolute-Prismatic Joints Manipulator

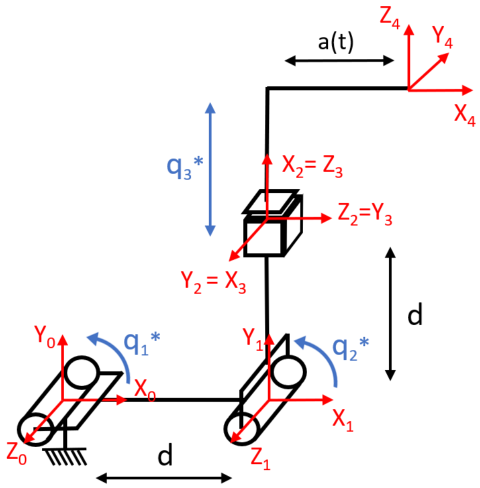

Figure A.5: Geometric model

Link	d_i	a_i	α_i	θ_i
1	0	d	0	q_1^*
2	0	d	90	q_2^*
3	0	0	90	90
4	q_3^*	a(t)	0	90

Table A.5: Link parameters

$$^0H_1 = \begin{bmatrix} C_1 & -S_1 & 0 & dC_1 \\ S_1 & C_1 & 0 & dS_1 \\ 0 & 0 & 1 & 0 \\ 0 & 0 & 0 & 1 \end{bmatrix} \quad {}^1H_2 = \begin{bmatrix} C_2 & 0 & S_2 & dC_2 \\ S_2 & 0 & -C_2 & dS_2 \\ 0 & 1 & 0 & 0 \\ 0 & 0 & 0 & 1 \end{bmatrix} \quad {}^2H_3 = \begin{bmatrix} 0 & 0 & 1 & 0 \\ 1 & 0 & 0 & 0 \\ 0 & 1 & 0 & 0 \\ 0 & 0 & 0 & 1 \end{bmatrix}$$

$$^3H_4 = \begin{bmatrix} 0 & -1 & 0 & 0 \\ 1 & 0 & 0 & a(t) \\ 0 & 0 & 1 & q_3^* \\ 0 & 0 & 0 & 1 \end{bmatrix} {}^0H_2 = \begin{bmatrix} C_{12} & 0 & S_{12} & d(C_{12}+C_1) \\ S_{12} & 0 & -C_{12} & d(S_{12}+S_1) \\ 0 & 1 & 0 & 0 \\ 0 & 0 & 0 & 1 \end{bmatrix} {}^0H_3 = \begin{bmatrix} 0 & S_{12} & C_{12} & d(C_{12}+C_1) \\ 0 & -C_{12} & S_{12} & d(S_{12}+S_1) \\ 1 & 0 & 0 & 0 \\ 0 & 0 & 0 & 1 \end{bmatrix}$$

$$^0H_4 = \begin{bmatrix} S_{12} & 0 & C_{12} & a(t)S_{12} + (q_3^*+d)C_{12} + dC_1 \\ -C_{12} & 0 & S_{12} & -a(t)C_{12} + (q_3^*+d)S_{12} + dS_1 \\ 0 & -1 & 0 & 0 \\ 0 & 0 & 0 & 1 \end{bmatrix}$$

$$J(q) = \begin{bmatrix} a(t)C_{12} - (q_3^*+d)S_{12} - dS_1 & a(t)C_{12} - (q_3^*+d)S_{12} & C_{12} \\ a(t)S_{12} + (q_3^*+d)C_{12} + dC_1 & a(t)S_{12} + (q_3^*+d)C_{12} & S_{12} \\ 0 & 0 & 0 \\ 0 & 0 & 0 \\ 0 & 0 & 0 \\ 1 & 1 & 0 \end{bmatrix}$$

$$det\ J = \begin{vmatrix} a(t)C_{12} - (q_3^*+d)S_{12} - dS_1 & a(t)C_{12} - (q_3^*+d)S_{12} & C_{12} \\ a(t)S_{12} + (q_3^*+d)C_{12} + dC_1 & a(t)S_{12} + (q_3^*+d)C_{12} & S_{12} \\ 1 & 1 & 0 \end{vmatrix}$$

$$= dS_1S_{12} + dC_1C_{12} = dcos(q_2^*)$$

A.6 Revolute-Prismatic-Revolute Joints Manipulator

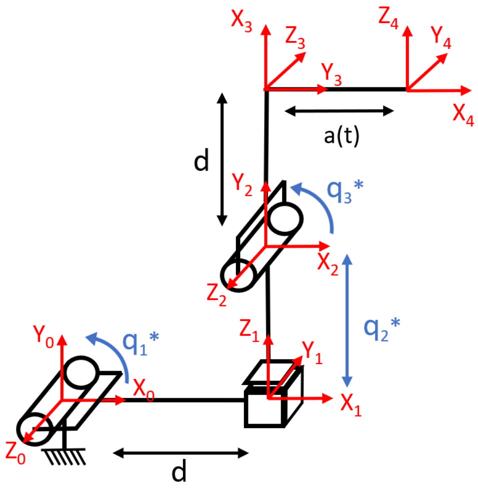

Figure A.6: Geometric model

Link	d_i	a_i	α_i	θ_i
1	0	d	-90	q_1^*
2	q_2^*	0	90	0
3	0	d	180	q_3^*
4	0	a(t)	90	90

Table A.6: Link parameters

$$ {}^0H_1 = \begin{bmatrix} C_1 & 0 & -S_1 & dC_1 \\ S_1 & 0 & C_1 & dS_1 \\ 0 & -1 & 0 & 0 \\ 0 & 0 & 0 & 1 \end{bmatrix} \quad {}^1H_2 = \begin{bmatrix} 1 & 0 & 0 & 0 \\ 0 & 0 & -1 & 0 \\ 0 & 1 & 0 & q_2^* \\ 0 & 0 & 0 & 1 \end{bmatrix} \quad {}^2H_3 = \begin{bmatrix} C_3 & S_3 & 0 & dC_3 \\ S_3 & -C_3 & 0 & dS_3 \\ 0 & 0 & -1 & 0 \\ 0 & 0 & 0 & 1 \end{bmatrix} $$

$$ {}^3H_4 = \begin{bmatrix} 0 & 0 & 1 & 0 \\ 1 & 0 & 0 & a(t) \\ 0 & 1 & 0 & 0 \\ 0 & 0 & 0 & 1 \end{bmatrix} \quad {}^0H_2 = \begin{bmatrix} C_1 & -S_1 & 0 & dC_1 - S_1q_2^* \\ S_1 & C_1 & 0 & dS_1 + C_1q_2^* \\ 0 & 0 & 1 & 0 \\ 0 & 0 & 0 & 1 \end{bmatrix} $$

$$ {}^0H_3 = \begin{bmatrix} C_{13} & S_{13} & 0 & d(C_{13} + C_1) - S_1q_2^* \\ S_{13} & -C_{13} & 0 & d(S_{13} + C_1) + C_1q_2^* \\ 0 & 0 & -1 & 0 \\ 0 & 0 & 0 & 1 \end{bmatrix} {}^0H_4 = \begin{bmatrix} S_{13} & 0 & C_{13} & a(t)S_{13} + d(C_{13} + C_1) - S_1q_2^* \\ -C_{13} & 0 & S_{13} & C_1q_2^* - a(t)C_{13} + d(S_{13} + S_1) \\ 0 & -1 & 0 & 0 \\ 0 & 0 & 0 & 1 \end{bmatrix} $$

$$ J(q) = \begin{bmatrix} a(t)C_{13} - d(S_{13} + S_1) - C_1q_2^* & -S_1 & a(t)C_{13} - dS_{13} \\ a(t)S_{13} + d(C_{13} + C_1) - S_1q_2^* & C_1 & a(t)S_{13} + dC_{13} \\ 0 & 0 & 0 \\ 0 & 0 & 0 \\ 0 & 0 & 0 \\ 1 & 0 & 1 \end{bmatrix} $$

$$ det\ J = \begin{vmatrix} a(t)C_{13} - d(S_{13} + S_1) - C_1q_2^* & -S_1 & a(t)C_{13} - dS_{13} \\ a(t)S_{13} + d(C_{13} + C_1) - S_1q_2^* & C_1 & a(t)S_{13} + dC_{13} \\ 1 & 0 & 1 \end{vmatrix} $$

$$ = -cos^2(q_2^*) - sin^2(q_2^*) = -q_2^* $$

A.7 Revolute-Revolute-Revolute Joints Manipulator

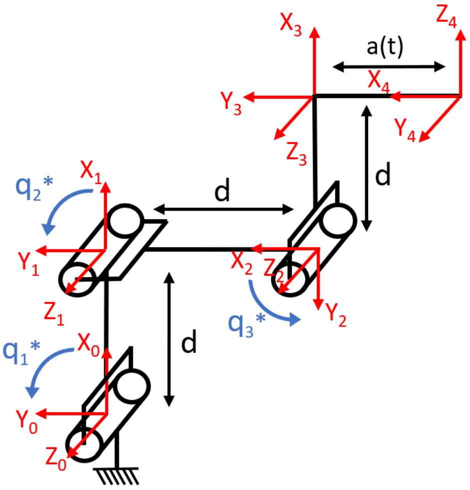

Figure A.7: Geometric model

Link	d_i	a_i	α_i	θ_i
1	0	d	0	q_1^*
2	0	d	0	$180 + q_2^*$
3	0	d	0	q_3^*
4	0	a(t)	90	90

Table A.7: Link parameters

$$^0H_1 = \begin{bmatrix} C_1 & -S_1 & 0 & dC_1 \\ S_1 & C_1 & 0 & dS_1 \\ 0 & 0 & 1 & 0 \\ 0 & 0 & 0 & 1 \end{bmatrix} \quad ^1H_2 = \begin{bmatrix} -C_2 & S_2 & 0 & -dC_2 \\ -S_2 & -C_2 & 0 & -dS_2 \\ 0 & 0 & 1 & 0 \\ 0 & 0 & 0 & 1 \end{bmatrix} \quad ^2H_3 = \begin{bmatrix} C_3 & -S_3 & 0 & dC_3 \\ S_3 & C_3 & 0 & dS_3 \\ 0 & 0 & 1 & 0 \\ 0 & 0 & 0 & 1 \end{bmatrix}$$

$$^3H_4 = \begin{bmatrix} 0 & 0 & 1 & 0 \\ 1 & 0 & 0 & a(t) \\ 0 & 1 & 0 & 0 \\ 0 & 0 & 0 & 1 \end{bmatrix} \qquad ^0H_2 = \begin{bmatrix} -C_{12} & S_{12} & 0 & dC_1 - dC_{12} \\ -S_{12} & -C_{12} & 0 & dS_1 - dS_{12} \\ 0 & 0 & 1 & 0 \\ 0 & 0 & 0 & 1 \end{bmatrix}$$

$$^0H_3 = \begin{bmatrix} -C_{123} & S_{123} & 0 & d(C_1 - C_{12} - C_{123}) \\ -S_{123} & -C_{123} & 0 & d(S_1 - S_{12} - S_{123}) \\ 0 & 0 & 1 & 0 \\ 0 & 0 & 0 & 1 \end{bmatrix}$$

$$^0H_4 = \begin{bmatrix} S_{123} & 0 & -C_{123} & d(C_1 - C_{12} - C_{123}) + a(t)S_{123} \\ -C_{123} & 0 & -S_{123} & d(S_1 - S_{12} - S_{123}) - a(t)C_{123} \\ 0 & 1 & 0 & 0 \\ 0 & 0 & 0 & 1 \end{bmatrix}$$

$$J(q) = \begin{bmatrix} a(t)C_{123} - d(S_1 - S_{12} - S_{123}) & a(t)C_{123} + d(S_{12} + S_{123}) & a(t)C_{123} + dS_{123} \\ a(t)S_{123} + d(C_1 - C_{12} - C_{123}) & a(t)S_{123} - d(C_{12} + C_{123}) & a(t)S_{123} - dC_{123} \\ 0 & 0 & 0 \\ 0 & 0 & 0 \\ 0 & 0 & 0 \\ 1 & 1 & 1 \end{bmatrix}$$

$$det\ J = \begin{vmatrix} a(t)C_{123} - d(S_1 - S_{12} - S_{123}) & a(t)C_{123} + d(S_{12} + S_{123}) & a(t)C_{123} + dS_{123} \\ a(t)S_{123} + d(C_1 - C_{12} - C_{123}) & a(t)S_{123} - d(C_{12} + C_{123}) & a(t)S_{123} - dC_{123} \\ 1 & 1 & 1 \end{vmatrix}$$

$$= -d^2 sin(q_2^*)$$

Appendix B

Detailed profiles of various gait cycles

B.1 Flat ground walking

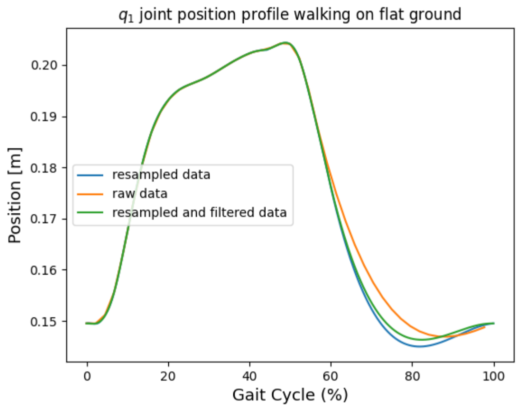

(a) q_1 joint position profile

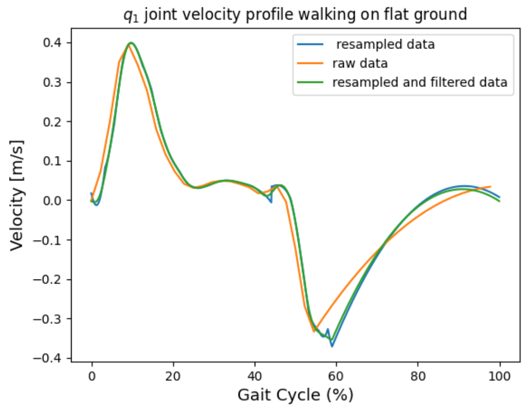

(b) q_1 joint velocity profile

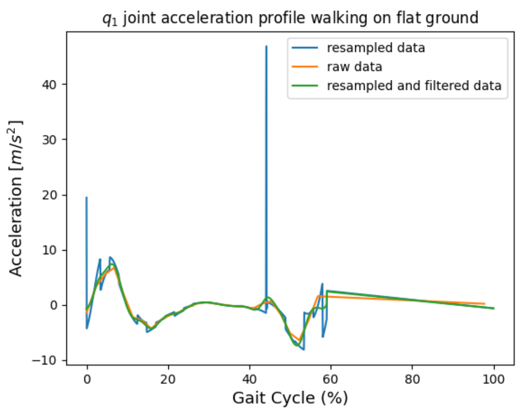

(c) q_1 joint acceleration profile

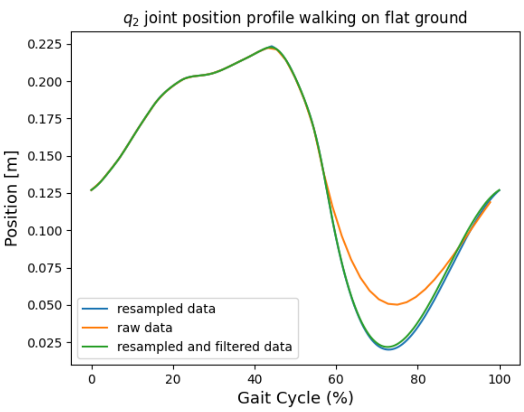

(d) q_2 joint position profile

Figure B.1: Detailed profiles during flat ground walking

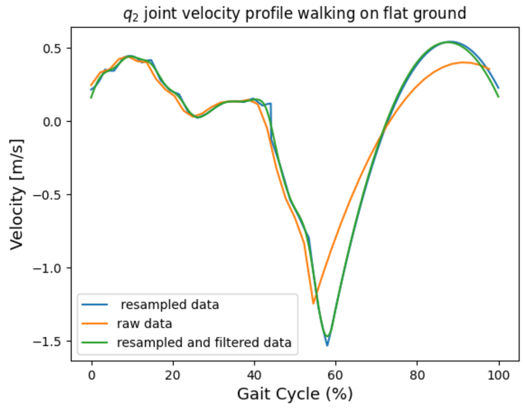

(e) q_2 joint velocity profile

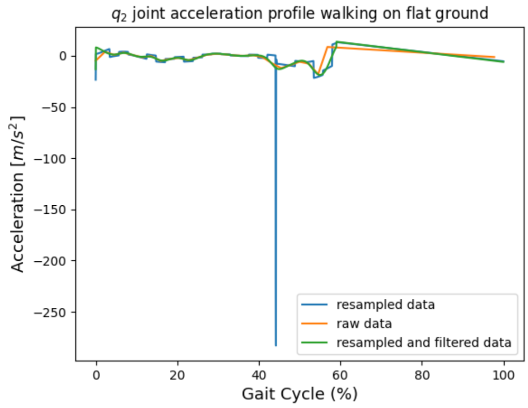

(f) q_2 joint acceleration profile

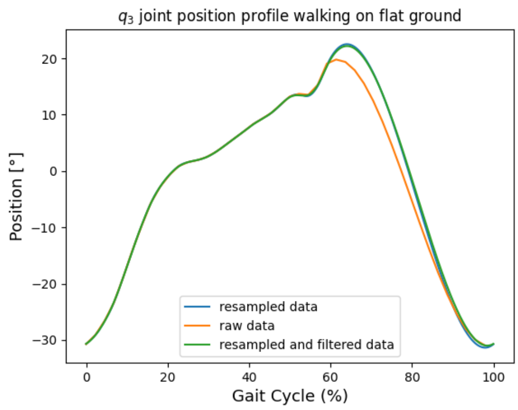

(g) q_3 joint position profile

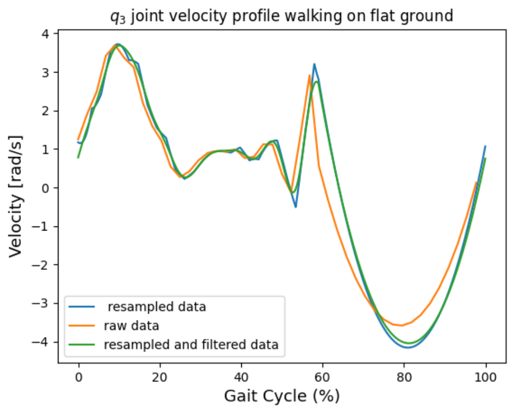

(h) q_3 joint velocity profile

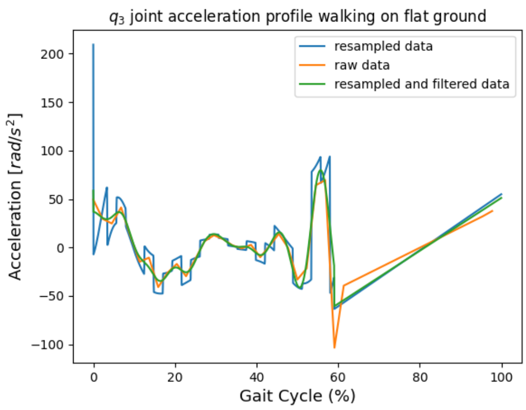

(i) q_3 joint acceleration profile

Figure B.1: Detailed profiles during flat ground walking

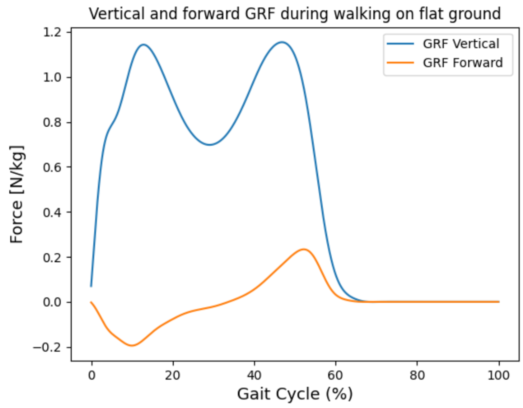

(j) Vertical and forward GRF

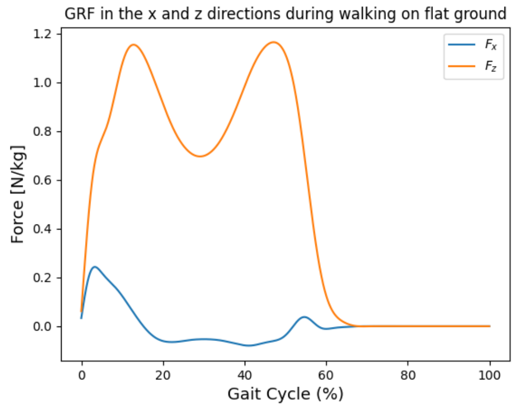

(k) GRF in the x and z directions

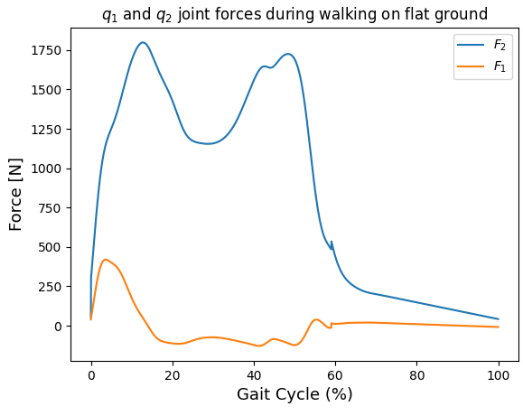

(l) q_1 and q_2 joint forces

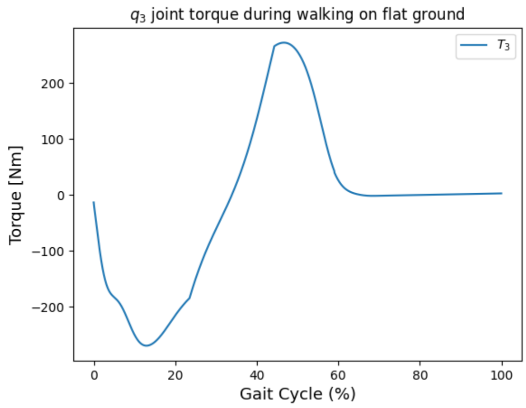

(m) q_3 joint torque

Figure B.1: Detailed profiles during flat ground walking

B.2 Stair ascent

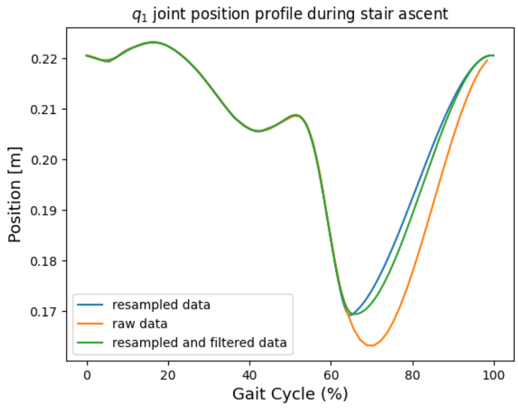

(a) q_1 joint position profile

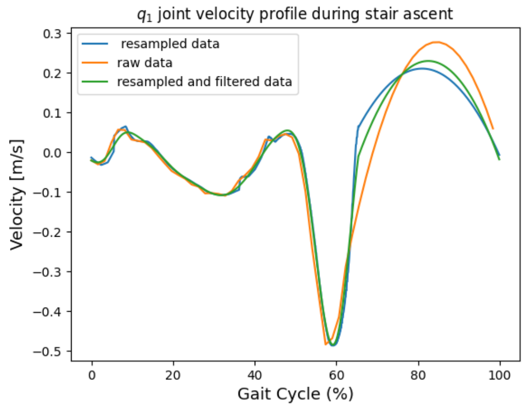

(b) q_1 joint velocity profile

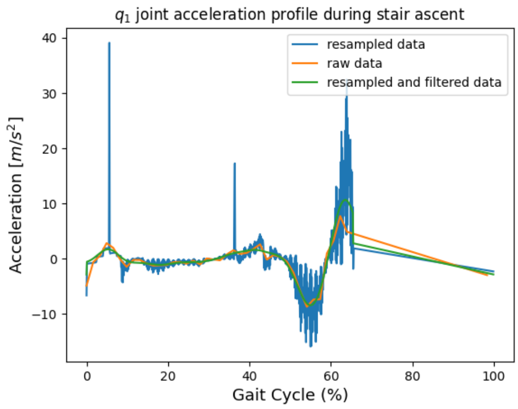

(c) q_1 joint acceleration profile

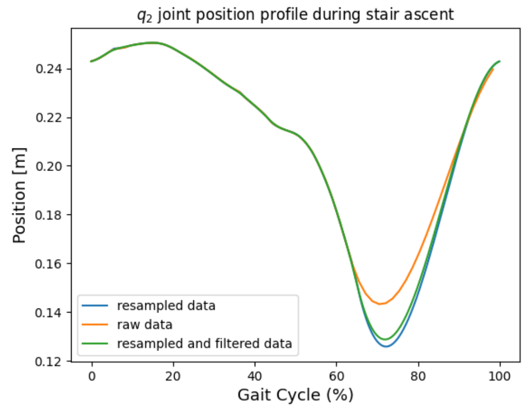

(d) q_2 joint position profile

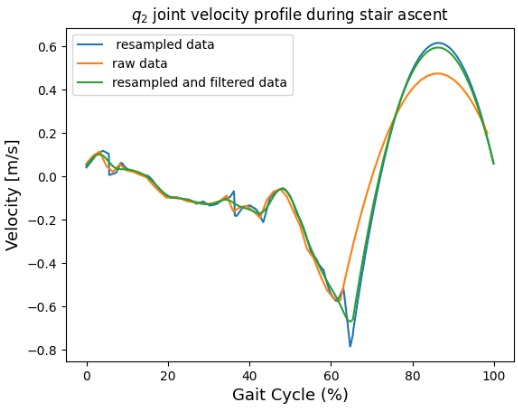

(e) q_2 joint velocity profile

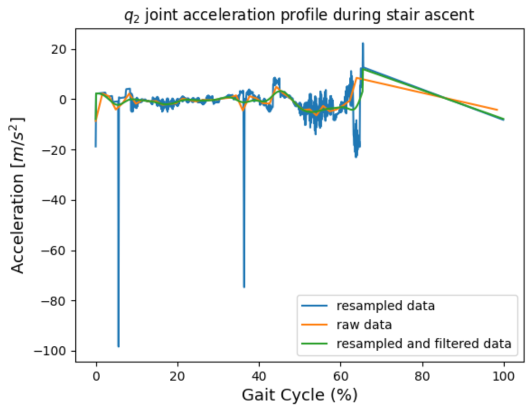

(f) q_2 joint acceleration profile

Figure B.2: Detailed profiles during stair ascent

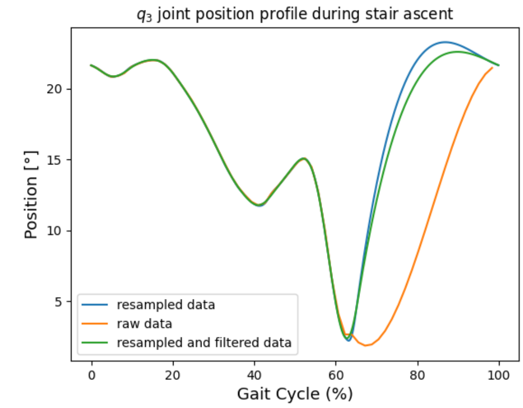

(g) q_3 joint position profile

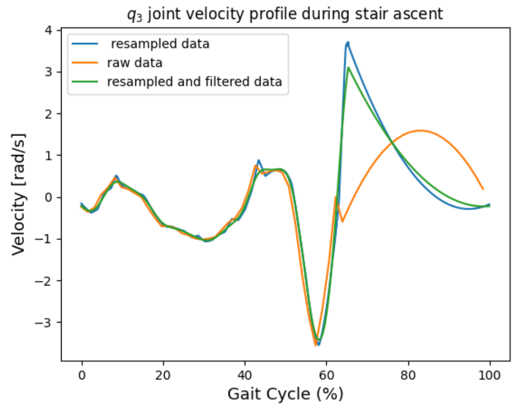

(h) q_3 joint velocity profile

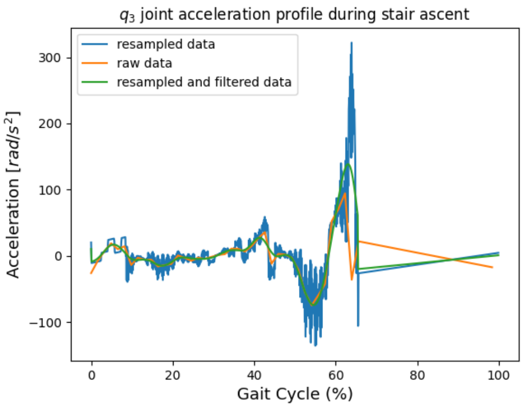

(i) q_3 joint acceleration profile

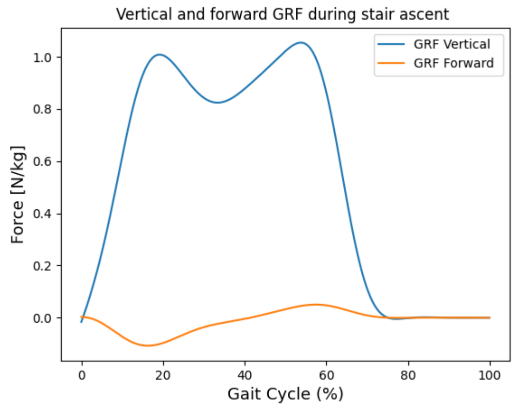

(j) Vertical and forward GRF

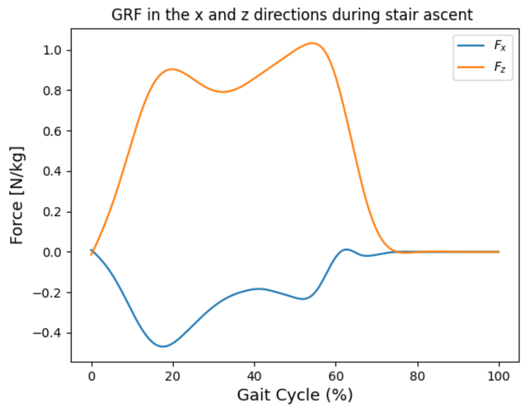

(k) GRF in the x and z directions

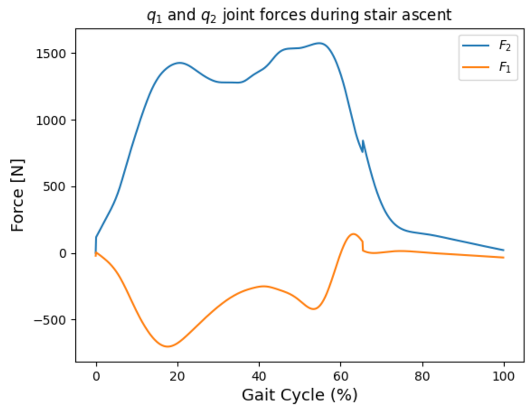

(l) q_1 and q_2 joint forces

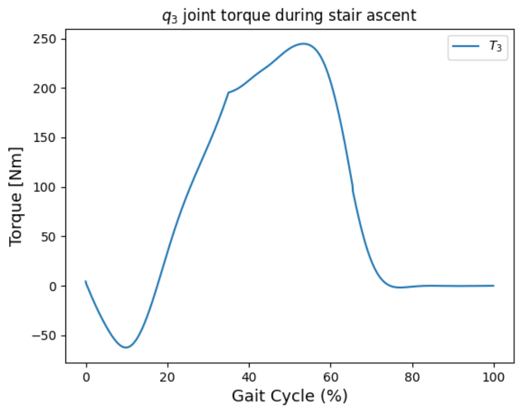

(m) q_3 joint torque

Figure B.2: Detailed profiles during stair ascent

B.3 Stair descent

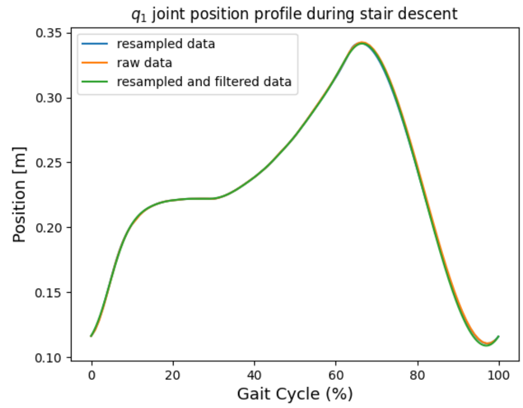

(a) q_1 joint position profile

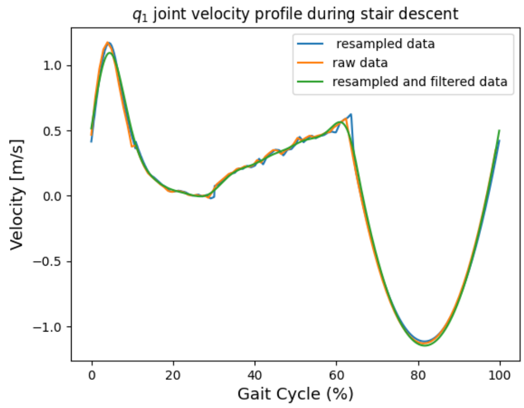

(b) q_1 joint velocity profile

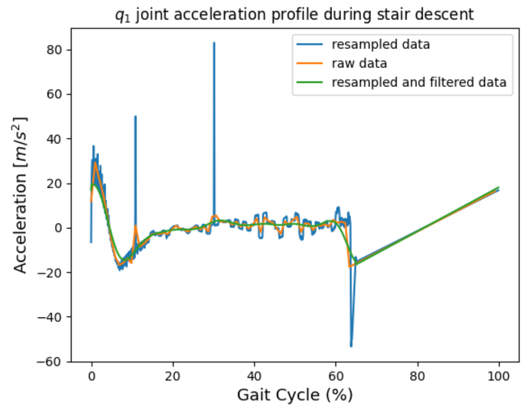

(c) q_1 joint acceleration profile

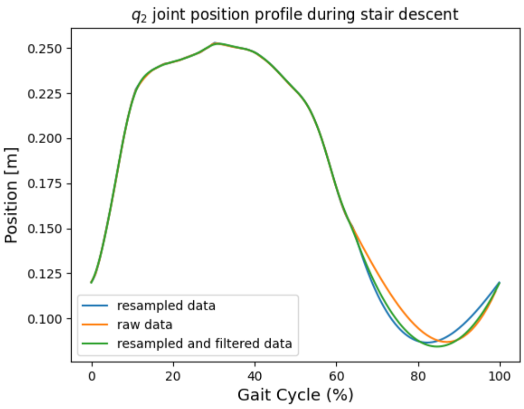

(d) q_2 joint position profile

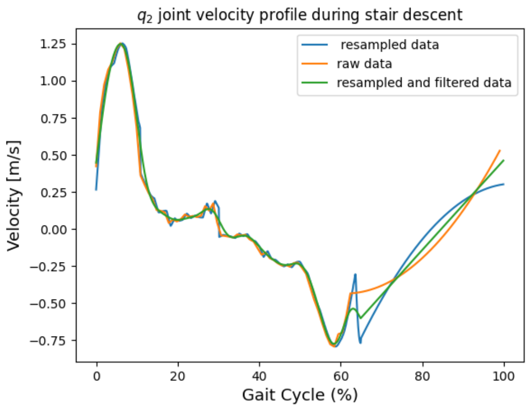

(e) q_2 joint velocity profile

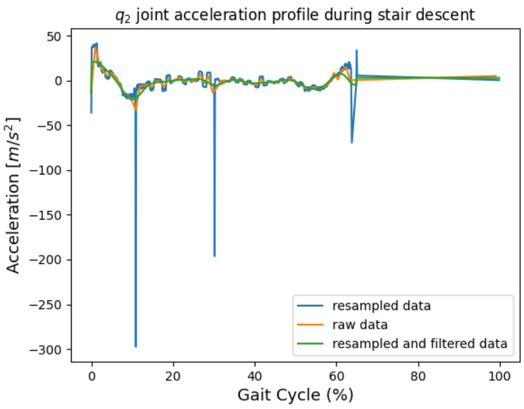

(f) q_2 joint acceleration profile

Figure B.3: Detailed profiles during stair ascent

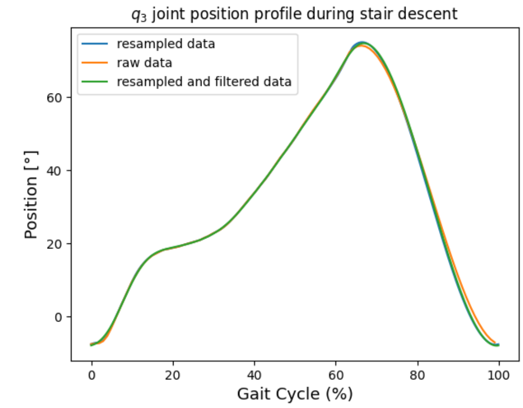

(g) q_3 joint position profile

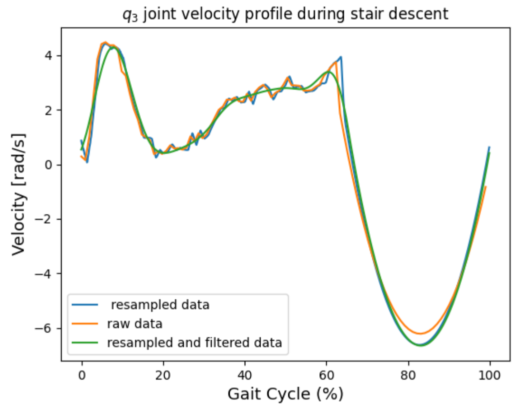

(h) q_3 joint velocity profile

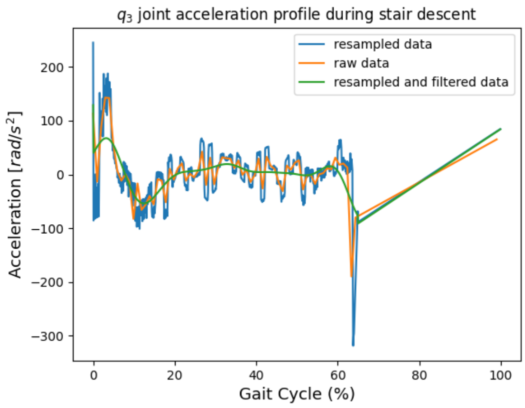

(i) q_3 joint acceleration profile

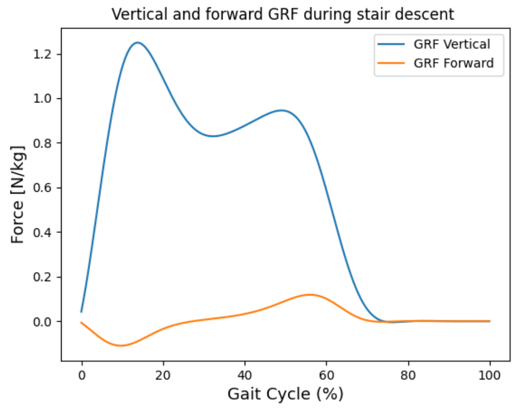

(j) Vertical and forward GRF

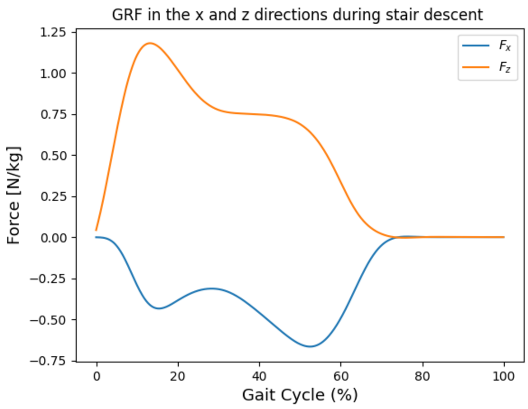

(k) GRF in the x and z directions

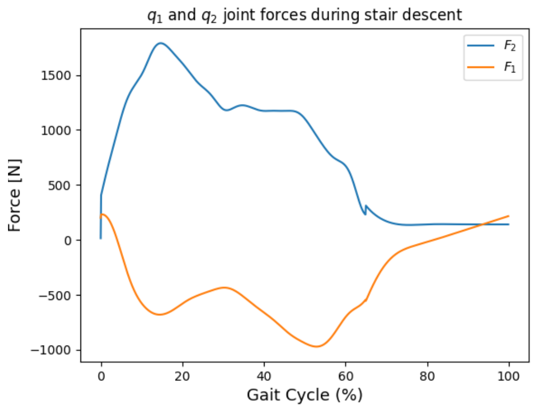

(l) q_1 and q_2 joint forces

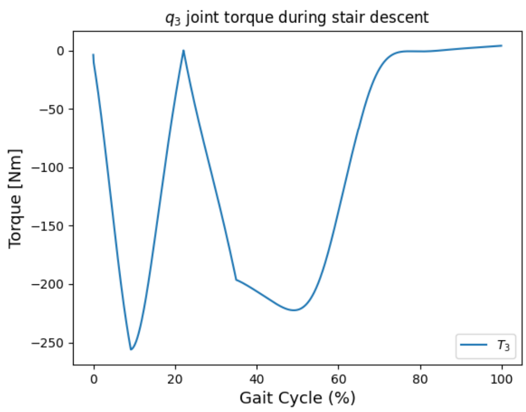

(m) q_3 joint torque

Figure B.3: Detailed profiles during stair descent

B.4 Walking on a 10° slope

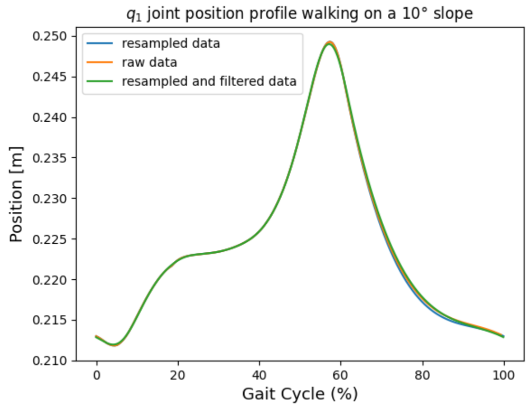

(a) q_1 joint position profile

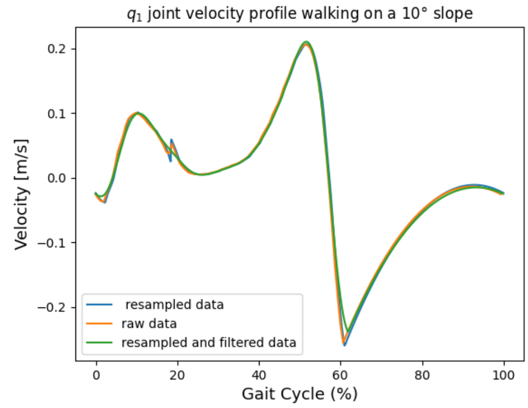

(b) q_1 joint velocity profile

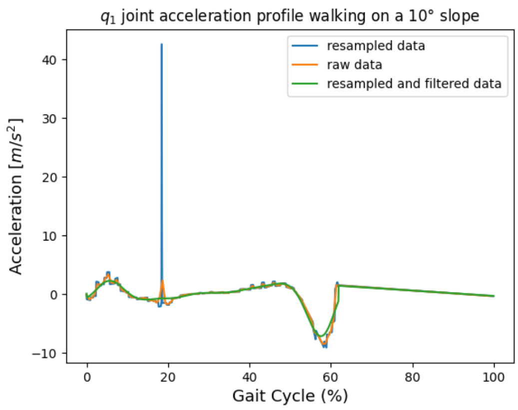

(c) q_1 joint acceleration profile

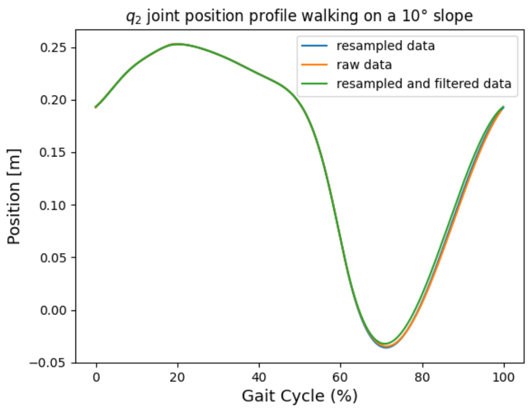

(d) q_2 joint position profile

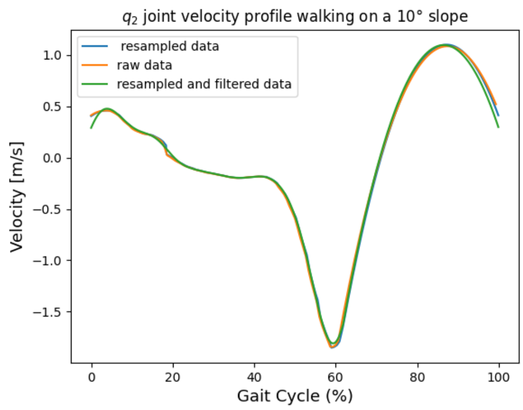

(e) q_2 joint velocity profile

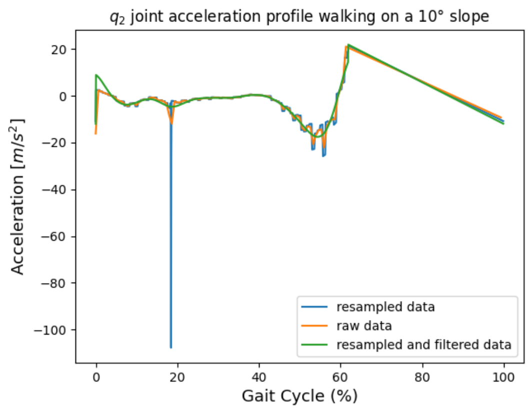

(f) q_2 joint acceleration profile

Figure B.4: Detailed profiles during walking on a 10° slope

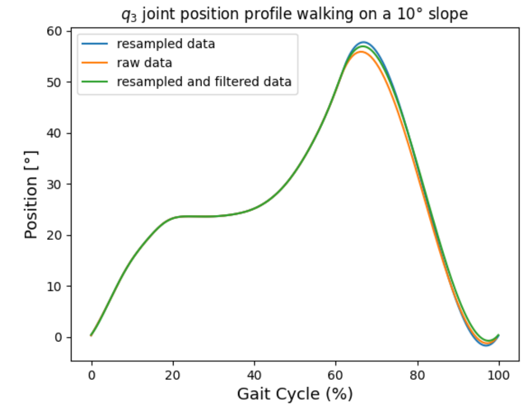

(g) q_3 joint position profile

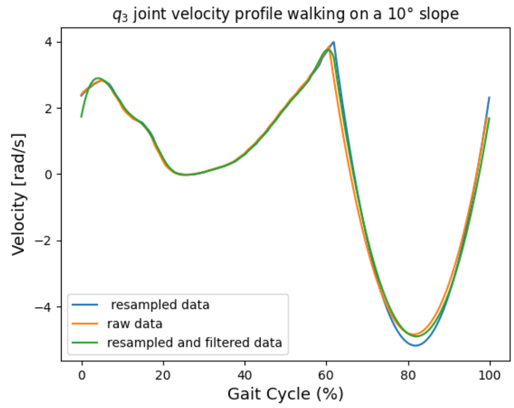

(h) q_3 joint velocity profile

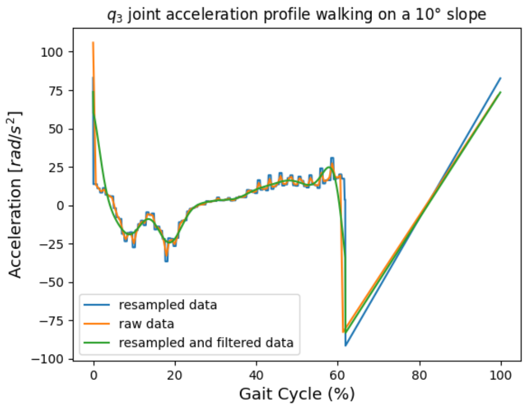

(i) q_3 joint acceleration profile

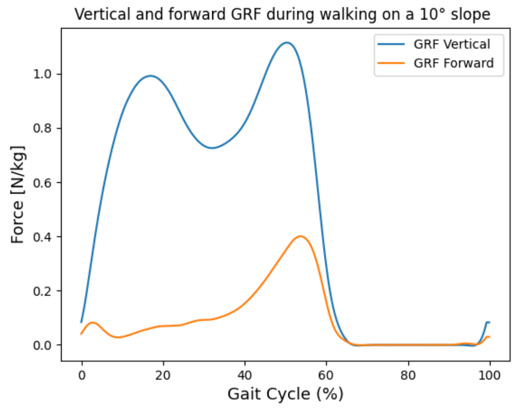

(j) Vertical and forward GRF

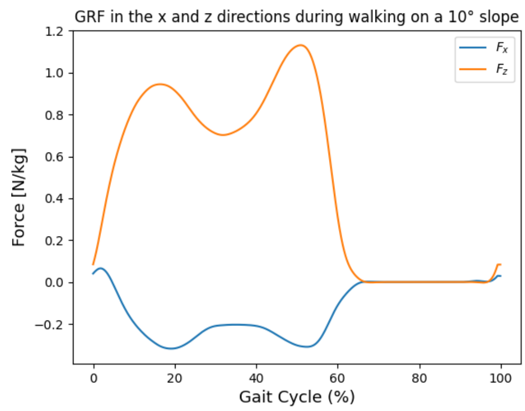

(k) GRF in the x and z directions

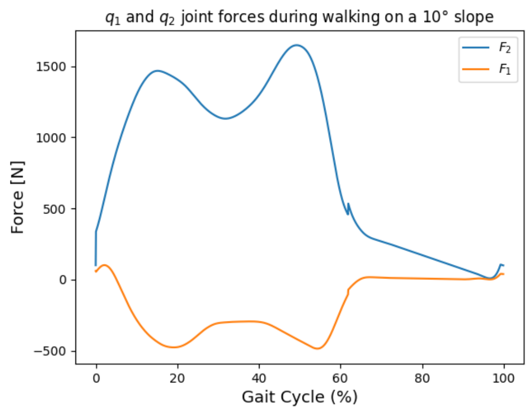

(l) q_1 and q_2 joint forces

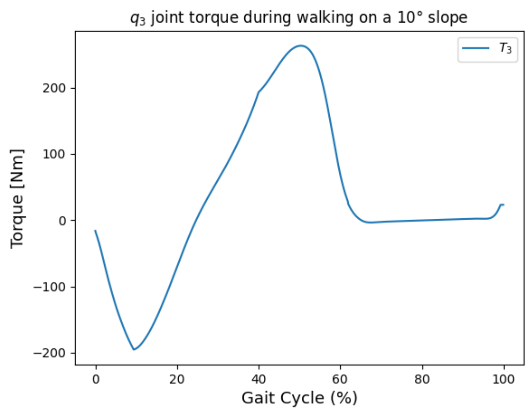

(m) q_3 joint torque

Figure B.4: Detailed profiles during walking on a 10° slope

B.5 Walking on a -10° slope

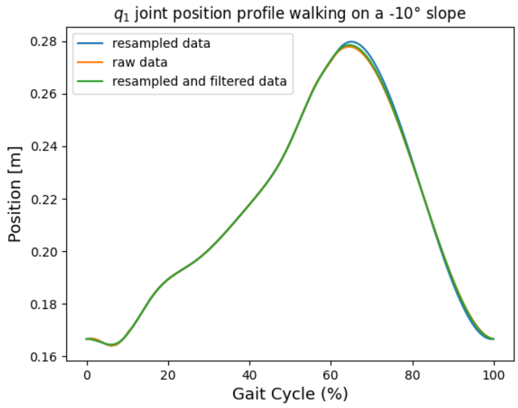

(a) q_1 joint position profile

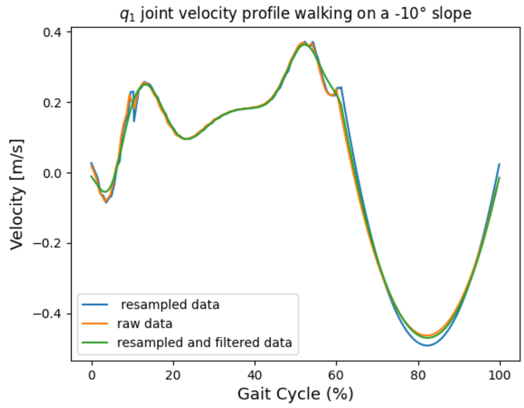

(b) q_1 joint velocity profile

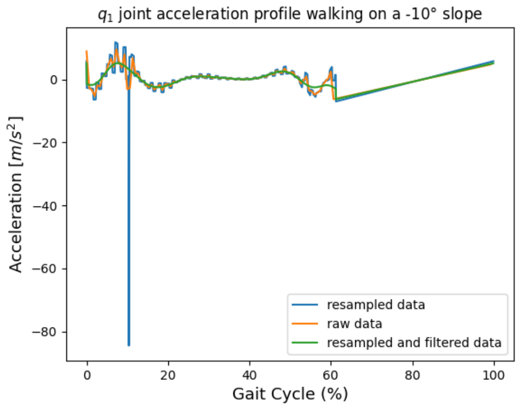

(c) q_1 joint acceleration profile

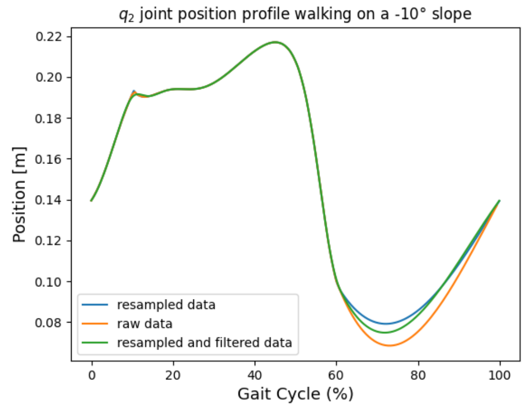

(d) q_2 joint position profile

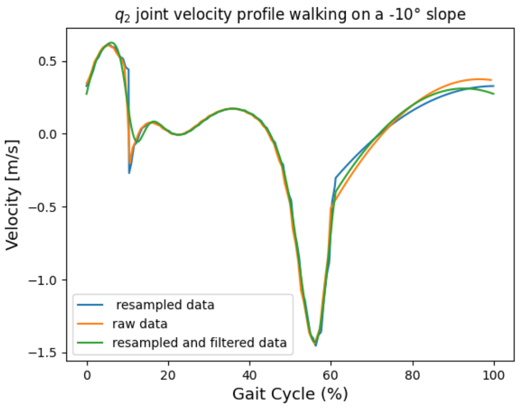

(e) q_2 joint velocity profile

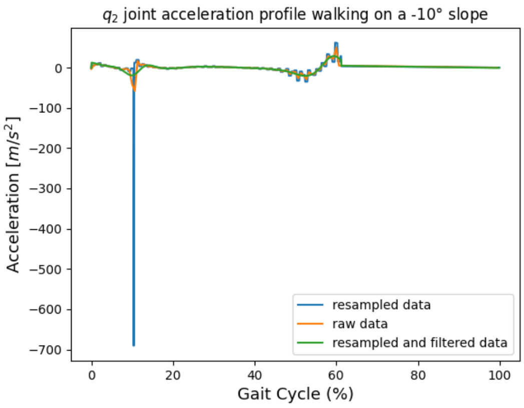

(f) q_2 joint acceleration profile

Figure B.5: Detailed profiles during walking on a -10° slope

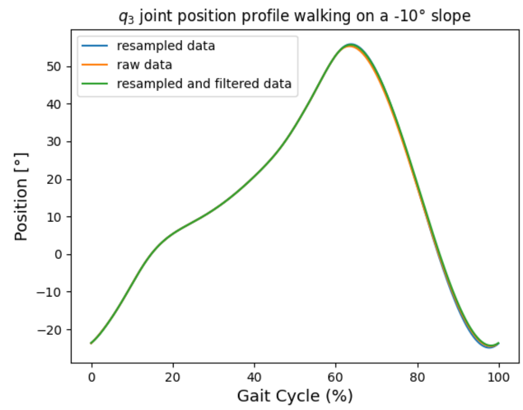

(g) q_3 joint position profile

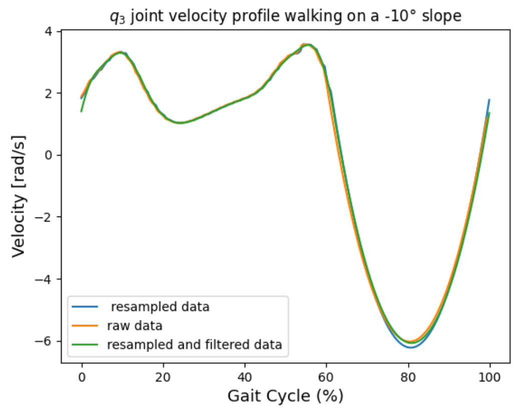

(h) q_3 joint velocity profile

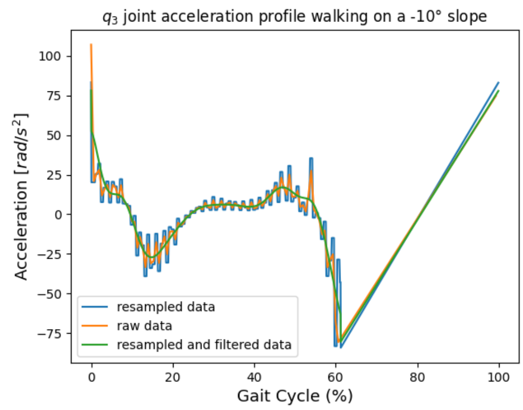

(i) q_3 joint acceleration profile

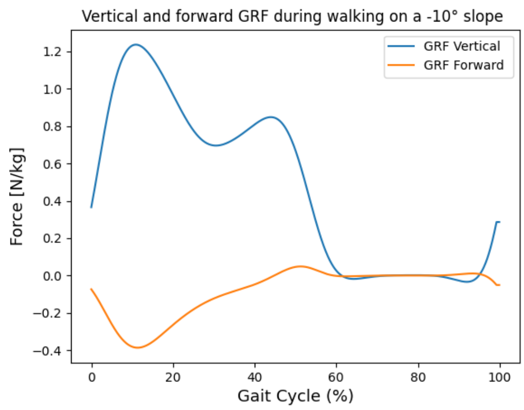

(j) Vertical and forward GRF

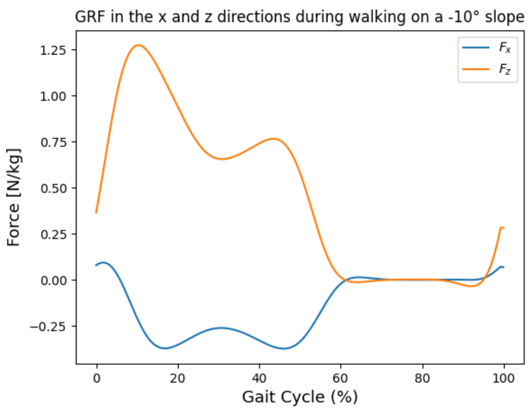

(k) GRF in the x and z directions

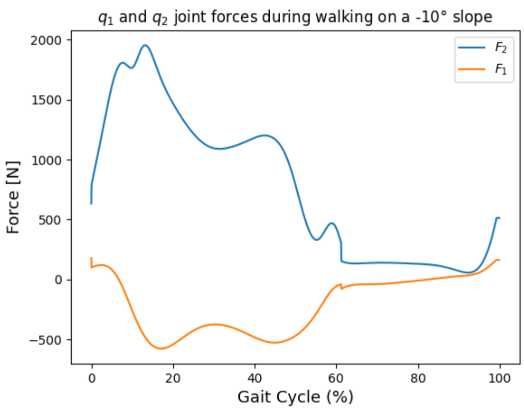

(l) q_1 and q_2 joint forces

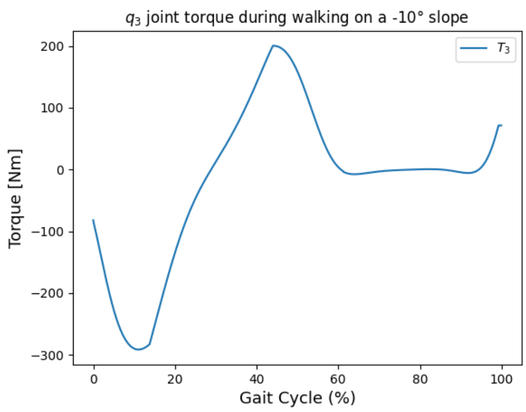

(m) q_3 joint torque

Figure B.5: Detailed profiles during walking on a -10° slope

Appendix C

Direct kinematic and dynamic models of the final design

Here, we will develop the kinematic and dynamic models of the final design. The kinematic model developed here aims to determine the Jacobian matrix that will be required in the final dynamic equations. To establish the kinematic model, we will once again use the Denavit-Hartenberg convention while following the approach outlined in Section 3.2 of [10]. To establish the dynamic model, we will again use the Euler-Lagrange equations as outlined in Section 6 of [10].

In Figure C.1, it can also be noticed that we have introduced new notations. Specifically, the third joint now represents the ankle joint denoted by q_p. Additionally, it can be observed that the variable a(t) has been replaced by a variable b(t). Indeed, a(t) represented the distance between the contact point and the middle of the sole along it. Here, b(t) is slightly different as it characterizes the distance between the contact point and the intersection between the sole and the line extending from the ankle joint to the center of mass. Finally, a new parameter ϕ is introduced, as illustrated in Figure C.2. Finally, we have also introduced the following notations :

- $S_{i-j} = \sin(q_i - q_j)$
- $C_{i-j} = \cos(q_i - q_j)$

$\forall i, j \in \{1, 2, p\}$.

C.1 Direct kinematic model

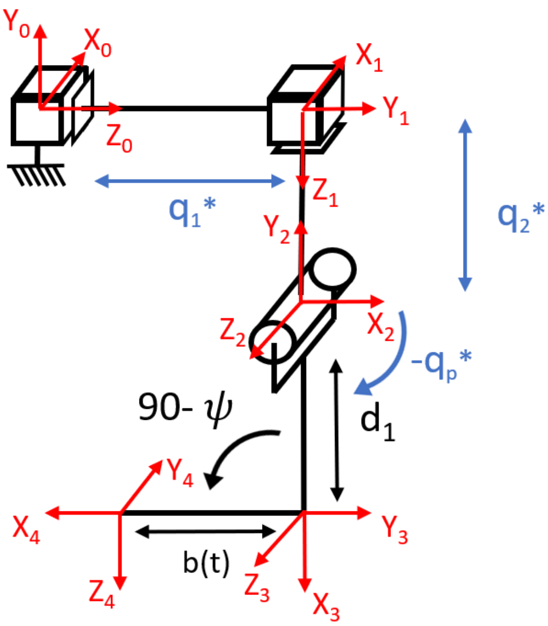

Figure C.1: Geometric model

Link	d_i	a_i	α_i	θ_i
1	q_1^*	0	90	0
2	q_2^*	0	-90	90
3	0	d_1	0	q_p^*
4	0	b(t)	-90	-90-ϕ

Table C.1: Link parameters

$$
{}^0H_1 = \begin{bmatrix} 1 & 0 & 0 & 0 \\ 0 & 0 & -1 & 0 \\ 0 & 1 & 0 & q_1^* \\ 0 & 0 & 0 & 1 \end{bmatrix} \quad
{}^1H_2 = \begin{bmatrix} 0 & 0 & -1 & 0 \\ 1 & 0 & 0 & 0 \\ 0 & -1 & 0 & q_2^* \\ 0 & 0 & 0 & 1 \end{bmatrix} \quad
{}^2H_3 = \begin{bmatrix} C_p & -S_p & 0 & d_1C_p \\ S_p & C_p & 0 & d_1S_p \\ 0 & 0 & 1 & 0 \\ 0 & 0 & 0 & 1 \end{bmatrix}
$$

$$
{}^3H_4 = \begin{bmatrix} -S_\phi & 0 & C_\phi & -b(t)S_\phi \\ -C_\phi & 0 & -S_\phi & -b(t)C_\phi \\ 0 & -1 & 0 & 0 \\ 0 & 0 & 0 & 1 \end{bmatrix} \quad
{}^0H_2 = \begin{bmatrix} 0 & 0 & -1 & 0 \\ 0 & 1 & 0 & -q_2^* \\ 1 & 0 & 0 & q_1^* \\ 0 & 0 & 0 & 1 \end{bmatrix}
$$

$$
{}^0H_3 = \begin{bmatrix} 0 & 0 & -1 & 0 \\ S_p & C_p & 0 & d_1S_p + q_2^* \\ C_p & -S_p & 0 & d_1C_p + q_1^* \\ 0 & 0 & 0 & 1 \end{bmatrix}
$$

$$
{}^0H_4 = \begin{bmatrix} 0 & 1 & 0 & 0 \\ -C_{p-\phi} & 0 & S_{p-\phi} & d_1S_\phi - q_2^* - b(t)C_{p-\phi} \\ S_{p-\phi} & 0 & C_{p-\phi} & q_1^* + d_1C_\phi + b(t)S_{p-\phi} \\ 0 & 0 & 0 & 1 \end{bmatrix} \quad
J(q) = \begin{bmatrix} 0 & 0 & 0 \\ 0 & -1 & d_1C_\phi + b(t)S_{p-\phi} \\ 1 & 0 & b(t)C_{p-\phi} - d_1S_\phi \\ 0 & 0 & -1 \\ 0 & 0 & 0 \\ 0 & 0 & 0 \end{bmatrix}
$$

C.2 Dynamic model

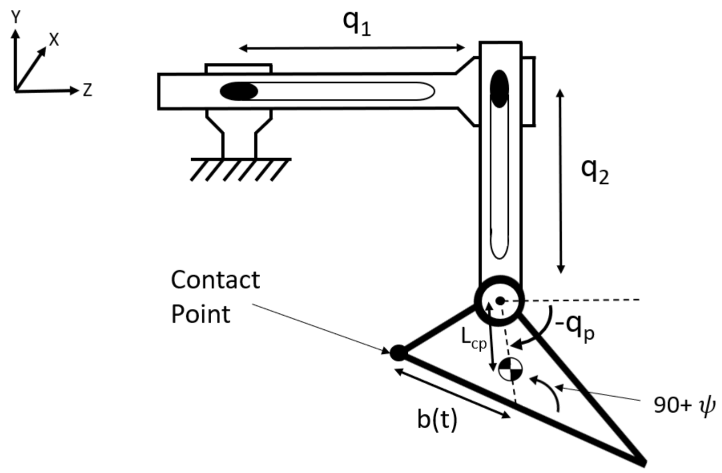

Figure C.2: Representation of the scenario with q_1 denoting the position of the horizontal linear actuator (link 1), q_2 representing the position of the vertical linear actuator (link 2), q_p indicating the angular position of the centre of mass of the prosthesis (link 3), L_{cp} signifying the distance between the center of rotation of the prosthesis joint and its center of mass, and b(t) denoting the time-dependent position of the contact point between the prosthesis and the substitute ground.

Link 1 will represent the horizontal linear movement, link 2 the vertical linear movement, and link p the rotational movement of the prosthesis. The position of the center of mass of these three links with respect to the inertial frame is given by :

$$Link \quad 1 \quad : \begin{bmatrix} 0 \\ K_2 \\ K_1 + q_1 \end{bmatrix} ; \quad Link \quad 2 \quad : \begin{bmatrix} 0 \\ K_2 + q_2 \\ K_1 + q_1 \end{bmatrix} ; \quad Link \quad p \quad : \begin{bmatrix} 0 \\ K_2 + q_2 + L_{cp} sin(q_p) \\ K_1 + q_1 + L_{cp} cos(q_p) \end{bmatrix}$$

where K_1 and K_2 are constants. Therefore, we can calculate the velocity of their center of mass as :

$$v_{c1} = J_{vc1}\dot{q} \quad ; \quad v_{c2} = J_{vc2}\dot{q} \quad ; \quad v_{cp} = J_{vcp}\dot{q}$$

where,

$$J_{vc1} = \begin{bmatrix} 0 & 0 & 0 \\ 0 & 0 & 0 \\ 1 & 0 & 0 \end{bmatrix} ; \quad J_{vc2} = \begin{bmatrix} 0 & 0 & 0 \\ 0 & 1 & 0 \\ 1 & 0 & 0 \end{bmatrix} ; \quad J_{vcp} = \begin{bmatrix} 0 & 0 & 0 \\ 0 & 1 & L_{cp} cos(q_p) \\ 1 & 0 & -L_{cp} sin(q_p) \end{bmatrix} ; \quad \dot{q} = \begin{bmatrix} \dot{q}_1 \\ \dot{q}_2 \\ \dot{q}_p \end{bmatrix}$$

So, we can write the total translational kinetic energy as :

$$\frac{1}{2}\dot{q}^T\{m_1J_{vc1}^TJ_{vc1} + m_2J_{vc2}^TJ_{vc2} + m_pJ_{vcp}^TJ_{vcp}\}\dot{q}$$

where m_1, m_2, and m_p are the respective masses of link 1, 2 and p . Next, we can also provide the expression for the total rotational kinetic energy as :

$$\frac{1}{2}\dot{q}^T\{I_p\begin{bmatrix}0 & 0 & 0\\0 & 0 & 0\\0 & 0 & 1\end{bmatrix}\}\dot{q}$$

Where I_p is the mass moment of inertia of link p. Therefore, we can express the total kinetic energy 'K' of the manipulator as :

$$K = \frac{1}{2}\dot{q}^T\{m_1J_{vc1}^TJ_{vc1} + m_2J_{vc2}^TJ_{vc2} + m_pJ_{vcp}^TJ_{vcp} + I_p\begin{bmatrix}0 & 0 & 0\\0 & 0 & 0\\0 & 0 & 1\end{bmatrix}\}\dot{q} = \frac{1}{2}\dot{q}^TD(q)\dot{q}$$

Where D(q) is called the 'Inertia Matrix' and its expression is :

$$D(q) = \begin{bmatrix}m_1+m_2+m_p & 0 & -m_pL_{cp}sin(q_p)\\0 & m_2+m_p & m_pL_{cp}cos(q_p)\\-m_pL_{cp}sin(q_p) & m_pL_{cp}cos(q_p) & m_pL_{cp}^2+I_3\end{bmatrix}$$

We can now calculate the Christoffel symbols, the general expression of which is :

$$c_{ijk} = \frac{1}{2}(\frac{\partial d_{kj}}{\partial q_i} + \frac{\partial d_{ki}}{\partial q_j} - \frac{\partial d_{ij}}{\partial q_k})$$

The non-zero Christoffel symbols are :

$$c_{331} = -m_pL_{cp}cos(q_p)$$

$$c_{332} = -m_pL_{cp}sin(q_p)$$

Now, we need to compute the potential energy 'P' of the 3 links :

$$P_1 = m_1gh$$

$$P_2 = m_2g(h+q_2)$$

$$P_3 = m_pg(h+q_2+L_{cp}sin(q_p)$$

Where 'h' is a constant and 'g' the gravitational acceleration. The total potential energy is thus given by : $P = P_1 + P_2 + P_3$. Finally, if we defined :

$$\phi_k = \frac{\partial P}{\partial q_k}$$

We can write the Euler-Lagrange equations as :

$$\sum_i d_{kj}(q)\ddot{q}_j + \sum_{i,j} c_{i,j,k}(q)\dot{q}_i\dot{q}_j + \phi_k(q) = \tau_k \quad , \quad k = 1, 2, p$$

Where τ_k is composed of the forces and torque delivered by the 3 actuators, as well as the external forces and torques acting on the system. In our case, only two external forces in the y and z directions act on our system, which are the reaction forces between the ground and the prosthesis. So we have:

$$\begin{bmatrix} \tau_1 \\ \tau_2 \\ \tau_p \end{bmatrix} = \begin{bmatrix} F_1 \\ F_2 \\ T_p \end{bmatrix} + J^T(q)F_{ext} = \begin{bmatrix} F_1 + F_z \\ F_2 + F_y \\ T_p + F_y[d_1cos(q_3) + b(t)sin(q_p)] + F_z[b(t)cos(q_p) - d_1sin(q_p)] \end{bmatrix}$$

Where F_1 and F_2 are the forces delivered by actuators q_1 and q_2, T_p is the torque delivered by prosthesis joint q_p, F_y and F_z are respectively the forces in the y and z (positive) directions at the contact point with the prosthesis, and $J^T(q)$ is the transpose of the Jacobian matrix of the system, the derivation of which can be found in Appendix C.2. So we can finally write the 3 dynamical equations of the system as :

$$(m_1 + m_2 + m_p)\ddot{q}_1 - (m_pL_{cp}sin(q_p))\ddot{q}_p - (m_pL_{cp}cos(q_p))\dot{q}_p{}^2 = F_1 - F_z \tag{C.1}$$

$$(m_2 + m_p)\ddot{q}_2 + (m_pL_{cp}cos(q_p))\ddot{q}_p - (m_pL_{cp}sin(q_p))\dot{q}_p{}^2 + (m_2 + m_p)g = F_2 - F_y \tag{C.2}$$

$$\begin{aligned} &-(m_pL_{cp}sin(q_p))\ddot{q}_1 + (m_pL_{cp}cos(q_p))\ddot{q}_2 + (m_pL_{cp}^2 + I_p)\ddot{q}_p + m_pL_{cp}gcos(q_p) = \\ &\qquad T_p + F_y[d - 1cos(q_p) + b(t)sin(q_p)] + F_z[b(t)cos(q_p) - d_1sin(q_p)] \end{aligned} \tag{C.3}$$

Appendix D

Technical drawings

D.1 Coupling

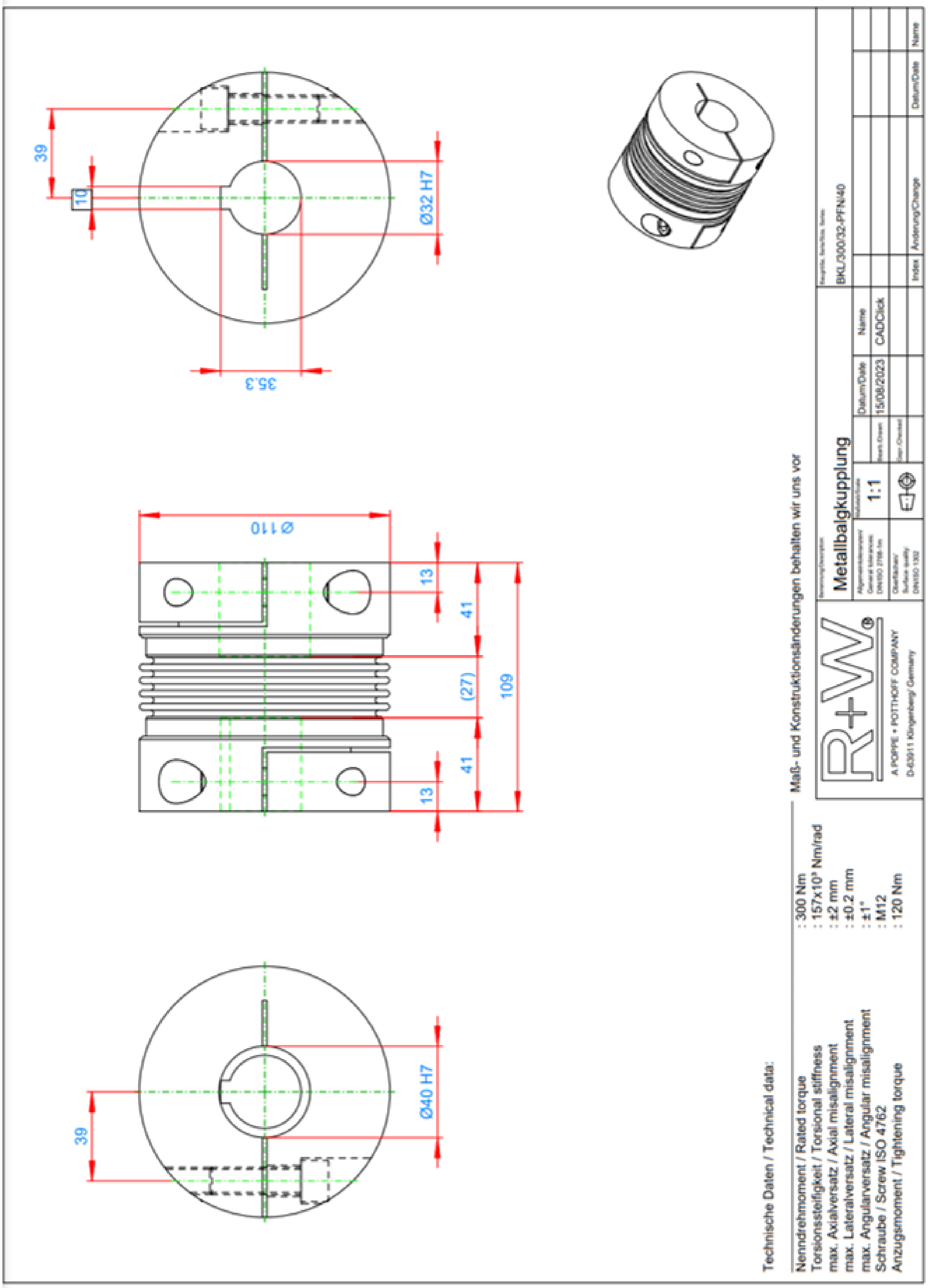

Figure D.1: Technical drawings of the BKL 300 32 PFN 40 1 coupling from [23]

D.2 Bearing unit

High-Base Pillow Block Units

FYH

UCPH
Cylindrical bore (with set screws)
d 12 ~ 50 mm

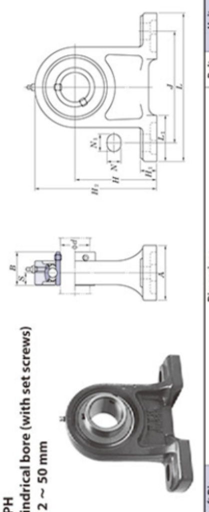

Variations of tolerance of distance from mounting bottom to center of spherical bore (Δ_{Hs})

Unit: mm

Housing No.	Δ_{Hs}
PH204~PH210	±0.15

Shaft Dia. d mm	Shaft Dia. d inch	H inch / mm	L	A	J	N	N_1	H_1	H_2	L_1	B	S	Bolt Size inch / mm	Unit No.	Housing No.	Bearing No.	C_r (kN)	C_{0r} (kN)	Factor f_0	Mass kg
12		2 3/4 70	5 127	1 9/16 40	3 3/4 95	1/2 13	3/4 19	19/32 15	3 31/32 101	1 13/16 46	1.220 31	0.500 12.7	3/8 M10	UCPH201	PH204	UC201	12.8	6.65	13.2	0.96
	1/2													UCPH201-8		UC201-8				
15														UCPH202		UC202				0.94
	5/8													UCPH202-10		UC202-10				
17														UCPH203		UC203				0.93
	3/4													UCPH204-12		UC204-12				
20														UCPH204		UC204				0.91
	7/8	3 5/32 80	5 1/2 140	1 31/32 50	4 1/8 105	1/2 13	3/4 19	5/8 16	4 1/2 114	1 15/16 49	1.343 34.1	0.563 14.3	3/8 M10	UCPH205-14	PH205	UC205-14	14.0	7.85	13.9	1.2
	15/16													UCPH205-15		UC205-15				
25														UCPH205		UC205				
	1													UCPH205-16		UC205-16				
	1 1/8	3 35/64 90	6 1/2 165	1 31/32 50	4 3/4 121	21/32 17	13/16 21	23/32 18	5 1/8 130	2 7/32 56	1.500 38.1	0.626 15.9	1/2 M14	UCPH206-18	PH206	UC206-18	19.5	11.3	13.9	1.6
30														UCPH206		UC206				
	1 3/16													UCPH206-19		UC206-19				
	1 1/4													UCPH206-20		UC206-20				
	1 1/4	3 47/64 95	6 9/16 167	2 3/8 60	5 127	21/32 17	13/16 21	23/32 18	5 1/2 140	2 1/8 54	1.689 42.9	0.689 17.5	1/2 M14	UCPH207-20	PH207	UC207-20	25.7	15.4	13.9	2.0
	1 5/16													UCPH207-21		UC207-21				
	1 3/8													UCPH207-22		UC207-22				
35														UCPH207		UC207				
	1 7/16													UCPH207-23		UC207-23				
	1 1/2	3 15/16 100	7 1/4 184	2 3/4 70	5 13/32 137	21/32 17	13/16 21	25/32 20	5 29/32 150	2 1/4 57	1.937 49.2	0.748 19	1/2 M14	UCPH208-24	PH208	UC208-24	29.1	17.8	14.0	2.7
	1 9/16													UCPH208-25		UC208-25				
40														UCPH208		UC208				
	1 5/8	4 9/64 105	7 15/32 190	2 3/4 70	5 3/4 146	21/32 17	13/16 21	25/32 20	6 7/32 158	2 9/32 58	1.937 49.2	0.748 19	1/2 M14	UCPH209-26	PH209	UC209-26	34.1	21.3	14.0	3.0
	1 11/16													UCPH209-27		UC209-27				
	1 3/4													UCPH209-28		UC209-28				
45														UCPH209		UC209				
	1 7/8	4 21/64 110	8 1/8 206	2 3/4 70	6 1/4 159	25/32 20	7/8 22	7/8 22	6 1/2 165	2 9/16 65	2.031 51.6	0.748 19	5/8 M16	UCPH210-30	PH210	UC210-30	35.1	23.3	14.4	3.5
	1 15/16													UCPH210-31		UC210-31				
50														UCPH210		UC210				
	2													UCPH210-32		UC210-32				

Remarks
1. In Part No. of unit, fitting codes follow bore diameter codes. (See **Table 10.5** in P.62.)
2. Part No. of the applicable grease fitting is A-1/4-28UNF.
3. As for the triple seal type product (from 201 to 205 are the double seal type products), suffix code L3 (or L2) follows Part No. of unit or bearing. (Example of Part No. : UCPH206JL3, UC206L3)
4. As for the dimensions and forms of applicable bearings, see the dimensional tables of ball bearing for unit.
5. Tapered bore (with adapter) type products are also available. (Example of Part No. : UKPH205J + H2305X, UK205 + H2305X)

Figure D.2: Technical drawings of the UCPH208 bearing housing from [24]

D.3 Mounting bracket

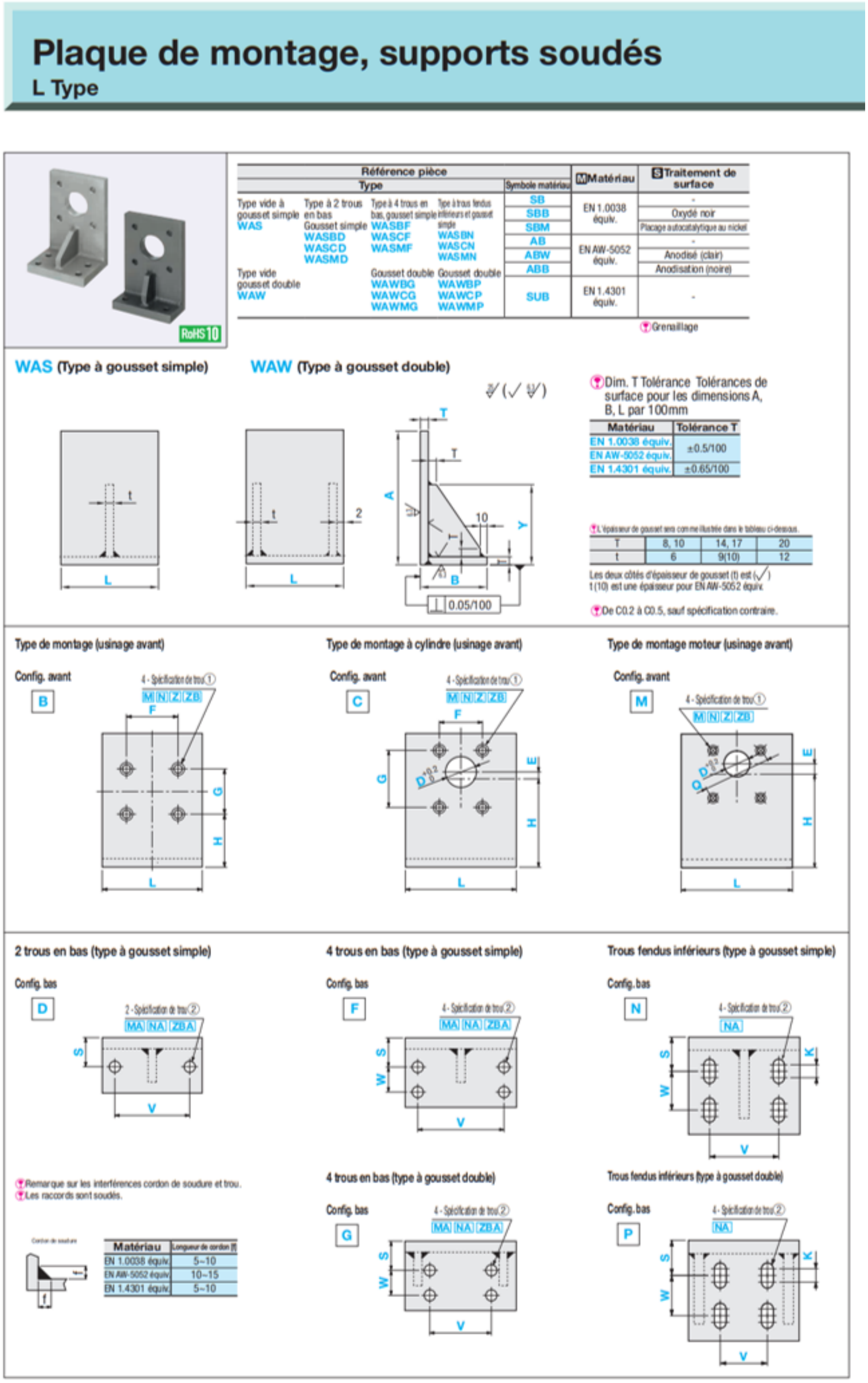

Figure D.3: Technical drawings of the mounting bracket with reference WAWMP-ABW-T10-A160-B120-L184-Y80-H100-E0-Q120-D90-N8-V137-S60-W40-NA12-K4-CC5-RC from [25]

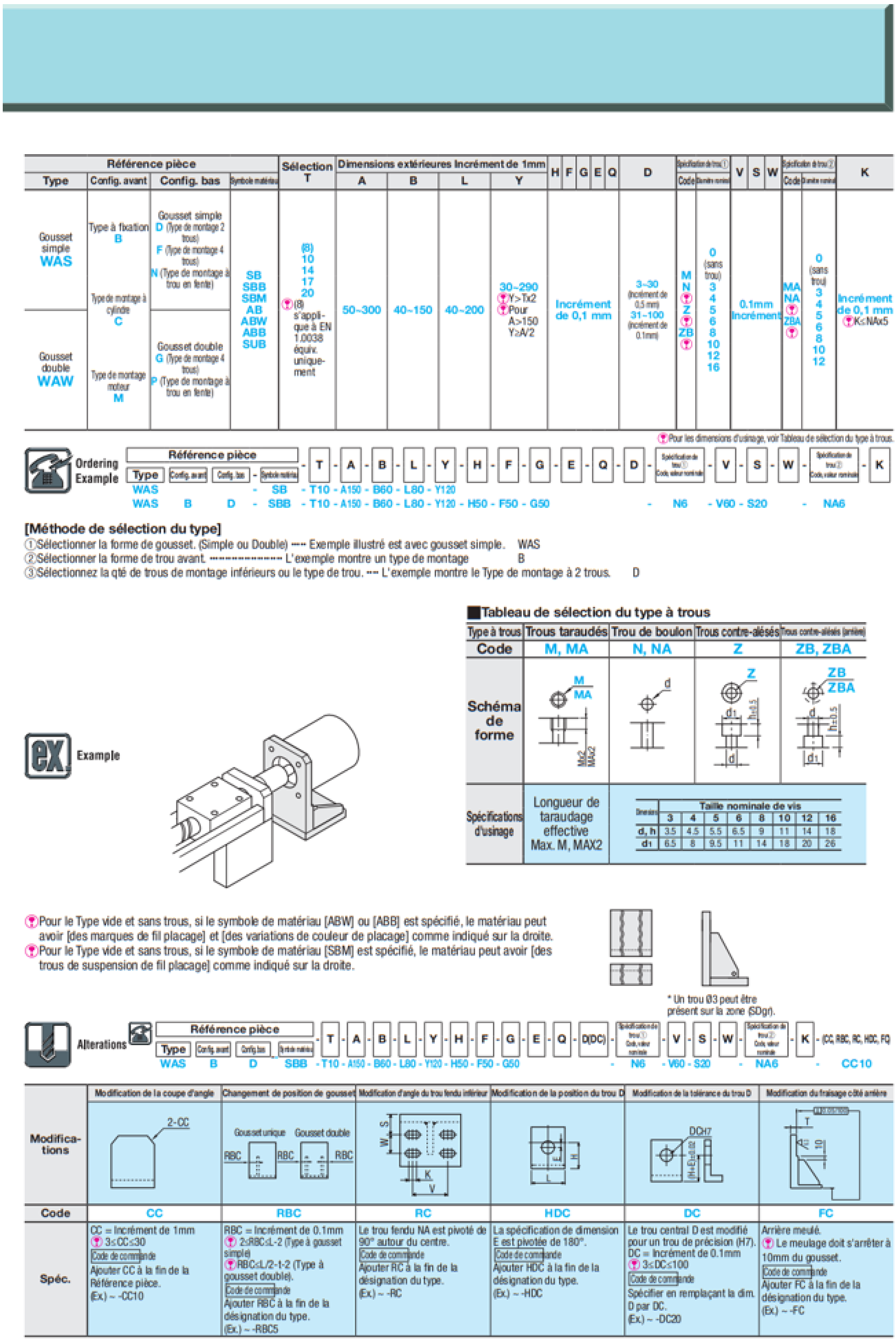

Figure D.3: Technical drawings of the mounting bracket with reference WAWMP-ABW-T10-A160-B120-L184-Y80-H100-E0-Q120-D90-N8-V137-S60-W40-NA12-K4-CC5-RC from [25]

D.4 Siemens motor

Basic motor data	
Motor type	Permanent-magnet synchronous motor, Natural cooling, IP64
Motor type	High Dynamic
Static torque	12.00 Nm
Static current	10.7 A
Maximum torque	33.00 Nm
Maximum current	42.0 A
Maximum speed	6,000 rpm
Rotor moment of inertia	6.0000 kgcm²
Weight	9.0 kg

Rated data	
SINAMICS S210, 3AC 480V	
Rated speed	3,000 rpm
Rated torque	8.60 Nm
Rated current	8.1 A
Rated power	2.70 kW

Encoder system	
Encoder system	Encoder AM22DQC: Absolute encoder 22 bit + 12 bit multiturn

Motor connection	
Connection type	OCC for S210
Connector size	M23

Mechanical data	
Design acc. to Code I	IM B5 (IM V1, IM V3)
Vibration severity grade	Grade A
Shaft height	63
Flange size (AB)	125 mm
Centering ring (N)	110 mm
Hole circle (M)	130 mm
Screw-on hole (S)	9.0 mm
Overall length (LB)	193 mm
Diameter of shaft (D)	24 mm
Length of shaft (E)	50 mm
Length of flange diagonal (P)	158 mm
Shaft end	Fitted key
Color of the housing	Standard (Anthracite, similar to RAL 7016)

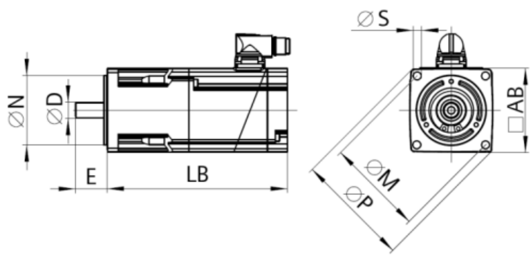

Figure D.4: Data sheet for SIMOTICS S-1FK2 motor with reference 1FK2106-4AF00-1MA0. Data sheet generated with the Siemens product configurator [27].

Appendix E

NTN-SNR Linear actuator characteristics tables

E.1 Linear axis with toothed belt / Ω - drive

Type	Axis profile cross section [mm]	Feed constant [mm/rev.]	Allowable dynamic operating load [N]	Guiding system	Maximum velocity [m/s]	Maximum total length [m]	Maximum dynamic load capacity [N]		Maximum dynamic load moments [Nm]		
							F_y	F_z	M_x	M_y	M_z
AXC40A	40 x 55,8	75	210	B	5	6	500	500	2,4	20	20
AXC60A	60 x 72,7	150	560	B	5	8	2 800	2 800	19	100	100
				L	15	6	840	500	10	27	41
AXC80A	80 x 89,3	200	870	B	5	8	4 650	4 650	235	235	205
				L	15	8	3 400	2 300	60	110	170
AXC120A	120 x 133,5	320	2 500	B	5	8	9 500	9 500	120	925	925
				L	15	8	5 100	3 400	110	260	390
AXDL160A	196 x 103	210	1 960	D	5	8	9 000	9 000	475	475	475
				L	15	8	1 200	1 200	62	84	84
AXDL240A	280 x 145	272	5 000	D	5	8	12 500	12 500	1 050	1 200	1 200
				L	15	8	2 600	2 600	220	210	210

Figure E.1: Main parameters Linear Axis toothed belt- Ω - drive. Table 5.2 from [18].

E.2 Linear axis with toothed belt drive

Type	Axis cross section [mm]	Feed constant [mm/rev.]	Allowable dynamic operating load [N]	Guiding system	Maximum velocity [m/s]	Maximum total length [m]	Maximum dynamic load capacity [N]		Maximum dynamic load moments [Nm]		
							Fy	Fz	M_x	M_y	M_z
AXC40Z	40 x 53	75	210	L	15	6,0	310	170	2,4	3,9	7,0
AXC60Z	60 x 80	150	560	B	5	8,0	2 800	2 800	19	100	100
				L	15	6,0	840	500	10	27	41
AXC80Z	80 x 100	200	870	B	5	8,0	4 650	4 650	43	235	235
				C	5	8,0	4 650	4 650	43	280	280
				L	15	8,0	3 400	2 300	60	110	170
AXC100Z	100 x 125	264	2 200	B	5	6,0	5 000	5 000	52	275	275
				C	5	6,0	5 000	5 000	52	630	630
	104 x 125			D	5	6,0	7 000	7 000	200	325	325
	100 x 125			L	15	6,0	3 400	2 300	87	120	180
AXC120Z	120 x 150	320	2 500	B	5	8,0	9 650	9 650	120	875	875
				C	5	8,0	10 500	10 500	140	2 150	2 150
				L	15	8,0	5 100	3 400	110	260	390
				M	15	8,0	6 800	4 500	150	530	790
AXF100Z	104 x 125	264	1 800	B	5	6,0	5 000	5 000	52	275	275
				C	5	6,0	5 000	5 000	52	630	630
				D	5	6,0	7 000	7 000	200	325	325
				P	7	6,0	120	240	9	13	6,5
AXDL110Z	110 x 65	170	980	D	5	6,1	2 300	2 300	80	110	110
AXDL160Z	160 x 83	216	1 830	D	5	6,1	9 000	9 000	475	475	475
				L	15	6,1	1 200	1 200	62	84	84
AXDL240Z	240 x 120	264	5 000	D	5	6,35	12 500	12 500	1 050	1 200	1 200
				E	5	6,35	12 500	12 500	1 050	2 250	2 250
				L	15	6,35	2 600	2 600	220	210	210

Figure E.2: Main parameters Linear Axis toothed belt drive. Table 5.1 from [18].

E.3 Linear axis with screw drive

Type	Axis cross section [mm]	Ball screw drive		Trapezoidal screw drive		Sliding screw drive		Guiding system	Maximum dynamic load capacity [N]		Maximum dynamic load moments		
		Pitch [mm]	Maximum total length [m]	Pitch [mm]	Maximum total length [m]	Pitch [mm]	Maximum total length [m]		F_y	F_z	M_x	M_y	M_z
AXC40	40x53	5/10	2,5	3	3,0			B	675	675	3,2	22	22
AXC60	60x80	5/10/16	3,5	4/8	3,0			B	1 400	1 450	10	70	70
								C	3 550	3 550	24	220	220
								L	840	500	10	27	41
AXC80	80x100	5/20/50	5,5	4/8	6,0			A	4 500	4 500	42	270	270
								B	5 850	5 850	55	500	500
								F	--	--	--	--	--
AXC100	104x125	5/10/25/50	5,5	5/10	6,0			D	5 850	5 850	170	600	600
AXC120	120x150	5/10/20/32	5,5	6/12	6,0			B	12 000	12 000	160	1 150	1 150
								L	3 400	2 300	76	260	390
AXF100	104x125	5/10/25/50	5,5	5	6,0	20/60/90	3,0	D	5 850	5 850	170	600	600
								P	120	240	9	13	6,5
AXDL110	110x65	5/10/16	3,5	4/8	3,0			D	2 900	2 900	100	140	140
								E	7 100	7 100	250	470	470
AXDL160	160x83	5/10/25/50	5,5	5/10	3,5			D	11 500	11 500	575	800	800
AXDL240	240x120	5/10/20/32	5,5	6/12	6,0			D	16 000	16 000	1 350	1 500	1 500
								E	18 000	18 000	1 500	3 100	3 100

Figure E.3: Main parameters Linear Axis screw drive. Table 5.3 from [18].

E.4 AXDL110S

Type		SN1605	SN1610	SN1616	TN1604	TN1608
Guiding system		Linear guide D and E				
Table length T	mm	Linear guide D: 215 / Linear guide E: 275				
Distance of the sliding blocks L1	mm	≤ 200 mm (recommended 120 mm)				
Length of the floating bearing L2	mm	≥ 7,5 mm + 22mm with 3 x SA / + 54 mm with 4 x SA				
Drive element		Ball screw			Trapezoidal screw	
Screw diameter	mm	16				
Pitch / Pitch direction	mm	5 / right, left	10 / right	16 / right	4 / right, left	8 / right
Maximum velocity	m /min	30	60	96	5,5	10,9
Pitch accuracy	µm/300mm	52			50	100
Dynamic load rating of the ball screw	N	13 300	8 230	5 400	-	
Idling speed torque	Nm	0,8				
Maximum drive torque	Nm	1,1	2,2	3,6	1,9	2,9
Maximum axial operating load	N	1 400				
Moment of inertia	$Kgcm^2/m$	0,31		0,34	0,3	
Geometrical moment of inertia (profile) I_y	cm^4	37,45				
Geometrical moment of inertia (profile) I_z	cm^4	138,31				
Maximum total length	m	4,5			3,0	
Repeatability	mm	0,03			0,07	
Efficiency		0,91	0,97	0,98	0,35	0,52

Figure E.4: Technical data of the AXDL110S model. Table from [18] page 94.

E.5 AXDL160S

Type		SN2505	SN2510	SN2525	SN2550	TN2405	TN2410
Guiding system		Linear guide D					
Table length T	mm	280					
Distance of the sliding blocks L1 [1]		≤ 250 mm (recommended 140 mm)					
Length of the floating bearing L2	mm	≥10 mm +25 mm with 2 x SA /+75 mm mit 3 x SA /+125 mm with 4 x SA					
Drive element		Ball screw				Trapezoidal screw	
Screw diameter	mm	25				24	
Pitch / Pitch direction	mm	5 / right	10 / right	25 / right	50 / right	5 / right, left	10 / right
Maximum velocity	m /min	30	60	120	150	4,4	8,9
Pitch accuracy	µm/300mm	52				50	200
Dynamic load rating of the ball screw	N	19 800	16 100	12 100	15 400	-	
Idling speed torque	Nm	0,3…2,0					
Maximum drive torque	Nm	2,5	4,9	12,0	25,0	6,0	9,0
Maximum axial operating load	N	3 100					
Moment of inertia	$Kgcm^2/m$	2,62	2,82	2,62	2,25	1,5	
Geometrical moment of inertia (profile) I_y	cm^4	140,3					
Geometrical moment of inertia (profile) I_z	cm^4	666,8					
Maximum total length	m	5,8				3,5	
Repeatability	mm	0,03				0,07	
Efficiency		0,98				0,41	0,58

Figure E.5: Technical data of the AXDL160S model. Table from [18] page 96.

E.6 AXDL240S

Type		SN*/SV3205	SN*/SV3210	SN*/SV3220	SN*/SV3232	TN*/TV3606	TN*/TV3612
Guiding system		Linear guide D and E					
Table length T	mm	Linear guide D: 330 / Linear guide E: 500					
Distance of the sliding blocks L1 [1]		≤ 310 mm (recommended 180 mm)					
Length of the floating bearing L2	mm	Guiding system D: ≥12 mm + 50 mm with 3 x SA /+ 100 mm with 4 x SA Guiding system E: ≥ 12 mm + 35 mm with 4 SA					
Drive element		Ball screw				Trapezoidal screw	
Screw diameter	mm	32				36	
Pitch / Pitch direction	mm	5 / right	10 / right	20 / right	32 / right	6 / right, left	12 / right
Maximum velocity	m /min	23	47	94	150	3,5	6,9
Pitch accuracy	µm/300mm	52				50	200
Dynamic load rating of the ball screw	N	26 000	34 700	24 300	18 000	-	
Idling speed torque	Nm	1,5…2,0					
Maximum drive torque	Nm	6,4	13,0	26,0	41,0	22,0	30,0
Maximum axial operating load	N	8 100					
Moment of inertia	Kgcm²/m	6,05	6,40	6,39	6,17	9,00	
Geometrical moment of inertia (profile) I_y	cm⁴	761,7					
Geometrical moment of inertia (profile) I_z	cm⁴	3 956,0					
Maximum total length	m	5,5			5,0	6,0	
Repeatability	mm	0,03				0,07	
Efficiency		0,91	0,97	0,98		0,35	0,52

Figure E.6: Technical data of the AXDL240S model. Table from [18] page 98.

E.7 Angle connection

Y - Axis	Z - Axis	Designation	ID number	Lx [mm]	X [mm]	Ly [mm]	Lz [mm]	Z [mm]
AXDL110	AXDL110	AX-AC-ACU-Y110-Z110	363425	209	114	156	160,0	90
AXDL160	AXDL110	AX-AC-ACU-Y160-Z110P	269049	209	130	156	160,0	90
AXDL160	AXDL160	AX-AC-ACU-Y160-Z160	373108	287	144	236	220,0	120
AXDL240	AXDL160	AX-AC-ACU-Y240-Z160P	256449	287	177	236	220,0	120
AXDL240	AXDL240	AX-AC-ACU-Y240-Z240	382303	287	177	236	220,0	120

Figure E.7: Different possible configurations for the angle connection. The different notations refer to Figure 3.15c. Table 6.13 from [18].

UNIVERSITÉ CATHOLIQUE DE LOUVAIN
École polytechnique de Louvain
Rue Archimède, 1 bte L6.11.01, 1348 Louvain-la-Neuve, Belgique | **www.uclouvain.be/epl**